Università degli Studi di Ferrara

DOTTORATO DI RICERCA IN
FISICA

CICLO XXVIII

COORDINATORE Prof. GUIDI VINCENZO

DISPERSION AND TRANSPORT OF TROPOSPHERIC AEROSOL AND POLLUTANTS IN THE WESTERN MEDITERRANEAN: THE ROLE OF THE PO VALLEY UNDER DIFFERENT TRANSPORT REGIMES

Settore Scientifico Disciplinare FIS/06

Dottorando
Dott. Bucci Silvia

Tutore
Prof. Fierli Federico

Anni 2013/2015

Contents

Chapter 1

Introduction

1.1 Dynamics and atmospheric composition at the continental scale

Aerosol and chemical pollutants represent a significant environmental problem in many regions of the world. Concentration of such atmospheric components are determined by local and regional source emissions as well as long range transport from remote area. This reflects in a large temporal and spatial variability of pollutants distribution and in a wide variety of pollutant types. The magnitude ad impact of air pollutants is firstly determined by the location and intensity of emissions. Their position with respect to the dominant atmospheric transport patterns has a strong influence on the frequency and strength of intercontinental pollution advection. For instance at Mid-latitudes (where most of the major emissions regions of North America, Europe and East Asia are located), transport is dominated by the westerly winds that transport emissions from East Asia across the North Pacific Ocean to North America, from North America across the North Atlantic Ocean to Europe, and from Europe into the Arctic and central Asia [182]. Vertical transport play also a relevant role, as pollutants that are lofted into middle and upper troposphere can travel more effectively with respect to pollutants that remain in the lower troposphere. At the same time vertical mixing of pollution, linked to convective and turbolent atmospheric activity, can lead to the entrainement and mixing of long range tranport pollutants with surface air, affecting therefore local air quality. Once entered in the atmophere, pollutants can be subject to a wide variety of physical and chemical transformation so that polluted air masses can show very different properties from the source region to the downwind regions. Examples are represented by photochemical reactions, new particles formation, and loss processes as wet (removal by precipitation scavenging) and dry (gravitational) deposition. Taking as an example transport of pollution from Asia to North America, figure 1.1 syntetizes some of these processes undergone by Particulate Matter (PM) and Ozone (two of

the most important atmospheric pollutants).

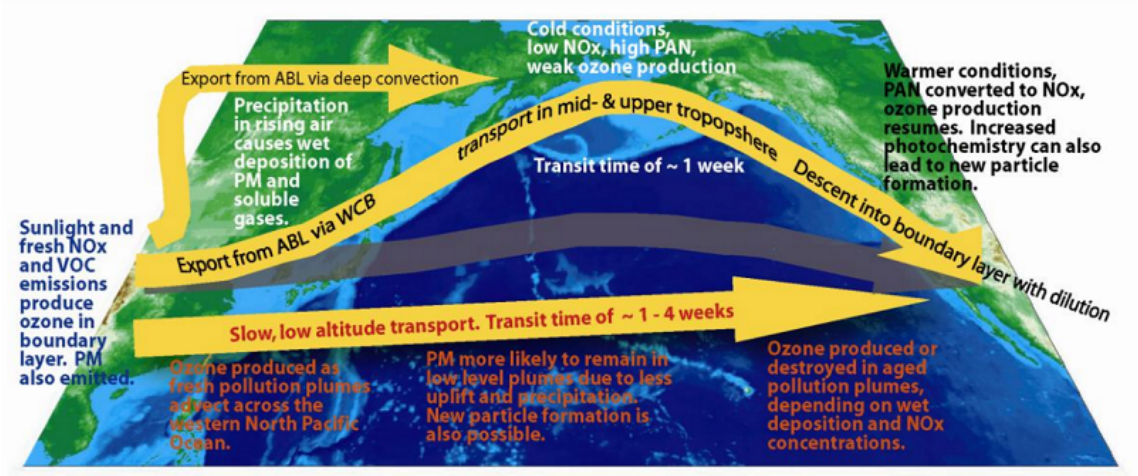

Figure 1.1: Transport and transformation processes during intercontinental transport of Ozone (O3) and particulate matter (PM). Blue text on the left applies to continental boundary layer processes, red text apples to low level transport and black/white text applies to high altitude transport[182] ABL stands for Atmospheric Boundary Layer (the lowest part of the atmosphere directly influenced by planetary surface, also called PBL), WCB stands for Warm conveyor belts (a transport layer created by cyclones in the mid-latitudes), PAN are peroxyacetyl nitrate, VOC are Volatile Organic Compounds and NOx are nitrates

1.2 Air Pollutants: Aerosol and trace gases

Any particulate or biological or chemical molecule in the Earth's atmosphere that may cause damages to living organisms and/or the environment can be considered an air pollutant. Air pollution may come from anthropogenic (e.g. vehicles, pesticides, waste disposal, industries) or natural sources (e.g. volcanoes, deserts, lightning, plants) and can be emitted directly in the atmosphere. In this case, they can be indicated as *primary emissions*. On the other hand pollutants can also results from the physical or chemical transformation of gases (that act therefore as *precursors*), like in gas-to-particle conversion (new particle formation by condensation of gaseous precursors, called *homogeneous nucleation*) or the interaction of gases with particles surface (e.g. coagulation and condensation over pre-existing particles, called *heterogeneous nucleation*). These complex processes yield a wide range of pollutant products both in the aerosol and gaseous form.

1.2.1 Aerosols

An aerosol can be defined as a two-phase system, being a collection of solid or liquid particles (with the exception of water, excluding therefore fog and clouds [145]) suspended in a gas. Aerosols diameters vary in the range of 10^{-9}–10^{-4} m, from

molecules and molecular clusters to sand particles [165]. Dust, fume, smoke, haze and smog are examples of aerosol.

Aerosols are mostly classified on the basis of their source characteristics, composition and size distribution, such as:

- **origins**: marine, continental, rural, desert aerosols, etc.
- **chemical composition**: sulfate (SO_4^{2-}), nitrate (NO_{3-}), carbonaceous aerosol (elemental carbon (EC) and organic carbon (OC)), sea salt(NaCl); etc.
- **particle size**: fine mode (d $<$ 2 µm) aerosol, ulteriorly divided in the Aitken (or transient) nuclei mode (about 0.005 µm $<$ d $<$ 0.1 µm) and accumulation mode (0.1µm $<$ d $<$ 2 µm), and coarse mode (d $>$ 2 µm) aerosol. The distinction between fine and coarse particles is clearly drawn: in general the fine and coarse particles modes originate separately (i.e. fine particles are mostly generated by gas-to-particles transformation, while coarse particles come mainly from mechanical processes). Moreover they undergo different physical and chemical transformations, different removal mechanisms and have different optical and chemical properties.

The composition of the atmosphere is highly complex, and a wide variety of chemical processes and physical modifications, in which aerosol constitutes an highly complex unit, can occur. The result is a continually changing chemical composition and particle size distribution. As said before, aerosol may represent a surface upon which (or with which) reactions can take place. Particles from different sources can mix with each other either externally (where each particle contains a chemically distinct aerosol species) or internally (where each particle contains a combination of different aerosol species) from Brownian diffusion and coagulation on microscale to atmospheric mixing processes on larger scales. Aerosols emitted from a specific source (e.g., soot, sea salt, or mineral dust), and consisting of a single specific substance, may become coated with the products of gas phase reactions. New particles are continually created and modified. Aerosol may be transported in the atmosphere or be removed by dry deposition, wet removal, and gravitational sedimentation. Typically, the lifetimes of aerosols in the troposphere range from a few minutes to several weeks. Consequently, the properties of the aerosol can exhibit a great deal of variability in both time and space [143]. Figure 1.2 illustrates some of the main processes involving particles of different origin and size.

1.2.2 Aerosol climatological and Health impacts

Because of their microphysical and optical properties, aerosol and gaseous pollution could play a critical role in many processes which impact indirectly on society, having

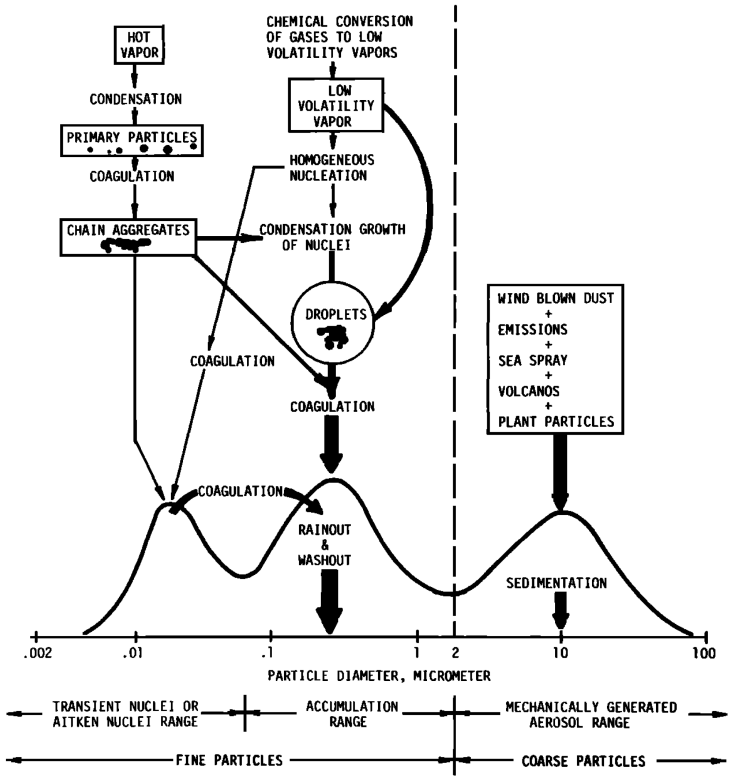

Figure 1.2: Schematic representation of the main sources of aerosol and the principal transformation and removal mechanism related to the resulting size distribution.[195]

strong effects on the regional radiative balance [11] with consequent effects on the climate [201], or directly, being potentially health damaging [80].

1.2.2.1 Climatological Effects

Aerosol particles affect the climate system via the following physical mechanisms:

- Aerosol can scatter and absorb solar and thermal radiation altering the radiative balance of the Earth-atmosphere system or, equivalently, the planetary albedo. Scattering or reflection of the longwave radiation emitted by the Earth surface (as it happens in presence of some desert aerosl) [45], as well as the backscattering of the incoming shortwave radiation (*global dimming*) [96] can cool the Earth's surface bringing to a negative radiative forcing that is estimate to be about 1 Wm^{-2} [179]. Absorbing particles instead (like the particles that constitute smoke) increase the absorption of the longwave radiation and incoming solar radiation with a increase in lower atmospheric heating of about 1 K day^{-1} [159]. This is the so-called *direct effect*. The global mean direct radiative forcing of aerosol, compared to other atmosphering components, is estimated by IPCC as reported in figure 1.3. Variation on the atmospheric absorption and scattering can affect the forcing of the atmospheric dynamics [179] at local level, as variation on the convective activity [96] or perturbating

the climate at the regional and global scale [159].

- Absorbing particles can also redistribute solar and thermal energy affecting evaporation processes and cloud formation. Because of aerosol absorbtion the evaporation of cloud droplets is increased [74] therefore leading to a decrease in cloud cover [135]. Moreover the temperature increase reduces the relative humidity possibly affecting the thermal atmospheric structure and dynamics [68]. This is called *semidirect effect* and, contrarily to the other aerosol effects, results in a net warming of the Earth-atmosphere system [94]

- Aerosol particles can act as cloud condensation nuclei (CCN) and ice nuclei (IN), offering surfaces on which water can condense. So the number of cloud droplets increases but the size of each droplet decreases. The optical depth of the cloud is thus enhanced [199] and reflectivity is higher, causing an increased albedo. This is called *cloud albedo effect or Twomey effect* [186]. On the other hand small droplets are less probable to grow by coalescence [152] leading to a decrease in the probability of precipitations and therefore to a longer clouds lifetime. This, in turn, reduces the net solar radiation at the surface [94]. Additionally less precipitations means drier soil, which in turn lead to an increase of dust in the atmosphere (*feedback loop*) [152]. These processes constitute the *indirect effect* that, again, lead to a resulting cooling at the surface, estimated to be around -0.7 W m-2 [76].

Such processes are schematically illustrated in figure 1.4.

The presence of a great variety of aerosol types, the large number of different sources, their distinct optical properties, their spatial distribution and atmospheric lifetimes constitute anyway obstacles for a deep understanding on the contribution of aerosols to the radiative forcing. In this framework aerosol measurements of size distribution, composition and optical properties can give important contribution in retrieving radiative relevant properties of the particles.

1.2.2.2 Health Effects

The link between exposure to fine particles in the atmosphere and adverse health effects has been well-established by epidemiological studies [80], [164]. Air pollution may have acute and chronic effects on human health. Although several natural processes may release pollutants in the atmosphere (volcanoes, fire, etc.) the anthropogenic activities are the main cause of environmental air pollution. In particular, in the last century, the increase in the combustion of fossil fuels played a key role [80]. The perilousness of an air pollutant depends on its chemical composition, reaction properties, persistence in the environment and possibility to undergo long or short transport. Aerosol air pollutants are generally indicated as *Particulate Matter*

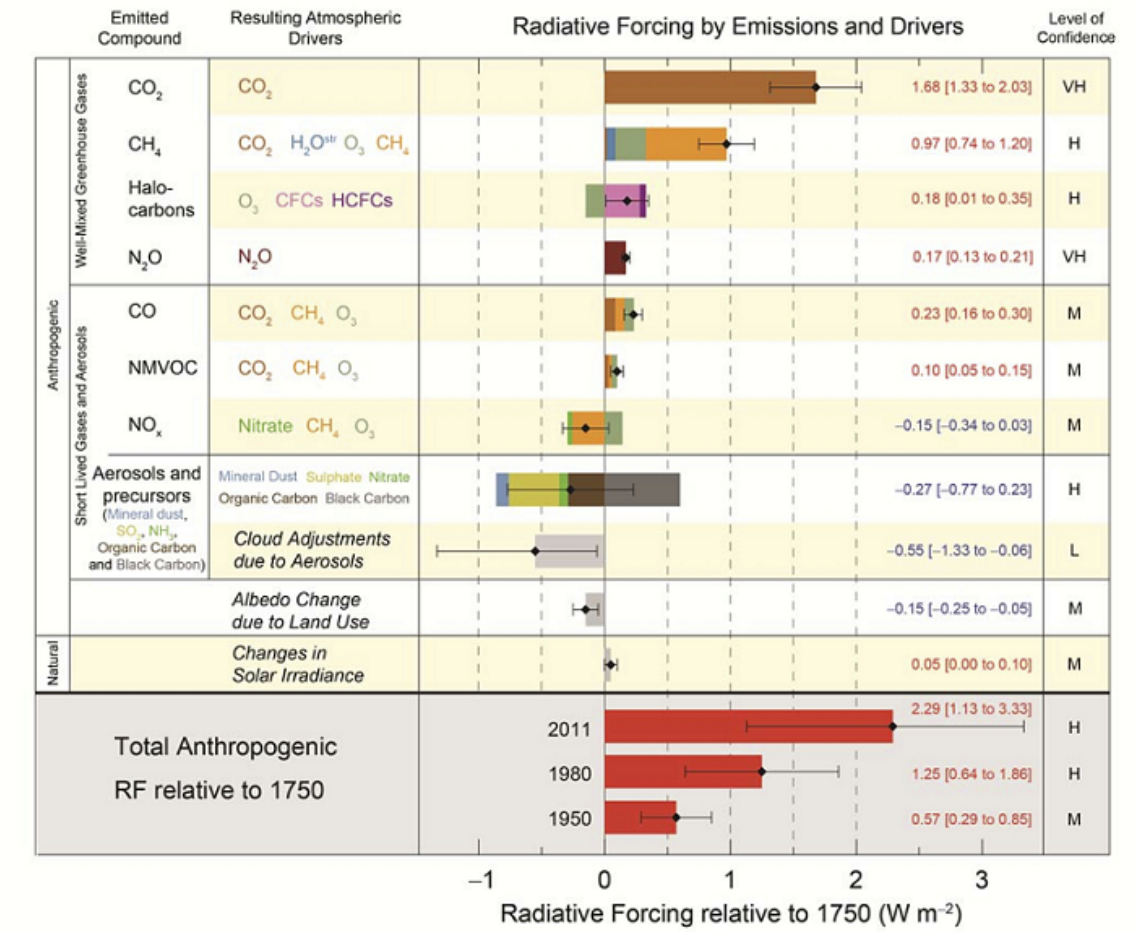

Figure 1.3: Schematic diagram of the global average aerosol radiative effects estimates in 2011 and relative to 1750, compared to the other atmospheric forcings [77]. Values are reported with their 90% confidence intervals year for greenhouse gases and atmospheric aerosols. Level of Confidence is reported as Very High (VH), High (H), Medium (M), Low (L). Total anthropogenic RF is also provided for three different years relative to 1750.

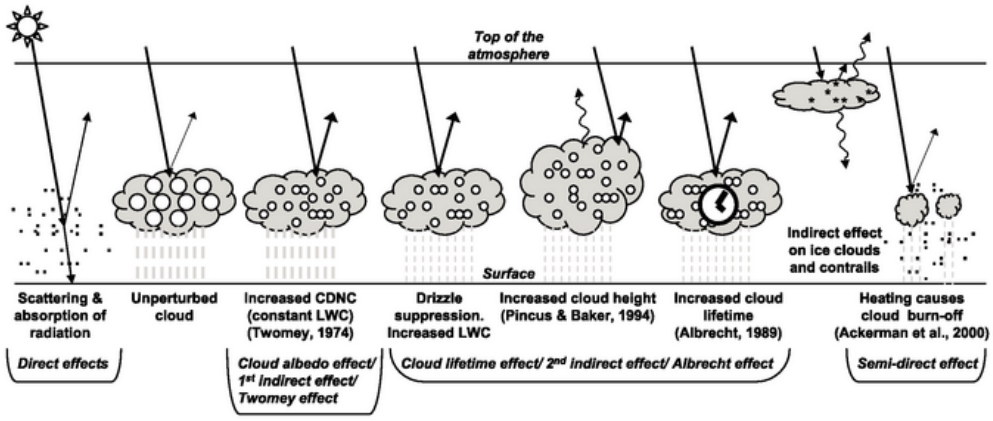

Figure 1.4: Schematic diagram of the aerosol radiative effects [76]. The small black dots represent aerosol particles; the larger open circles cloud droplets. Straight lines represent the incident and reflected solar radiation, and wavy lines represent terrestrial radiation. CDNC stays for cloud droplet number concentration and LWC refers to the liquid water content.

(PM). PM is the generic term that include complex mixtures of suspended particles, varying in size and composition, emitted by both natural and anthropogenic sources [141]. Two main categories of PM were defined: $PM_{2.5}$, particles with an aerodynamic diameter smaller than 2.5 μm, and PM_{10}, particles with an aerodynamic diameter smaller than 10 μm. This distinction is linked to the dependency on the particle size of the site in the respiratory tract in which particles will deposit. PM_{10} affect mainly the upper respiratory tract while fine $PM_{2.5}$ are able to reach lung and alveoli [80]. Inhalation in fact represent the primary route of exposure to air pollutants, although there is also an important contribution in food and water contamination, that makes ingestion another channel of contact [184]. In general, air pollution can affect different systems and organs: from acute respiratory irritation and chronic bronchitis to heart disease, lung cancer and asthmatic attacks [80]. Long term exposures have also been linked to premature mortality and reduced life expectancy [140]. According to estimates from the World Health Organization (WHO), particle pollution contributes to approximately 7 million premature deaths each year, making it one of the leading cause of worldwide mortality [198]. A study from the European Topic Centre on Air and Climate Change (ETC/ACC) estimated that PM2.5 pollution in European countries is associated with more than 492,000 annual premature deaths, corresponding to almost 4.9 million years of life lost (YOLL) every year. The geographic distribution of premature deaths attributable to exposure to PM2.5 is shown in figure 1.5.

Among the parameters that contribute to PM toxicity, size, surface and number of the particles are the most relevant [80]. The chemical composition is also playing an important role, with a major toxicological contribution from metals, organic compounds, material of biologic origins, ions and the particle carbon core [80]. Fine and ultrafine particles are demonstrated to be more dangerous than the coarse for mortality increases and cardiovascular and respiratory effects because they are sufficiently small to penetrate the membranes of the respiratory tract and enter the blood circulation or be transported along olfactory nerves into the brain [141].

A summary of the air pollution health impacts is presented in figure 1.6 [89] indicating premature mortality linked to chronic obstructive pulmonary disease (COPD) due to enhanced concentration of O3, cerebrovascular disease (CEV), ischaemic heart disease (IHD), COPD and lung cancer (LC) linked to PM 2.5.for adults older than 30 years and acute lower respiratory illness (ALRI) for infants with less than 5 years. Data are reported relatively to 2010 with future projections on year 2050 assuming that only currently agreed legislation is implemented. Globally the contribution of air pollution is estimated to lead to more than 3 million premature deaths, while results for Europe shows an estimate of 381 thousand premature death in 2010. Future scenarios suggests that those numbers could double in 2050.

An efficient control of air quality, based on a comprehensive understanding of

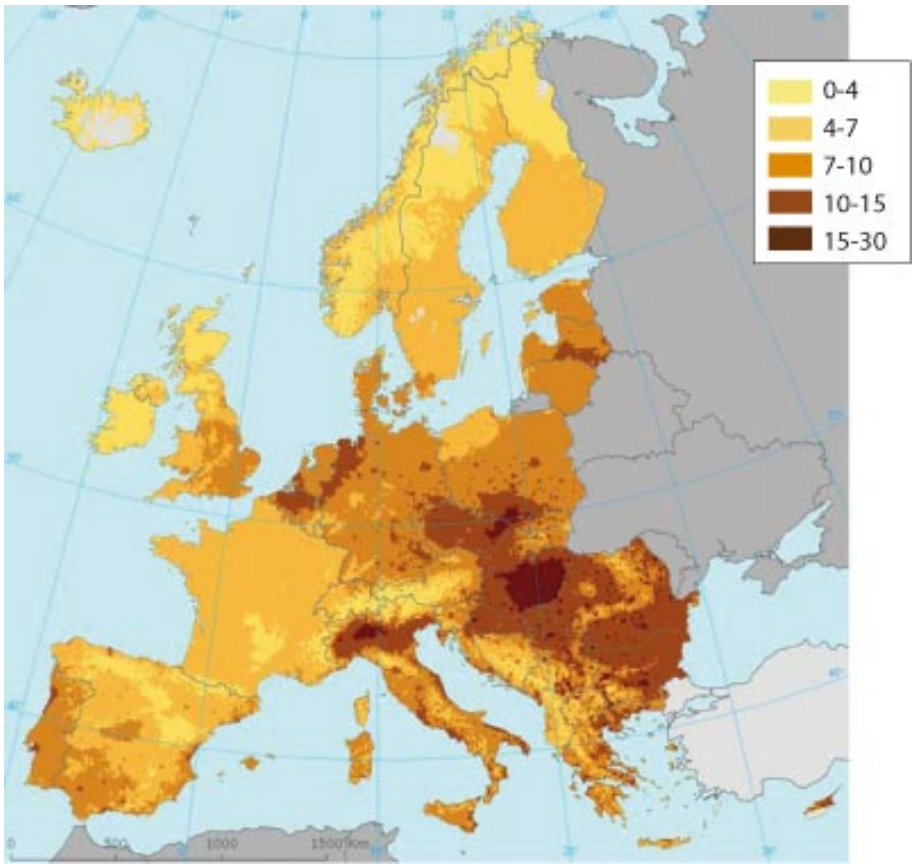

Figure 1.5: Premature mortality (expressed as deaths per 10,000 inhabitants/year) attributable to PM2.5 exposure at year 2005 pollution levels, source: http://www.airclim.org/

Premature mortality related to $PM_{2.5}$ and O_3 for the population <5 and ≥30 years old

WHO region	Year	Population ($\times 10^6$)	Mortality attributable to air pollution (deaths $\times 10^3$)						
			$PM_{2.5}$					O_3	Total
			ALRI < 5 yr	IHD ≥ 30 yr	CEV ≥ 30 yr	COPD ≥ 30 yr	LC ≥ 30 yr	COPD ≥ 30 yr	
Africa	2010	809	90	55	77	11	2	2	237
	2050	1,807	158	185	262	38	5	12	660
Americas	2010	930	0	44	8	4	7	5	68
	2050	1,191	0	75	15	7	11	11	119
Eastern Mediterranean	2010	602	56	115	86	12	5	12	286
	2050	1,021	66	321	246	37	13	40	723
Europe	2010	867	1	239	95	13	27	6	381
	2050	886	1	307	156	18	37	11	530
Southeast Asia	2010	1,762	64	327	250	124	15	82	862
	2050	2,332	104	865	807	419	48	227	2,470
Western Pacific	2010	1,812	19	299	794	209	107	35	1,463
	2050	1,861	16	413	1,120	309	155	57	2,070
World	2010	6,783	230	1,079	1,311	374	161	142	3,297
	2050	9,098	346	2,166	2,604	828	270	358	6,572

Figure 1.6: Premature mortality linked to CEV, COPD, IHD and LC for adults older than 30 years old, and ALRI for infants < 5 years old. [89]

the nature, sources, atmospheric interactions and sinks of air pollutants, is therefore required to limitate potentially dangerous health effects. Without this understanding, the introduction of new laws and regulations for environmental protection runs the risk of being ineffective or even counter-productive [141].

1.2.3 Trace Gases

Trace gases can be defined as gases that constitute an extremely small portion of a mixture. Most of our atmosphere is made up of nitrogen (78% by volume) and oxygen (21% by volume). So trace gases constitute the remaining 1%. Despite their very small concentrations, trace gases have several important effects on both the Earth's weather and climate. About 90% of the total atmospheric mass resides in the troposphere (the region of atmosphere extending from surface to tropopause at around 10-18km) so also the largest part of trace gases burden can be found there. These gases can be emitted directly into the tropopshere from surface by combustion of fossil fuels such as fuel oil, gasoline, and natural gas like in power plants, automobiles, and similar combustion sources like waste incineration. In troposphere they are subject to a series of complex chemical and physical transformations, reacting or interacting with each other, with sunlight, and with water vapor, cloud droplets, and raindrops. In particular photochemistry and the produced troposheric radicals play an important role influencing the atmospheric composition and its climatic and air quality impact. The air pollutants trace gases of most relevance in urban settings are ozone (O_3), carbon monoxide (CO) and nitrogen oxide (NO_x).

- Ozone (O_3) is a key component of smog and it is a secondary pollutant. Tropospheric ozone in fact is not emitted but chemically produced in the atmosphere via the photochemical oxidation of volatile organic compounds (VOCs) like benzene, formaldehyde and chlorofluorocarbons, and carbon monoxide (CO) in the presence of nitrogen oxides (NOx). In such case the production of Ozone is subject to the following reactions[110]:

$$\mathrm{OH + CO \longrightarrow H + CO_2} \tag{1.1}$$
$$\mathrm{H + O_2 + M \longrightarrow HO_2 + M} \tag{1.2}$$
$$\mathrm{HO_2 + NO \longrightarrow OH + NO_2} \tag{1.3}$$
$$\mathrm{NO_2 + h\nu \longrightarrow O + NO} \tag{1.4}$$
$$\mathrm{O + O_2 + M \longrightarrow O_3 + M} \tag{1.5}$$
$$\tag{1.6}$$

Where OH indicates the hydroxyl radical (a strong atmospheric oxydant), $h\nu$

is the energy of solar radiation, HO2 is a peroxy radical and M represents a third body that partecipate in the reaction. The resulting net reaction is the production of O3:

$$CO + 2\,O_2 + h\nu \longrightarrow CO_2 + O_3 \tag{1.7}$$

On the contrary, when NOx are present in little concentration O_3 destruction is the dominant factor:

$$OH + CO \longrightarrow H + CO_2 \tag{1.8}$$
$$H + O_2 + M \longrightarrow HO_2 + M \tag{1.9}$$
$$HO_2 + O_3 \longrightarrow OH + 2\,O_2 \tag{1.10}$$
$$\tag{1.11}$$

with resulting

$$CO + O_3 \longrightarrow CO_2 + O_2 \tag{1.12}$$

Therefore production or loss of Ozone are dependent on HOx and NOx concentration [110].

While in the stratosphere ozone plays an important and beneficial role by providing a shield from the hazardous shortwave radiation, in the troposphere, ozone is harmful to plants, causing damages to crops, forests and grasslands, and to humans. At high concentrations in fact it inflames lung tissues and can cause chest pains, asthmarespiratory problems and can finally lead to increased death rates during smog events. Moreover O3 contributes to climate forcing both directly, acting as a greenhouse gas, and indirectly, damaging vegetation. Its radiative forcing can affect area from regional to intercontinental scale from the precursors emissive regions [182]

- Carbon monoxide (CO) is mainly produced by incomplete combustion (i.e. not enought oxygen is present for complete oxidation) of carbon-containing fuels, such as gasoline, natural gas, oil, coal, and wood. CO air concentrations are generally high in areas with heavy traffic congestion as emissions from vehicles contribute for about the half of all CO emissions [163]. Its primary sink is oxidation by the hydroxyl radical (OH), which in turn controls the removal of most of the atmospheric pollutants as it is usually the predominant

atmospheric oxidant [34] The yearly average concentration of CO in different areas of the world is reported in figure 1.7 with indicated also the contribution from different processes.

	Total	Origin of CO							
		Industrial activities		Biomass burning		CH_4 oxidation		NMHC oxid. and other	
	ppbv	ppbv	%	ppbv	%	ppbv	%	ppbv	%
Total	93	27	29	20	21	23	25	23	25
Europe	163	85	52	28	17	22	15	28	16
North America	128	53	42	26	20	23	18	26	20
Asia	133	52	39	30	23	23	17	28	21
Africa	120	22	18	41	34	26	22	31	26
South America	105	9	9	35	33	24	23	37	35
Oceania	65	6	9	14	22	23	35	22	34
North Atlantic	104	33	32	21	20	26	25	23	23
South Atlantic	53	4	8	10	19	22	41	17	32
North Pacific	89	25	28	17	19	25	28	22	25
South Pacific	50	4	8	7	14	22	44	17	34
Indian Ocean	53	4	8	9	17	22	41	18	34

Figure 1.7: Yearly average surface CO concentration in regions of the world, in ppbv, and contribution from the different processes leading to CO formation[63]: Industrial activities, Biomass Burning, CH4 (methane) oxidation and NMHC (non-methane hydrocarbons) oxidation

In Europe mean CO concentration was estimated to be more than 150 ppbv with largest contribution coming from industrial activities (more than 50%). Globally, industrial activities, biomass burning and oxidation of methane (CH4) and other hydrocarbons seems to contribute in similar amounts. The total global surface average is indicated to be 93 ppbv. Carbon Monoxide, apart from being considered a precursor of ozone is also a dangerous pollutant. When breathed in high concentration, it reduces the amount of oxygen carried by haemoglobin around the body in red blood cells. The result is that vital organs, such as the brain, nervous tissues and the heart, do not receive enough oxygen to work properly. CO exposure is also closely associated to cardiovascular disease [70] and cardiac mortality [157].

- Nitrogen oxides (NOx, mainly NO and NO2) are relevant species in determining air quality. At high concentrations $NO2$ is a toxic gas and can have hazardous effects on lung functioning and on the respiratory system, also at relatively low NO2 concentrations when in combination with long-term exposure (WHO, 2000). Indirect negative effects arise from the tendence of NOx to favor to the formation of ozone and fine particles. Major formations of NOx came from anthropogenic sources like fossil fuel combustion and biomass burning but they can form also from natural sources like soil emissions and lightning. NOx is mainly removed from the atmosphere with the formation of nitric acid (HNO3) that is subsequently deposited on land and ocean surfaces as acid rains or dry deposited. Human health concerns include effects on

breathing and the respiratory system, damage to lung tissue, and premature death.

For our study we will mainly focus on the CO species as it is an excellent tracer for pollution sources and pollution pathways through the troposphere. Because of the relatively long lifetime (from few weeks to few months) of most CO, it is not thoroughly mixed throughout the troposphere. This implies that the distribution of the CO situated in the lower troposphere is close to its source distribution. Conversely, in the free troposphere CO has a relatively long lifetime, which permits the study of long range transport in the upper troposphere and makes it a useful tracer of other pollutants [119].

1.3 Atmospheric measurements techniques

As pointed out in the previous sections, the knowledge on size-distribution and optical and chemical properties of pollutants, as well as spatial distribution and temporal evolution, is required to have a complete understanding on the possible climatological and health impacts. To achieve this goal many different air measurements techniques were developed:

in-situ measurements In situ measurements are observations performed with the instrumentation located directly at the point of interest and in contact with the subject of interest. In-situ measurements techniques offer the advantage of rapid and cotinuos particles detection and can retrieve detailed information on the sample like: total number concentration or optical coefficients (e.g. Condensation Nuclei Counter, integrating nephelometr) aerosol physical chemical properties (e.g., filters, mass spectometers), measurements of aerosol size distributions (e.g., Optical Particle Counter, electrical mobility analyzer, Aerodynamic Particle Sizer), and measurements of size-resolved aerosol composition (e.g. Cascade impactor, Electron microscopy). Such information is essential to quantify the possible impacts of the various species on processes like radiative forcing, health effects and atmospheric microphysics and chemistry. In-situ measurements has nevertheless the disadvantage of being point monitors, giving only locally representative information and no vertical distribution of properties. Even if instruments can be located on board of aircraft, balloons or mobile laboratory, the spatial sampling remains limited in time. Moreover, the mobility of the platform may affect the sampling accuracy of the instrument.

Remote sensing instruments Remote sensing instruments can operate with passive or active sensors. Passive sensors detect natural energy that is emitted by Sun or reflected by the aerosols, molecules and clouds (like sun photometer or

infrared spectrometry or microwave radiometer). Passive remote sensing instrumentation can probe large volumes of atmosphere but often provide poor vertical resolution or integrated columnar atmospheric values. Additionally measurements are strongly dependent on natural light sources and in some cases they can be reliable only during daytime. Cloud cover can also affect atmospheric observations resulting in bias and high uncertainties.

Active sensors, on the other hand, emit radiation which is directed toward the target to be investigated. The radiation reflected or backscattered by the atmospheric component is detected and measured by the sensor (e.g. Light Detection and Ranging (LIDAR) sensor or synthetic aperture radar (SAR)). These sensors can collect measurements regardless of the time of day or season. Moreover, active remote sensing can give vertical resolved measurements as, computing the time required for the signal to travel to the target and return back to the sensor, is possible to determine the distance or range from the target. However, active systems require the generation of a fairly large amount of energy and often it puts limitations on the vertical extent of the atmospheric portion that can be observed.

Chemical Transfer Models (CTMs) The combination of satellite, airborne and ground based in-situ and remote sensing observations allows, to some degree, to overcome many of the described limitations and help have a comprehensive overview on the spatial extension and main relevant properties of the atmospheric components. Nevertheless observational evidence can also be combined with atmospheric chemistry and transport models to have better insights into processes of emission, transport, transformation, and removal that affect the observed concentrations. Such models are called chemical transport models (CTMs). Using meteorological information as input they solve the continuity equations for mass conservation of the chemicals in the atmosphere. A CTM can be Eulerian or Lagrangian. A Eulerian model simulates transport reproducing three-dimensional grids through which fluxes, chemical production/loss and deposition occur over time. Such models are largely adopted to reconstruct of global (e.g. GEOS-Chem) and regional (e.g CHIMERE, WRF-CHEM) budgets of atmospheric chemicals. Lagrangian models instead follow the motion and the possible physical evolution of parcels of air over time basing on trajectories simulation. Such models can provide source-receptor relationships and offer understanding on the relation between concentrations at a given location and emissions found upwind. Largely adopted examples of Lagrangian CTM are HYSPLIT and FLEXPART.

1.4 The Mediterranean Basin: climatological, transport and air composition characteristics

The Mediterranean region plays an essential role in climate feedbacks [170, 6, 71] [60] as well as being a sensitive hot spot for air quality issues [111]. Several studies indicate that in the Mediterranean region the aerosol radiative forcing, during summer, is among the highest in the world [88],[59]. The Mediterranean climate is affected by local processes induced by the complex morphology of the region (for example the presence of the Alpine chain acts as a forcing, modifying travelling synoptic and mesoscale systems) and the presence of a large body of water (the Mediterranean Sea) that constitute an important source and reservoir of energy, moisture and precipitation in the region [58, 162, 91]. Atmospheric circulation over the WMB is also highly influenced by the Azores high pressure system and is balanced between two synoptic systems [106, 131, 168]. During the last decades, the rapid growth in urbanization led to the birth of several Megacites [1] in the Mediterranean region, with consequent growth in vehicle use and industrialization and therefore increase in the pollutant emissions to the atmosphere. Observations show that the spatial distribution of atmospheric pollution concentration and composition over the area is often complex and high variable in space and time, due to the interplay of sources and transport regimes leading to different pollutants and aerosol typologies of both natural (Desertic particles, sea salt, vulcanic ashes) and anthropogenic (black carbon, sulphate, etc.) origins with large differences in spatial patterns and properties [88] in relation to different origin processes and export conditions [52, 171, 95]. Rea et al. 2015 [149] for example demonstrated that, during summer 2012, the PM10 and the PM2.5 over the WM were constituted respectively for the 86% and 44% by dust. PM10 exceedance were mainly caused by dust (more than the 49.5% of cases) while for PM2.5 they where mostly carried by antropogenic (more than 46.3%) and biogenic(more than 12.6%) particles. Fires influenced the PM10 and PM2.5 exceedance only less than the 7.2% and 12.4% of the cases. Querol et al. 2009 [147], among the others complexities, highlights an increase in the PM10 and PM2.5 load moving from the west to the east side of the Mediterranean and from North to South, as well as notice a clear seasonal pattern (with summer maximum due to lower precipitation, higher resuspension, photochemical transformations and frequent African episodes) in PM levels in the western part of the Mediterranean. In this region a key role in determining the intensity of aerosol and gaseous related pollution events is in fact also played by meteorological conditions [108]. During winter, pollution over the Mediterranenan is limited by wet removal from freqeunt precipitations, while clouds and low insolation limit the phochemistry and thus the production of harmful chemical. On the contrary Mediterranean summer is characterized by

[1] urban agglomeration with more than 10 million of inhabitants, http://www.worldclimate.com

high pressure situations with consequent conditions of subsidence, stability, clear sky (with consequent limited washout) and high solar radiation intensity that favor photochemical processes [189] and emissions of biogenic VOC's [108]. When in presence of favourable meteorological conditions and high solar radiation air masses in the Mediterranean Basin are mixed and aged causing alterations on the aerosol properties. Dust coated by pollution components can show modified climate relevant properties [81], or change hygroscopic behaviour via nitration and suplhation [147]. In Mediterranean climates, photochemistry is a significant process in the formation of secondary particles as aerosols released to the atmosphere can co-react under the presence of sunlight, producing secondary pollutants [16]. High insolation periods (in correspondence for example of low cloud formations) is also linked to atmospheric abundance of highly hygroscopic aerosols [147]. During summer the complex layout of the coast and surrounding mountains lead also to the development of sea breeze, upslope winds and recirculation flows. These cause pollutant accumulation and subsidence over the coast and the sea and return flows of pollutants accumulated during night that recirculate during daily breezes. [56, 3]. Synoptic circulation and local dynamics impact on vertical distribution, layering and aging of particles along the coast [106, 56, 131, 188].

1.4.1 Long Range transport

As air masses can remain over a specific region for a prolonged period, local sources are strongly affecting the surface concentration of pollutants. Nevertheless long and regional range transport of both natural and anthropogenic pollution over the Mediterranean is demonstrated to be of similar impact on the background air pollution levels as the local sources [81]. The Mediterranean area in fact represents a crossroad of air masses patterns coming from Europe, Asia and Africa. Transport from anthropogenic air pollutants come mainly from southern and Eastern Europe and the central Mediterranean Region toward the eastern Mediterranean Region, northern Africa, and the Middle East, while the major contribute of natural pollutants comes from the Saharan dust [7]. A conceptual diagram of the transport paths for air pollutants in the Mediterranean Region, resulting from analysis of air pollution episodes and modeling systems [7] is illustrated in figure 1.8

1.4.1.1 Dust transport

The relative proximity to the Sahara desert, the major dust source of the planet [144, 193], makes this region often subject to long range dust transport, with an higher frequency during the summer season [79, 100, 130, 24], up to 8 single episodes during a single season for the Western part of Mediterranean [61], due to favorable synoptic conditions for dust advection across the Mediterranean basin, towards

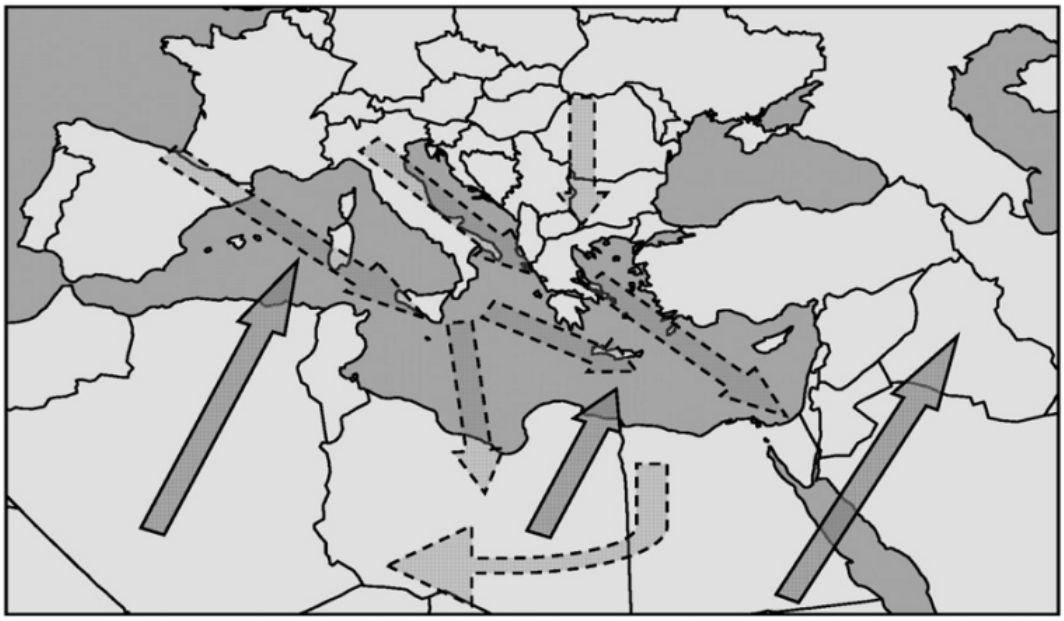

Figure 1.8: Schematic representation of the characteristic paths and scales for transport of air masses in the Mediterranean Region. Grey dashed arrows indicate the transport of anthropogenic pollutants in the lower troposphere while solid arrows highlight the main Saharan dust transport path in the Mediterranean Region [7]

southern Europe. Dust storms over African deserts may be caused by the formation of low-pressure systems over the Atlantic or north Africa with high pressures over the Mediterranean, or by a pattern of high pressures at upper levels over North-West Africa [47, 147]. At the same time, the uplift of dust particles at higher atmospheric levels is possible, caused by the strong surface winds and the large-scale convection that typically involves north Sahara during summer months [147]. Dust is then transported over the basin following usually anticyclonic pattern of circulation over Mediterranean basin [61] triggered by the extended subtropical anticyclone of the Atlantic Azores in correspondence to the extended thermal low of south-west Asia. Dust is found to be usually transported in the high troposphere: Papayannis et al., 2005, during a continuos period of measurements between 2000 and 2002, sistematically observed multiple dust layers of variable thickness (200-3000 m) over the Eastern Mediterranean, with the greatest load detected between 2 and 5 km. Nevertheless there is evidence of episodes of mixing with local pollution near the ground [14, 62, 136, 130] that can modify the local aerosol optical properties [128] and increase the local PM concentration, with an estimated annual mean contribution of 10ug/m3 in North-Italy, possibly causing episodes of exceedances of the legislative PM10 daily limits [102, 130, 23]. Such studies relied on in situ measurements, while a direct evidence of dust entrainment in the PBL from continuous observations of the vertical aerosol distributions was missing.

1.4.2 Anthropogenic pollution transport

Although the anthropogenic pollution typically remains close to the emission sources, local meteorology can transport some of this contaminated air mass to rural and remote areas. In general Liu et al 2013 [93] showed that air pollution can br transported at long distances and the nocive effects of emitted pollutants may not be confined to the emissive region. The necessity of an estimate of the imported pollution grows as the emissions in developing countries increase while European air quality standards are restricted. North Western Mediterranean has been demonstrated to be affected by continental outflow and severe pollution episodes, especially during summer beacause of the build up of ozone and other pollutants linked to the typical summer stagnant conditions (high humidity, low winds..etc) [107]. As said before the topography of the Mediterranean coast and the typical meteorological conditions lead to land and sea breezes. These processes can carry the pollution accumulated in the industrialised valleys and depressions to remote and rural areas, and even at higher altitudes, resulting in intense pollution episodes [134, 137]. Lelieveld et al. 2002 [88], showed high values of CO over the Mediterranean region, even though a negligible influence of local pollution sources. Their results indicate that regions surrounding the Mediterranean such as southern Italy, Greece, Yugoslavia, the Middle East, and North Africa contribute to the CO with a typical contribution of about 20%. While the eastern Mediterranean is mainly polluted by emissions from eastern Europe, the strongest influences over the western Mediterranean come from France, Germany, and northern Italy [88]. A recent study from Di Biagio et al. (2015) [41], basing on aircraft measurements, shows that continental pollution largely affects the western Mediterranean both close to coastal regions and in the open sea up to $\sim$ 250 km from the coastline. Basing on aircraft measurements they observed aerosol scattering coefficient between 20 and 120 Mm^{-1} and carbon monoxide (CO) and ozone (O3) mixing ratios in the range of 60–165 and 30–85 ppbv, respectively. Our study will mainly focus on the North Italy pollutant source region, and in particular on the Po Valley basin.

1.4.2.1 The Po Valley as an emissive region

The Po basin in Northern Italy is one of the most important emissive region, characterized by high concentration of both natural and anthropogenic aerosol and trace gases [111]. The region is an air pollution hot spot, where the European air quality standards are often exceeded for PM10, NO2 and O3 [51]. With its population densities among the highest in Europe (of about 20 million people), the Po Valley can be also considered as a "distributed megacity"[51]. The geographical location of this region, surrounded by two mountain ranges (the Alpine chain at the North and West side of the valley and the appennines to the South), favours frequent occurrence of

stagnant meteorological conditions [153], with an accumulation of local pollution [67, 39, 156, 40] from industrial, urban and agricultural emissions, and complex processes of aerosol-chemicals transformation. High emissions, coupled to stagnant atmospheric conditions, lead to unusually high concentrations of atmospheric pollutants and particulate with frequent and prolonged periods of intense pollution. This is visible also from satellite as in figure 1.9 where it is possible to identify a grey veil of haze over the Po Valley and expanding over the Adriatic Sea. Consequently the region is one of the areas with the highest AOD[2] in the world: Multi-year TOMS and MODIS observations over the eastern Mediterranean [69], as well as on the Po Valley [154] indicate the occurrence of high AOD values (up to more than 0.8 at 500 nm) over large urban areas surrounding megacities. Figure 1.10 shows the AOD (at 550 nm) as seen from MODIS and MISR satellites for the 2003 to 2012 period with annual mean values ranging from 0.2 to 0.5 [117] Similarly the region is also strongly affected by high concentration of gaseous pollutants: Lelieveld et al. (2002) [88], using model analysis of Chemistry and Transport Model (CTM) applied to anthropogenic sources in different part of Europe, showed peaks over Mediterranean of 150 ppbv of CO, compared to North and South Pacific values of 60-70 ppbv and 40-50 ppbv. He also found summer O3 concentrations over the Mediterranean to be a factor of 2.5–3 higher than in the hemispheric background troposphere (with mean surface mixing ratio of about 60 to 65 ppbv). This is also easily seen from figure 1.11 (from the Harvard University GEOS-CHEM model [72]) that illustrates model calculations of monthly mean afternoon surface ozone concentrations in July.

Figure 1.9: True-color Terra MODIS image from March 17, 2005, source: http://visibleearth.nasa.gov/

1.4.3 Thesis Objectives and Outlines

In general large uncertainties still persist in the estimation of the possible impacts of air pollution mainly due to the difficulties that limitate a full characterization of the physical and chemical properties of pollutants and their spatial and vertical distribution [15]. In order to understand aerosol role and predict their behaviour it is necessary to consider their various properties, like size distribution and their composition [143]. For gases, differently, is generally sufficient to measure the concentration

[2]The aerosol optical depth (AOD) represents the integration of the extinction by particles along the whole atmospheric column

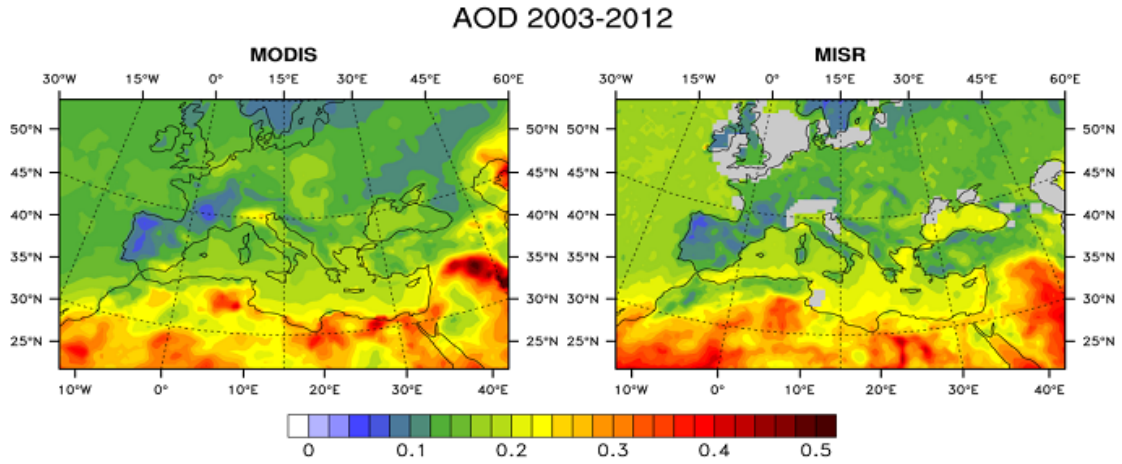

Figure 1.10: Annual mean values of AOD (at 550 nm) over the Mediterranean retrieved from MODIS and MISR satellites for the 2003 to 2012 period [117]

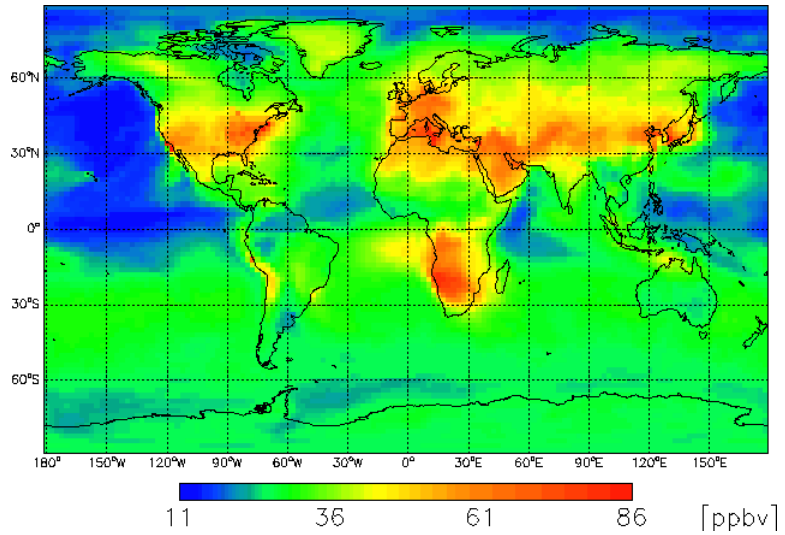

Figure 1.11: Monthly mean afternoon (1 to 4 PM) surface ozone concentrations calculated for July using Harvard GEOS-CHEM model[72]

in order to assess any possible radiative and health effects. The present thesis has the objectives of providing such kind of information in the complex framework of the Mediterranean synoptic circulation and emissions. In particular this work aims to give an inside on the aerosol and gaseous pollutants vertical distribution evolution over the North Western Mediterranean basin, under the different local and regional meteorological conditions that occured during the 15th June 2012 - 5th July 2012 period. In this time interval a wide variety of synergistic measurements take place as part of different campaigns and projects. The analysis of an extensive aerosol and gas observational dataset and of the atmospheric transport regimes allowed to evaluate the aerosol and gaseous pollutants variability from the planetary boundary layer (PBL) to the free troposphere. The adoption of Lagrangian and Chemical Transport Model (CTM) simulations supported the pollutants transport analysis over the Northern Mediterranean basin. The analysis deal with processes at different spatial and time scales, from large-scale transport of dust to the variability of aerosol in the PBL in stagnant condition.

Chapter 2 presents the framework of the analysis, describing the campaign, the projects and the sites from which the observations were collected. The chapter analyses the details of LIDAR data treatement and the methods of aerosol classification, showing the optical profiles collected during the whole campaign. Other instruments used for the study, including the FLEXPART and the WRF/WRF-CHEM models, are then presented. **Chapter 3** describes the meteorological evolution during the campaign, analyzing the different transport regimes and the possible convective activity. The impact of such meteorological variability on the vertical distribution of aerosol is then explained by means of the coupling between LIDAR, in-situ aerosol measures and backtrajectories analysis. Events of long range transport of particulate, as well as local aerosol processes, are presented. A diurnal vertical resolved statistical analysis on the aerosol evolution during the campaign is offered at the end of the chapter. **Chapter 4** describe the dynamics and the intensity of air pollution export from the Po Valley to the Gulf of Genoa, basing on the CO specie as a tracer of pollution. The reliability of the Po Valley meteorological and chemical information derived from the WRF-CHEM model are evaluated by comparison with local in-situ measurements. The model is then adopted in conjuction with FLEXPART forward trajectories and aircraft data analysis for the identification of the outflow plumes during the summer 2012 campaign. The transport simulation analysis is then extended for the whole 2012 year to look for possible seasonality in the export events. **Chapter 5** drives the main conclusion and perspectives of the study.

Chapter 2

Observations and methods

To evaluate the aerosol variability from the PBL to the free troposphere over the North Mediterranean region, a sinergy of remote sensing, in-situ, airborne measurements and model analysis is adopted. The period under consideration is summer 2012 (in particular 15th June - 5th July), when a large dataset of aerosol, gas and meteorological observations were collected as part of different european and italian projects (ChArMEx, PEGASOS and Supersito, presented in section 2.1). The region investigated (Po Valley and Gulf of Genoa) is shown in figure 2.1 with large fraction of the observation collected at the San Pietro Capofiume (SPC, 44°39'0" N, 11°37'0" E,11m a.s.l) and Mount Cimone (MTC, 44.12N, 10.42E, 2165 m asl) stations (described in the next paragraphs)

Instrumentation Meteorological reference was derived from the vertical profiles, from ground up to 4km, of wind speed and direction from radiosondes (Vaisala RS92) launched each day at 00:00, 06:00 and 12:00 UTC from the meteorological station at the SPC station. Large part of the aerosol analysis is based on the **LIDAR** profiles, used to investigate the vertical distribution of aerosol and their optical properties. Remote sensing is complemented with in-situ data: an **Aerodynamical Particle Sizer** (APS) at SPC provides information on the concentration and dry diameter of aerosol reaching the ground (at around 30 m a.s.l.), while in-situ size distribution from an **Optical Particle Sizer** (OPC) at the Monte Cimone WMO/GAW Global Station provides a reference for transition layer between the summer PBL and the lower part of the free troposphere. Aerosol chemical composition from the **Monitor for AeRosols and Gases in ambient Air** (MARGA), analysez at SPC, are used as ancillary data to evaluate the typology of particulate in well-developed PBL conditions. LIDAR retrievals of aerosol exinction were also used for comparison with simultaneous observations from the PEGASOS Zeppelin during a measurement day at SPC and with the SPC ground based Sky Radiometer (SkyRad). Trace gas measurements were taken on a larger domain over North Italy: data were provided by a **non-Dispersive Infrared analyser** (NDIR)

at the MTC site, several urban site across the Emilia Romagna region from the **BRACE** network (http://www.brace.sinanet.apat.it/), the **MOSQUITA mobile lab** travelling through Po Valley and two **TRAQA flights** passing over the Gulf of Genoa. A better diagnostic on the air masses transport, origins and variability is provided by model analysis from the Lagrangian transport system **FLEXPART**, driven both by the meteorological mesoscale field from GFS (Global Forecast System) and WRF (the Weather Research and Forecasting Model) and the Eulerian system **WRF-chem** that couple the WRF meteorological information with chemistry[1]. The geographical location of all the measurements site, airborne and mobile lab tracks, are reported in figure 2.1

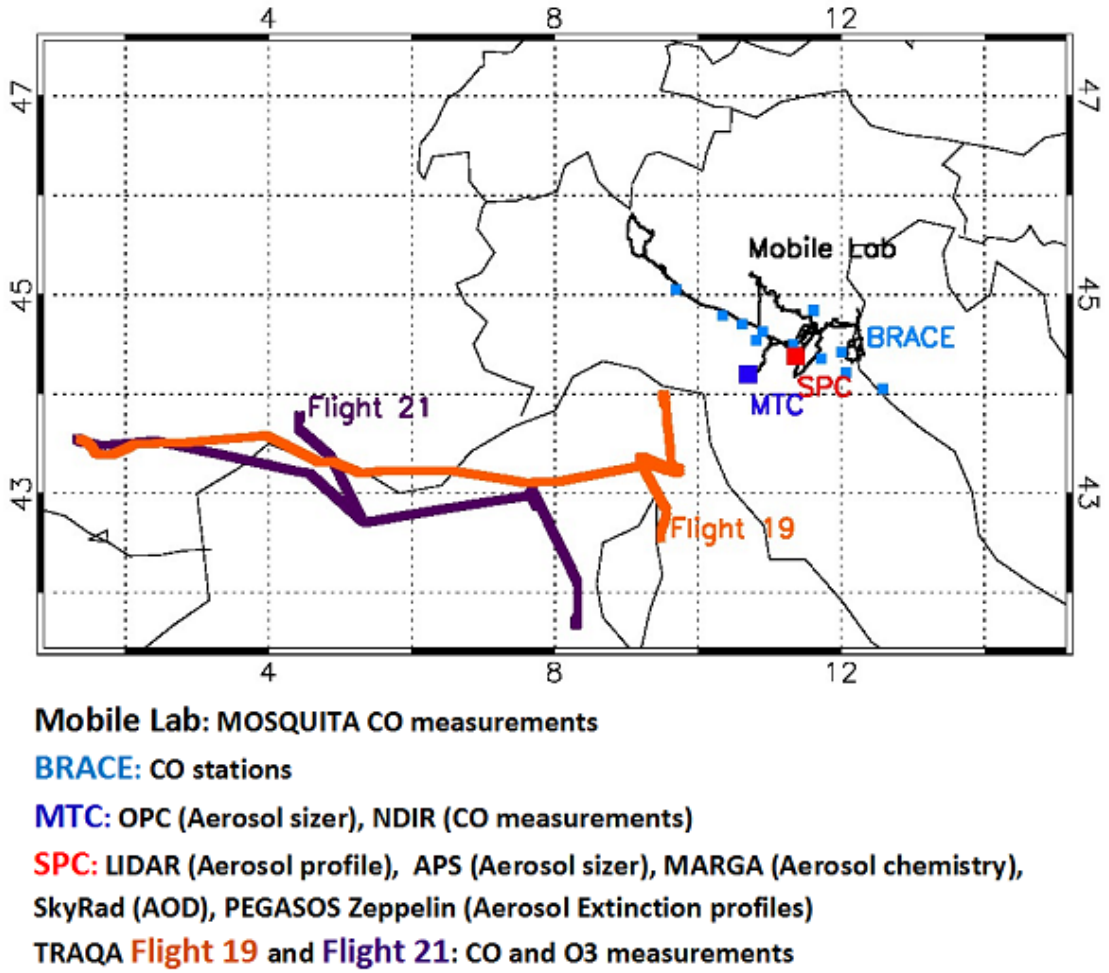

Figure 2.1: Geographical locations of SPC and MTC measurement sites, BRACE stations, mobile lab track and TRAQA flights 19 and 21 patterns

[1]A fluid flow (in that case atmospheric air) may be described in two different ways: the Lagrangian approach and the Eulerian approach. In the Lagrangian approach the air parcel is followed as it moves in the flow. Is possible then to describe the pathline of the parcel. The Eulerian approach, observing the flow passing through a fixed non-moving box in the space, is used instead to obtain a picture of the flow in one particular instant. The lines comprising this flow field are called streamlines

San Pietro Capofiume Station The San Pietro Capofiume (hereafter SPC) station (44°39'0" N, 11°37'0" E, 11 m a.s.l) is located in the South – Eastern part of Po Valley at a flat rural background site (see figure 2.2) of Emilia-Romagna. This region of Italy is characterized by a dense network of primary and secondary roads. SPC is moreover situated close to two major Po Valley cities: Bologna

Figure 2.2: San Pietro Capofiume site, www.arpa.cnr.it

25 km to the South, with over 300 000 inhabitants, heavy industry, and a major transportation hub and Ferrara, 20 km to the north, with 130 000 inhabitants and food and machinery industry. The geographical location of the SPC site makes it therefore ideally suited also for anthropogenic pollution studies. SPC was selected as a site for a WMO (Word Meteorological Organisation) station as, being located in a flat region (horizontally homogeneous at local scale), the collected in-situ data could be also considered as representative of the surrounding wider region, from the Apennines chain to the Adriatic sea. Several campaigns have taken place at the SPC site focusing on variations in chemical composition as well as hygroscopic and optical properties and showing that the site is subject also to long range transport and aged aerosol from distant pollution sources [156, 40]. De Cesari et al. (2014) [40], showed for instance that organic aerosol mass observed on SPC was accounted for 38% by anthropogenic aerosols accumulating in the lower layers during night, for 21% by local aerosols recirculated in residual layers while the 41% was related to the most aged aerosols imported from transalpine areas. Moreover some events of mineral dust events over the site, observed as large increases in coarse particle volume, were also identified [14, 100]

Mount Cimone Station The climate Observatory "O. Vittori" (ICO-OV) of Mt. Cimone (hereafter MTC)(44°12' N, 10°42' E, 2165 m asl) is located at the summit of the Northern Italian Apennines and it is characterized by a 360° free horizon (see figure 2.3). Moreover it is situated on the border line of two different climatic regions: the continental Europe (northwards) and the Mediterranean Basin

(southwards). Because major towns (i.e. Bologna, Firenze) are situated in the

Figure 2.3: Monte Cimone site, www.isac.cnr.it

lowlands about 60 km away and industrial areas are not closer than 40 km and 2 km below the Laboratory, the atmospheric measurements collected at MTC can be considered representative of the background conditions of the South European free troposphere [13]. Nevertheless, the site is subject to transport of air masses from the regional PBL (Planetary Boundary Layer). The reduced ventilation conditions, typical in the Po Valley, and favorable climatic factors promote the build-up of aerosols and pollutants at ground level over the wide basin of the Po Valley. Under stable atmospheric conditions during summer and, less intensely, in winter during daytime, thermal circulations may transport such pollution upwards to the station [38, 100]. For the scientific relevance of the atmospheric information it can offer, MTC station was included in the Global Atmosphere Watch (GAW) program of the World Meteorological Organization (WMO).

2.1 Projects involved

Observations are performed in the framework of the Supersito project by Regional Agency of Prevention and Environment, from Emilia Romagna region (ARPA-ER, Italy www.supersito-er.it), the european projects PEGASOS (Pan-European Gas-AeroSOl-climate interaction Study) and ChArMEx (Chemistry-Aerosol Mediterranean Experiment)

2.1.1 Supersito project

The Supersito project is carried out by the Emilia-Romagna region (Italy) and its Arpa (Regional agency for the environment protection, http://www.arpa.emr.it/)

with the collaboration of national and international research institutes. The objective of the project is to improve the knowledge o the environmental and health related issues related to the fine(PM2.5 e PM10) and ultrafine (smaller than PM0.1) particulate suspended in the atmosphere both in indoor and outdoor environment. The project is based on the collection of chemical, biological, physical atmospheric parameters from several distributed station in the Emilia Romagna region, located in both urban and rural sites.

2.1.2 ChArMEx project

The ChArMEx project (http://charmex.lsce.ipsl.fr) is a collaborative research program federating international activities to investigate Mediterranean regional chemistry-climate interactions. A special observing period (SOP-1a), including intensive airborne measurements, was performed in the framework of the Aerosol Direct Radiative Forcing on the Mediterranean Climate (ADRIMED) project during the Mediterranean dry season over the western and central Mediterranean basins, with a focus on aerosol-radiation measurements and their modeling. The project aimed to create an innovative database gathering the physical, chemical, optical properties as well as the vertical distribution of the main Mediterranean aerosols, to estimate the direct radiative forcing and the forcing efficiency of different aerosols with their implications on the radiative budget effects (sea-surface evaporation fluxes, relative humidity profiles, cloud-cover, precipitation and hydrological cycle) The **TRAQA** (TRAnsport et Qualité de l'Air au dessus de la Méditerranée) french campaign is part of the Charmex poject. This experiment is based on intensive aircraft and balloons measures as well as modelling to investigate pollution plumes (ageing, import/export processes between boundary layer and free troposphere, Lagrangian processes) over the Mediterranean sea. In particular it investigates the pollution outflow toward the Western Mediterranean originated form the regions of Marseille and Barcelona and the aerosol plumes coming from the European or African continent towards the Corsica island. TRAQA flights were carried out during daytime, when the chemistry, induced by sun light, favours increase in pollution levels.

2.1.3 PEGASOS project

The PEGASOS project (http://pegasos.iceht.forth.gr/) involves many of European research groups, with state-of the-art observational and modeling facilities with the main objective of quantifying the magnitude of regional to global feedbacks between atmospheric chemistry and climate and therefore identifying mitigation strategies and policies to improve air quality while limiting their impact on climate change. The project, focused on the European continent, try to bridge the spatial and temporal scales that connect local surface-air pollutant exchanges, air quality

and weather with global atmospheric chemistry and climate. The project is based on a fully integrated analysis of dynamically changing emissions, deposition and their link to tropospheric chemical reactions and interactions with climate. It includes development of new climate sensitive biogenic and anthropogenic emission models, laboratory and field process studies, development and use of the most advanced models.

2.2 Remote Sensing: LIDAR

Aerosol optical profiles were collected at the SPC station by means of a single-wavelength (532 nm) elastic LIDAR system with depolarization channel. The LIDAR (LIght Detection And Ranging) remote sensing instrument represents an high potential technique to determine either qualitatively or quantitatively the aerosol content in the atmosphere as it provides vertically extended and high temporal (order of seconds) and spatial (order of meters) resolved profiles of particulate optical properties.

2.2.1 SPC LIDAR system description

The SPC LIDAR uses Nd-YAG pulsed laser source with active Q switching. The emission has a pulse duration of 1ns with energies of 400 μJ/pulse at 532 nm (green) and repetition rate of 1 kHz. The laser beam divergence, 3 mrad from factory, is further reduced by a factor of 7 by a beam expander. The optical receiver of the LIDAR is a F/1.5 Newtonian telescope with a diameter of 20 cm and a field of view (FOV) of 0.67 mrad. Further details are described in Cairo et al. 2012 [21]. The laser and the telescope FOV overlaps between 50 m and 300 m from the system. Nitrogen Raman scattering channel at 608 nm, whose data are available only in nighttime conditions, is used for the experimental correction of the signal coming from this region of Partial Overlap Region (POR) between laser and telescope FOV. The Raman signal is in fact proportional to the molecular density [142]. Taking the molecular density profiles from radiosoundings or models lead therefore to evaluate the effect of the POR on the signal. This correction allows the reconstruction of the lidar profile down to around 100 m with an acceptable uncertainty (close to 10%) on the backscatter ratio that rapidly decreases with height (see figure 2.4).

The LIDAR used in the present study is a small portable one and the weak intensity of the Raman signal does not allow to extend the Raman profile much beyond the 2 km range mantaining a satisfactorily signal-to-noise ratio[2], so it is not possible to use it for a Rayleigh-Raman extinction retrieval, as usually done on larger and more performing lidar systems. Raman profiles are thus acquired once,

[2]signal-to-noise ratio, often referred as SNR, is a measure of signal strength relative to background noise

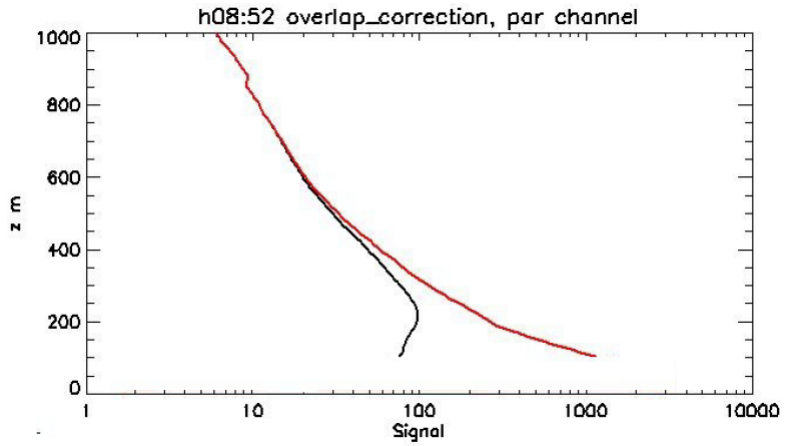

Figure 2.4: Example of POR correction on a single parallel channel profile. Black line represent the raw signal, the red line is the signal after the POR correction. The profile is cut at the minimum height of 100m, where the correction produces uncertainty of 10%

during the lidar setup and alignment, with the scope of partial FOV reconstruction. The backscattered light is collimated and split into parallel and cross polarized components with respect to the laser emission. The backscattering signal is acquisited by photomultipliers whose signal is simultaneously recorded both in current and in photocounting mode. In current mode the signal is digitalized with a sampling time of 50 ns, for a total of 1024 samples, providing a reconstruction of the vertical profile with a resolution of 7.5 m for a vertical extension of 7 km. In photoncounting mode, the single photon detections are counted for ulterior 1024 sampling with a time window of 100 ns length, obtaining the vertical profile up to 15 km with a resolution of 15 m. A region of superposition between current mode and photoncounting mode allows merging the two acquisition modes to reconstruct the whole backscattering profile from the ground to the top of the sounding. For the purpose of this thesis the lidar profile analysis was limited to the first 5 km above ground level (a.g.l.) and therefore to the only current mode. The system provides a profile every 5 minutes, by averaging the signals over 300000 laser shots. The principal technical specification are summarized in table 2.1. A scheme of the system is presented in figure 2.5.

2.2.2 Physical principle

According to Bouguer-Lambert-Beer law [204] the intensity of a laser beam propagating along the $\vec{r}$ direction between distances r = 0 and r = R of an inhomogeneous medium is given by:

$$\frac{I(\lambda)}{I_0} = T(\lambda, R) = exp\left[- \int_0^R \alpha(t, \lambda) dr \right] \tag{2.1}$$

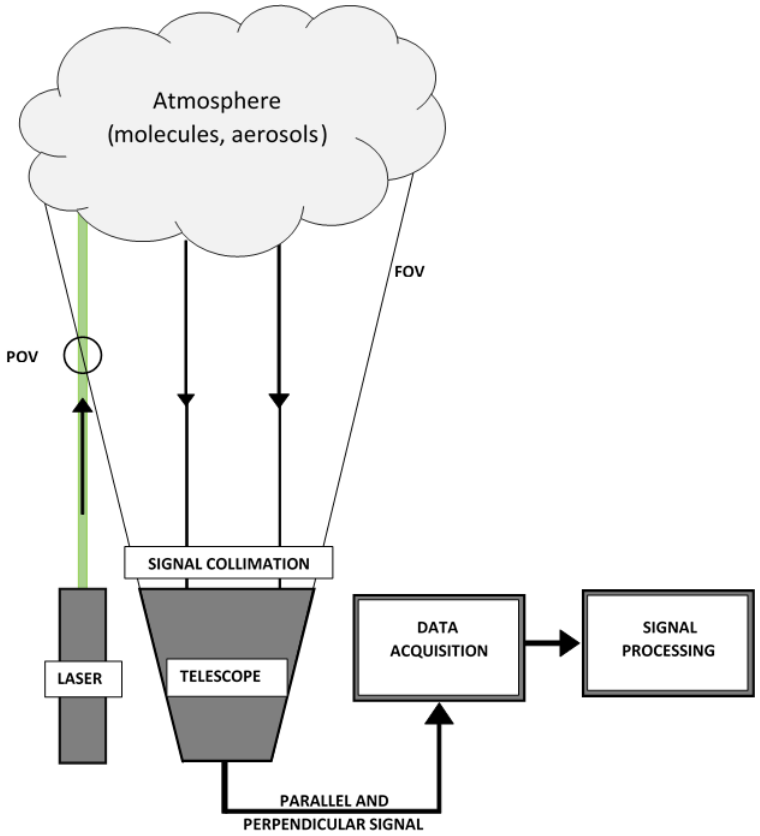

Figure 2.5: Schematic representation of the LIDAR system

Table 2.1: SPC LIDAR specifications

Wavelenghts used	532nm (with polarization channel)
Laser type	NdYAG
Pulse duration	1 ns
Laser repetition rate	1kHz
Laser output energy	400 μJ
Receiver	F/1.5 Newtonian telescope
Telescope FOV	0.67mrad
Vertical resolution	7.5m <7 Km and 15m >15 km
Temporal resolution	5 minutes

where I_0 is the initial intensity at r = 0, I is the intensity at r = R, λ is the operating wavelength, α is the atmospheric extinction coefficient [km^{-1} if r is in km], and T(λ,R) is the one-way transmittance at the [0,R] interval. The extinction term is a combination of three simultaneous phenomena: molecular absorption, molecular or Rayleigh scattering (when the size of the scatterers a is much lower than the signal wavelenght λ:$\frac{2\pi a}{\lambda} \ll 1$), and particulate or Mie scattering (size of the scatterers comparable to the signal wavelenght :$\frac{2\pi a}{\lambda} \approx 1$):

$$\alpha = \alpha_{m,abs} + \alpha_{m,sct} + \alpha_{a,sct} \tag{2.2}$$

where the subscripts "m" and "a" indicates respectively molecules and aerosol (or particles) while "abs" stands for absorption and "sct" for scattering. Rayleigh and Mie scattering are usually indicated as elastic scattering, because they do not shift the wavelength in the interaction with the signal. Rayleigh scattering is largest in the ultraviolet while Mie scattering is roughly wavelength independent, usually much larger than Rayleigh scattering at visible and infrared wavelengths and strongly determined by the size distribution and particle number density. So, chosing these range of wavelengths for the LIDAR measurements, absorption and Raman scattering (usually termed inelastic scattering as it shifts the return wavelength caused by rotational transition in molecules) terms became much weaker than the elastic scattering terms and can be neglected in the computation of the total extinction [75, 82]. The dominant backscattering radiation comes therefore from the airborne constituents and conveys information about the atmospheric state in terms of a range dependent amplitude signal. The backscattering signal is derived by solving the so-called LIDAR equation:

$$N(r) = \frac{E \cdot C \cdot \beta(r)}{r^2} \cdot \exp\left(-2 \cdot \int_0^r \alpha(r)dr \right) = \frac{E \cdot C \cdot \beta(r)}{r^2} \cdot T(r) \tag{2.3}$$

Where N(r) indicates the measured quantity (the number of photons backscattered at a distance r in case of photoncounting detection, or a current directly proportional to them in case of current detection), E is the energy of the laser pulse, C a parameter that describes the overall efficiency of the system, T(r) term represents the two-way transmittance through the r range, $\beta(r)$ the the backscatter coefficient and $\alpha(r)$ the atmospheric extinction.

As explained before, both the backscattering and extinction terms receive a contribution from the molecular and the aerosol components:

$$\alpha(r) = \alpha_m(r) + \alpha_a(r) \tag{2.4}$$

$$\beta(r) = \beta_m(r) + \beta_a(r) \tag{2.5}$$

Basing on that is possible to define the Backscatter Ratio quantity (R):

$$R(r) = \frac{\beta(r)}{\beta_m(r)} \tag{2.6}$$

The R quantity defined above is therefore $R = 1$ in absence of aerosol and $R>1$ otherwise. This quantity can be directly derived solving the 2.3:

$$R(r) = \frac{N(r) \cdot r^2}{E \cdot C \cdot \beta_m(r) \cdot T(r)} \tag{2.7}$$

E and C parameters depend on the system characteristics but are removed from the equation by calibration: the signal is calibrated in a region (r_0) supposed to be free from aerosol ($R(r_0) = 1$). Once this is done is possible to retrieve R(r) and therefore also:

$$\beta_a(r) = (R(r) - 1) \cdot \beta_m(r) \tag{2.8}$$

As atmospheric molecules are smaller than the wavelength typically used in lidar system the molecular contribution β_m can be evaluated from the Rayleigh theory once the air density profile is obtained from measurements or from a suitable atmospheric model (in our case from the ERA40 reanalysis[3]).

The presence of a polarization channel in the LIDAR system allows to evaluate an additional parameters, the volume linear depolarization ratio δ. This can be defined as:

$$\delta = \frac{\beta_{perp}}{\beta_{par}} \tag{2.9}$$

where β_{perp} and β_{par} are the backscattered signal components with polarization perpendicular and parallel to the polarization of the emitted light. This parameter is widely adopted for aerosol (and cloud phase) discrimination as it gives information on the sphericity of the particles (the higher δ is, the higher is the level of asphericity) [42, 78, 196]. Because of the presence of the cross depolarized channel, a further calibration is needed. This is accomplished again choosing an atmospheric region where the presence of aerosol can be considered negligible (so that depolarization comes from molecules alone) and therefore setting δ to a theoretical value δ_m. For this analysis it was fixed to 1.4% [9].

A solution of the lidar equation for both the atmospheric extinction coefficient α_a and the atmospheric volume backscatter coefficient $\beta_a(r)$ is not possible from a single backscatter channel (unless a synergic Raman lidar channel is used, that is not the case). Consequently, it is necessary to introduce a priori assumptions on the exctinction-backscatter relation to derive the extinction profile. Usually assumptions

[3]https://climatedataguide.ucar.edu/climate-data/era40

are made on the values of Lidar Ratio (LR):

$$LR(r) = \frac{\alpha_a(r)}{\beta_a(r)} \tag{2.10}$$

In such assumptions lie the largest source of inaccuracy in lidar retrievals. Changes in the values of LR have two consequences:

- a total decrease on the backscattering coefficient profile $\beta(z)$ (and the backscatter ratio profile R(z)) with increasing LR, with more marked effects going further down in height from the calibration altitude;
- a variation on the extinction ($\alpha(z)$) retrieval in correspondence of variation of LR along the profile, as ($\alpha(z)$) is simply linearly proportional to the backscattering coefficient and LR ($\alpha(z) = LR \cdot \beta(z)$).

These effects are highlighted in the example profile of figure 2.6 from the SPC LIDAR system that show the scattering ratio (R(z)) and the extinction coefficient $\alpha(z)$ profile during an event of saharan dust transport (visible as an increase in the signal around 4 km of height)

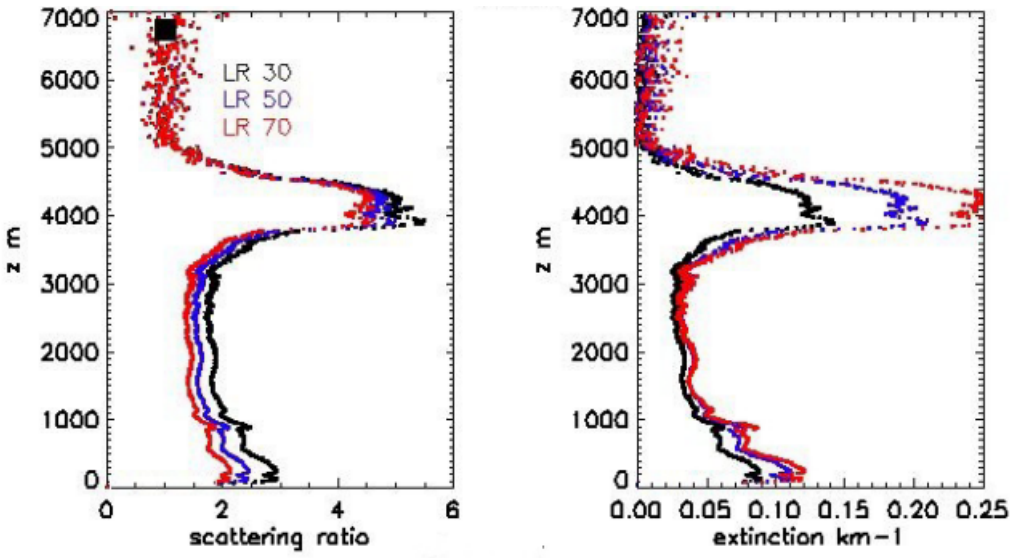

Figure 2.6: Left panel, Scattering ratio (R(z)), right panel extinction coefficient($\alpha(z)$). Red, blue and black show respectively the 70, 50 and 30 LR choice. Black square represent the calibration altitude range

In the case of figure 2.6, the first effect on R(z) (left panel) can be seen as an increase of the scattering ratio, intensified at lower heights from the calibration altitude: it is in fact not visible above 500m but causes a 50% variation on the aerosol scattering ratio R(z) in the lower point. As expected, the larger is the LR, the smaller is the R(z). On the extinction profiles (right panel) is instead visible the second effect: the larger the LR the higher the $\alpha(z)$ value. This happens more markedly in correspondence with Saharan dust layer, (here centered at 4 km), with

variation of 100% going from 30 to 70 sr, while the variation is slightly less in the lower layers (around 50%).

For this study the standard Klett approach was adopted [84]: different (fixed) values of LR were assigned to regions where clouds or aerosols are present. Such regions are automatically identified by inspecting the values of R, altitude and δ and fixing threshold taken from the literature. Thin liquid and ice clouds regions are assigned respectively with LR=20 sr and LR=30 sr [30, 123], desert dust is associated with LR=50 sr [113] while continental pollution (biomass burning aerosol) with LR of 60-70 sr [114, 49, 50].

The threshold values chosen for the LR assignment are reported in table 2.2

Table 2.2: Lidar Ratio (LR) assumption

LR (sr)	**R**	δ(%)	**z(m)**	**Aerosol Type**
70	1.05 >R <10	δ <10%		Polluted continental
50	1.05 >R <10	δ >10%		Saharan dust
30	R >10		z >6000m	Ice clouds
20	R >10		z <6000m	Liquid clouds or haze

An comparison study of LIDAR profiles for different LR values with indipendent measurements of aerosol extinction is presented in Appendix A.

2.2.3 Aerosol Classification

Lidar observations have been extensively used to identify dust layers and discriminate among different typologies of aerosols. Generally such classification is based on a choice of specific ranges of optical parameters considered representatives of a certain aerosol types. Examples are shown in Burton et al. 2012 [19], where the classification among 8 different types of aerosol is derived from total depolarization ratio δ, LR and the color ratio[4] (CR), and Groess et al. 2013 [65] where, basing on lidar ratio LR and aerosol depolarization δ_a, a distinction among sea-salt, dust and mixed dust aerosol types is made. Even if is not possible, from the analyzed LIDAR system, to obtain an estimate of the LR (not having a continuos Raman channel) or of the CR (having a single wavelenght channel), an aerosol discrimination can still be performed basing mainly on δ_a. The parameter δ_a is the depolarization related to the only contribution of the particles. It can be estimated from the scattering ratio R and δ[18]:

$$\delta_a = \frac{\delta \cdot (R + R \cdot \delta_m - \delta_m) - \delta_m}{R - 1 + R \cdot \delta_m - \delta} \tag{2.11}$$

[4]ratio between the backscatterig coefficient β at two different wavelenght: $CR = \frac{\beta_{532nm}}{\beta_{1064nm}}$

δ_m is the depolarization ratio of the atmospheric molecules (taken as 1.4%, as already stated in section 2.2.2). Differently from the total depolarization ratio δ, which value depends on the density of aerosols (decreasing, for example, as the aerosol concentration decrease), aerosol depolarization δ_a depends only on the morphology of the particles. δ_a, in fact, shows well-defined different values for certain typologies of aerosol. For example, for a 532nm wavelenght signal, values of aerosol depolarization around or higher than 30% are generally associated to layers of nearly pure dust [176, 92, 55] while smaller values (around 8–10 %) are often shown in correspondence of mixture of dust and spherical particles [115, 176, 180]. By contrast, smoke and other anthropogenic aerosol are usually found to be related to low values of aerosol depolarization (less than 5% [178, 65]). A basic classification, depending on δ_a and R values, is then implemented on the SPC LIDAR profiles in order to characterize the vertical and temporal aerosol variability over the region during the campaign (15 June 2012 - 5 July 2012) . Figure 2.7 reports the probability density function (PDF) for the whole measurements period, as a function of the parameters 1-1/R (ranging from 0 in aerosol free condition to 1 when R tends to infinity) and δ_a.

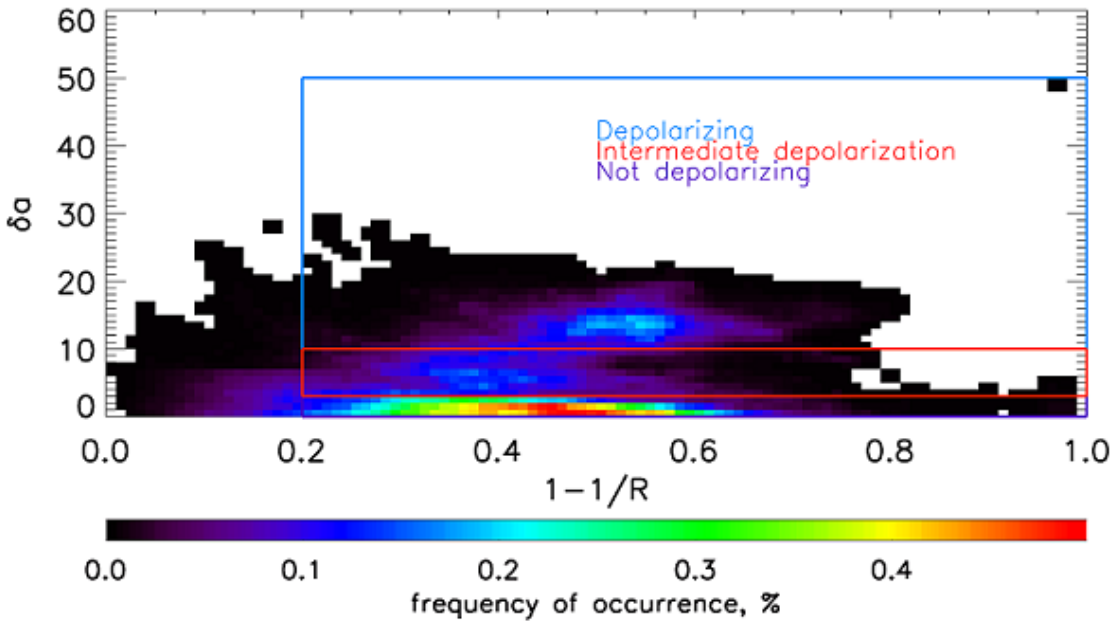

Figure 2.7: PDF of aerosol properties over the 15 June 2012-5 July 2012 period on the 1-1/R and δ_a parameters. Colors indicate the frequency of occurrence. The relative mean error on δ_a profile is found to not significantly affect the aerosol classification (see Appendix B)

Observing the distribution, and taking 0.2 as a minimum value for 1-1/R to indicate the presence of an aerosol layer, is possible to identify two main clusters of occurrence and a transition class with intermediate aerosol properties:

1. **Not depolarizing** aerosol: δ_a <3% and 1-1/R ranging between 0.2 and 1. This values of depolarization are indicative of spherical particles; based on the

above references such aerosol may be composed of anthropogenic pollution and, for the higher values of R, by droplets.

2. **Depolarizing** aerosol: δ_a >10 % and 1-1/R ranging between 0.2 and 1. This value of depolarization, accordingly to other classifications (see references above), can be considered as a miminum threshold for dust or mixed-dust particles.

3. **Intermediate Depolarizing** aerosol: 3% <δ_a <10% and 1-1/R ranging between 0.2 and 1. For this class the information provided by the LIDAR are not enought to indicate a dominance of a defined aerosol type and is therefore necessary to integrate them with additional observations.

The boxes in figure 2.7 define the regions of aerosol properties discrimination and indicates the parameters ranges chosen to identify each class. This classification is then applied to derive an aerosol mask for the whole campaign: this is shown in figure 2.8 (upper panel), together with the profiles of 1-1/R (medium panel) and δ_a (lower panel).

Overall, spherical particles (Not depolarizing type) are dominant throughout the campaign in a continuous layer from ground to 2000 m height, and they are associated with enhanced values of R (parameter 1-1/R ranging between 0.4 and 0.6). Two events of depolarizing aerosol (19 June – 21 June and 29 June – 02 July), likely dust, are observed between 2000m and 5000m. Dust events are also clearly visible in R in the free troposphere with values of 1-1/R ranging from 0.6 and 0.8. The intermediate class is individuated in close proximity of the depolarizing aerosol and within the PBL. Here it would be difficult to discern, basing only on the LIDAR parameters, if the enhanced depolarization is related to an effective descent of dust. The observed coherent vertical and time distribution of the intermediate type indicates, on a qualitative basis, that this may be due to mixing of dust with local spherical particulate. Intermediate values are also observed in coherent patterns after 12 UTC (Universal Time Coordinate) between 0 and 1500 m height for a majority of dust-free days. The integration with additional observations and the meteorological context, provided in the following part, allows to further investigate the nature of the different classes of particles.

2.3 In-situ measurements

2.3.1 Aerosol Measurements

Optical Particle Counter The in-situ aerosol number concentration at CMN were derived from an Optical Particle Counter (OPC). The OPC (Grimm, Particle Size Analyzer Mod. 1.108) provides particle counts in the diameters (Dp) range

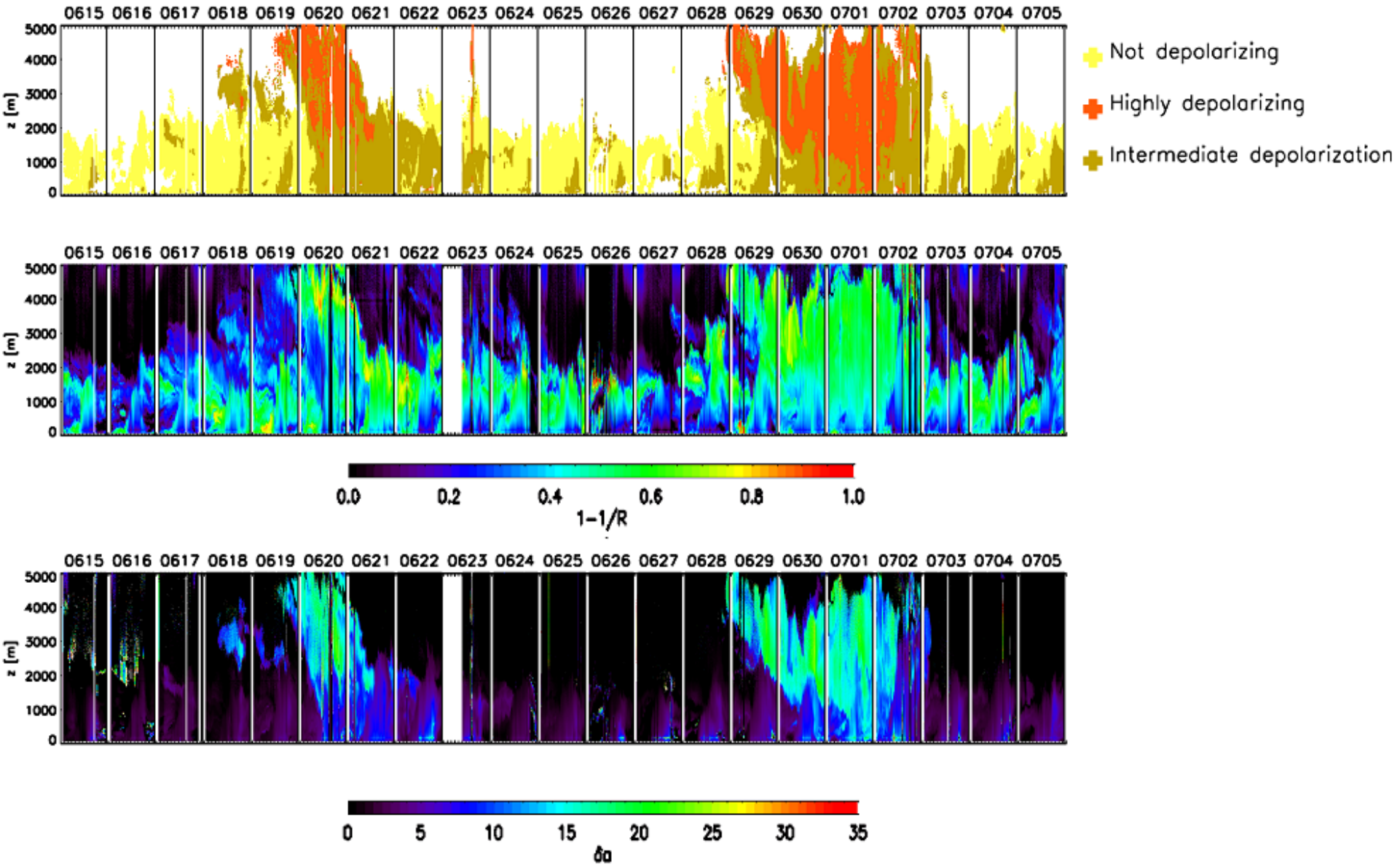

Figure 2.8: LIDAR Profiles along the whole campaign. Upper panel: vertical profiles of aerosol types resulting from the classification of figure 2.7. Yellow dots represent the not depolarizing class, the orange one is the depolarizing class and the brown is the class with intermediate properties. Medium panel: vertical profiles of 1-1/R. Lower panel: vertical profiles of δ_a

0.3μm<Dp<20μm. The instrument is based on the quantification of the 90° scattering of light by aerosol particles. According to the specifications, the reproducibility of the OPC in particle counting is ±2% [146]. An estimate of the total error affecting the data is provided in Appendix B. Such measurements allow the determination of the fine (0.3μm<Dp<1μm) and coarser (1μm<Dp<20μm) aerosol fractions with a 1 minute time resolution

Aerodynamic Particle Sizer Aerosol concentration at the ground at SPC were provided by an Aerodynamic Particle Sizer model 3321 (APS spectrometer) that collects high-resolution, real-time aerodynamic measurements of particles from 0.5 to 20 microns. The aerodynamic diameter is defined as the physical diameter that a unit density sphere will have if settles through the air with a velocity equal to that of the particle observed. The aerodynamic diameters of particles is estabilished measuring their transit time between two estabilished point when accelerated singly through a well-defined flow field. Data are collected with a time resolution of 10 minutes. Error analysis on the data collected is discusses on Appendix B.

MARGA The Monitor for AeRosol and GAses (MARGA) is a fully autonomous sampling and measurement system that continuously measures the gases and aerosol components that might have a direct effect on air quality. The analytical system is capable of quantifying anions and cations in aerosols and water soluble gases simultaneously. First the gases are absorbed in a Wet Rotating Denuder device and then separated from aerosols in a Steam-Jet Aerosol Collector. Two ion chromatographs detect and analyze the collected gas and aerosol samples with high accuracies to reach detection limits as low as 0.01 μg/m3. Air is collected into the MARGA analyzer through a size-selective particle separator. Thus the size of the particles for analysis can be limited to a diameter of less than 10 (PM10) or 2.5 (PM2.5) μm. The aerosol ions measured are CL-, NO3-, SO42-, NH4+, K+, Ca2+, Mg2+, Na+. The instrument has a time resolution of 1 hour.

Sky Radiometer Columnar optical properties at the SPC station is measured with a POM-02 sky radiometer. The instrument gathers measurements of direct sun irradiance and sky radiance within a 1° full field of view at 11 wavelengths (ranging from 315 nm to 2200 nm) and a time resolution of one minute. Diffuse radiances from the sky and direct sun irradiances are processed with the SKYRAD algorithm [118] employed to process the radiance measurements to retrieve the aerosol optical depth (AOD), the Angstrom exponent, the single scattering albedo, the complex refraction index and the asymmetry factor [43]. In this work the AOD from the Sky Radiometer will be compared with the AOD derived by the LIDAR. In-situ calibration is provided by the improved Langley technique [22]. The maxium absolute error for AOD is found to be 0.05 [43]

Zeppelin NT Within the PEGASOS project a Zeppelin NT ("New Technology") was adopted as a measurement platform to detects variations of aresol properties in air masses layers inside the convective Planetary Boundary Layer (PBL) over Europe. A WHite-light humidified Optical Particles Spectrometer (WHOPS), together with an aethalometer and an Aerosol Mass Spectrometer (AMS) were mounted in the Zeppelin NT to investigate optical properties like aerosol size distribution, hygroscopic growth factor, effective index of refraction and light absorption coefficient, and observe chemical composition. More deteails, as well as the general set-up of the Zeppelin NT platform for aerosol measurements, are described in Rosati et al. (2015b) [150]. Aerosol extinction profiles derived from the Zeppelin mesurements will be compared with the LIDAR ones.

2.3.2 CO Measurements

BRACE stations The BRACE (Banca dati Relazionale Aria Clima Emissione) database collects air quality measurements in all the Italian regions and makes the data available on the web (http://www.brace.sinanet.apat.it/).Information is collected at local and regional level and are then transmitted to the Superior Institute for the Environmental Protection and Research (Istituto Superiore per laProtezione e la Ricerca Ambientale, ISPRA) then to the European Environment Agency (EEA) and finally archived on the european database AIRBASE. Information on the network, the stations and the measurement sensors as well as the pollutants concentrations data are collected at the national database of BRACE [26].

non-Dispersive Infrared analyser Carbon monoxide at the CMN station is measured by using a non-Dispersive Infrared (NDIR) analyser (Thermo Scientific TEI 48C-TL). Two CO standards (approx. 10 ppm, synthetic air, Messer Italia) are used to calibrate the instrument with a dilution system. The analytical principle is based on absorption of Infra Red (IR) light by the CO molecule. As CO has a sufficiently characteristic IR absorption spectrum (CO absorbs IR maximally at 2.3 and 4.6 um) the absorption of IR by the CO molecule can be used as a measure of CO concentration in the presence of other gases. The instrument has a time resolution of 30 minutes and a relative error that is estimated to be of 10%.

Mobile lab: MOSQUITA Ground CO measurements across the Po Valley were provided by the Paul Scherrer Institute mobile laboratory[5] named MOSQUITA (Measurements Of Spatial Quantitative Imissions of Trace gases and Aerosols). The lab is equipped with a suite of instruments to characterize the chemical composition and physical properties of aerosols as well as trace gases at high time resolution (2s) and a Global Positioning System (GPS) to track the driving routes. The CO

[5]https://www.psi.ch/lac/mobile-laboratory

concentration were collected by an Aero-Laser (model AL5002). This instruments allows a fast CO monitoring with a sensitivity below 1ppb (parts per billion). Relative error on the data is estimated to vary between 5% and 10%. The detection of CO is based on a fluorimetric method, employing the excitation of CO at 150nm.

TRAQA flights During the TRAQA (TRansport and Air QuAlity) campaign a total of 17 flights were measured up to 5000 m above sea level over an extended area (40–45 °N and 2° W–12° E) including the Gulf of Genoa, southern France, the Gulf of Lion, and the Spanish coast in the period 20 June–13 July 2012. Research flights were performed with the SAFIRE (Service des Avions Français Instruments pour la Recherche en Environnement, http://www.safire.fr/) tropospheric aircraft ATR-42. The basic equipment of the ATR-42 aircraft includes sensors for the measurements of meteorological parameters (pressure, temperature, relative humidity, wind components), radiative fluxes (down- and up-welling shortwave and longwave radiation), and carbon monoxide (CO) and ozone (O3) mixing ratios. Carbon monoxide (CO) and ozone (O3) mixing ratios were measured by the MOZART instrument described in detail by Nedelec et al. (2003)[120]. The CO analyser is an improved version of a commercial Model 48CTL from Thermo Environmental Instruments, based on the Gas Filter Correlation principle of infrared absorption by the 4.67 μm fundamental vibrationrotation band of CO. The O3 measurement are coming from a commercial fast response ozone analyzer (Model 49C TEI Thermo Environment Instruments) that is based on classic UV absorption at 254 nm. CO and O3 are measured at a resolution of 30 and 4 s, respectively. The nominal uncertainty is ±5% for CO and ±2% for O3 [120].

2.4 Numerical simulations

2.4.1 Lagrangian simulations: FLEXPART

We make use of the FLEXPART ("FLEXible PARTicle dispersion model") Lagrangian transport and dispersion model(version 9.02) to characterize the air masses transport (Stohl et al., 2005 [174] and references therein). Lagrangian particle models compute trajectories and concentrations of infinitesimally small atmospherical parcels. The tracers can be released from point, line, area or volume sources. It can also be used in a domain-filling mode where the entire atmosphere is represented by particles of equal mass. In addition, the resolution of a Lagrangian model can be infinitesimally small. Particles trajectories calculation is basically obtained by the integration of the trajectory equation:

$$\frac{d\mathbf{X}}{dt} = \mathbf{v}[\mathbf{X}(t)] \tag{2.12}$$

using the simple "zero acceleration" scheme

$$\mathbf{X}(t + \Delta t) = \mathbf{X}(t) + \mathbf{v}(\mathbf{X}, t)\Delta t \tag{2.13}$$

where t represents the time, Δt the time increment, (X) the position vector and (v) the wind vector. This one is composed by the grid scale wind $\bar{\mathbf{v}}$, the turbulent wind fluctuations $\mathbf{v}_t$ and the mesoscale wind fluctuations $\mathbf{v}_m$:

$$\mathbf{v} = \bar{\mathbf{v}} + \mathbf{v}_t + \mathbf{v}_m \tag{2.14}$$

The $\mathbf{v}_t$ components are parameterized assuming a Markov process based on the Langevin equation [183]:

$$v_{t_i} = a_i(\mathbf{X}, \mathbf{v}_t, t)dt + \sum_j b_{ij}(\mathbf{X}, \mathbf{v}_t, t)dW_j \tag{2.15}$$

where $\mathbf{a}$ is the drift term, $\mathbf{b}$ the diffusion term and dW_j are the uncorrelated in time incremental components of a Wiener process with zero mean and variance dt [87]. Particle transport and turbulent dispersion are handled by the model with procedures that interpolate winds and other data to the particle position and the Langevin equations are solved. The mesoscale components instead is not directly resolved by the ECMWF data nor covered by the turbulence parameterization so it needs to be taken into account in an approximate way, solving an independent Langevin equation for the mesoscale wind velocity fluctuations basing on the method of Maryon (1998) [101] with the basic assumption that the variance at the grid scale provides some information on its subgrid variance.

FLEXPART, largely adopted for the simulation of long-range and mesoscale transport and diffusion of atmospheric tracers, can also take in account the loss processes such as dry and wet deposition or radiactive exponential decay [174]. Other applications range from the dispersion of radionuclides, over the establishment of flow climatologies, to the analysis of Earth's water cycle. FLEXPART also produces output suitable for inverse determination of emission sources, e.g., of greenhouse gases or volcanic ash. The trajectories can be run both forward in time to study the dispersion of tracers from their sources, and backward in time to find a possible contributing sources for a receptor. The model has been validated using large-scale tracer experiments [173, 54]. In addition to the reference version of FLEXPART, which is based on meteorological data from ECMWF (European Centre for Medium-Range Weather Forecasts, http://www.ecmwf.int/) and GFS (Global Forecast System, https://www.ncdc.noaa.gov/), several branches of FLEXPART have been developed, which can be run with meteorological data from mesoscale models (like WRF, COSMO and MM5, see http://transport.nilu.no/flexpart/flexpart-and-flextra-users). For our purposes, the model has been run with pressure level data

from NCEP-GFS (rda.ucar.edu) when analysing intercontinental transport (i.e. dust advection from Africa). Flexpart-WRF version developed by Briuode [17], was instead used with the output of the mesoscale Weather Research and Forecasting (WRF) model (http://www.wrf-model.org/) when studying regional level transport processes. The Global Forecast System (GFS, https://www.ncdc.noaa.gov/) is a weather forecast model produced by the National Centers for Environmental Prediction (NCEP). This dataset includes several atmospheric and land-soil variables, from temperatures, winds, and precipitation to soil moisture and atmospheric ozone concentration. The GFS simulations covers the entire globe with a base horizontal resolution of 18 miles (28 kilometers) between grid points. Data con be downloaded from http://rda.ucar.edu/datasets/ds094.0/. Meteorological data input for FLEXPART-WRF were instead obtained by WRF-CHEM runs. The model and its main configuration settings are described in the following section.

2.4.2 Eulerian Simulation: WRF and WRF-CHEM

The WRF model is a fully compressible and Euler non hydrostatic model. It has two dynamical cores: The Advanced Research WRF (ARW) and Nonhydrostatic Mesoscale Model (NMM). The availability of different possible physical parameterization makes it suitable to simulate atmospheric processes over a wide range of spatial and temporal scales [48]. WRF can generate atmospheric simulations using real data (observations, analyses) or idealized conditions. The dynamical cores include mostly advection, pressure gradients, Coriolis, buoyancy, diffusion and respects mass and scalare conserving flux. Vertical coordinates are terrain-following hydrostatic pressure coordinate with the top of the model being a constant pressure surface. WRF has been developed by a large collaborative partnership and is supported by several research centers, among them the National Center for Atmospheric Research (NCAR), the National Oceanic and atmospheric Administration (NOAA), the National Centers for Environmental Prediction (NCEP) and the Forecast Systems Laboratory (FSL)(http://ruc.noaa.gov/wrf/WG11/). The WRF-CHEM, the WRF Chemistry system, is a fully coupled online model [6] as it simulates trace gases and particulates simultaneously with the meteorological fields [48]: the chemistry and meteorological components of the WRF-Chem model are fully consistent with each other using same transport scheme, the same horizontal and vertical grids and the same physics scheme for the sub grid scale transport [64]. The WRF-Chem model undergoes three main phases:

1. **WRF Preprocessing System (WPS)**: The function of the WPS system is to define WRF grid, generate map, elevation and land information for WRF

[6] In an *online* modeling system, chemistry is integrated simultaneously with the meteorology, allowing the feedback at each model time step between meteorology and chemistry

(terrain, landuse, soil type etc.), De-grib GRIB files for meteorological data (u, v, T, q, surface pressure, soil data, snow data, sea-surface temperature, etc.) and interpolate the data to the WRF grid.

2. **Meteorology and emissions data initialization**: Initialize boundary and initial condition files for real or ideal data cases, does vertical interpolation to model levels, does vertical dynamic (hydrostatic) balance and does soil vertical interpolations and land-use mask checks.

3. **WRF dynamical solver (ARW or NMM) and chemistry**: This last phase uses boundary and initial conditions extracted from the previous step and runs the model simulation with the selected namelist options (such as physics and chemical choices, timestep, length of simulation, etc.)

These steps are summarized in figure 2.9

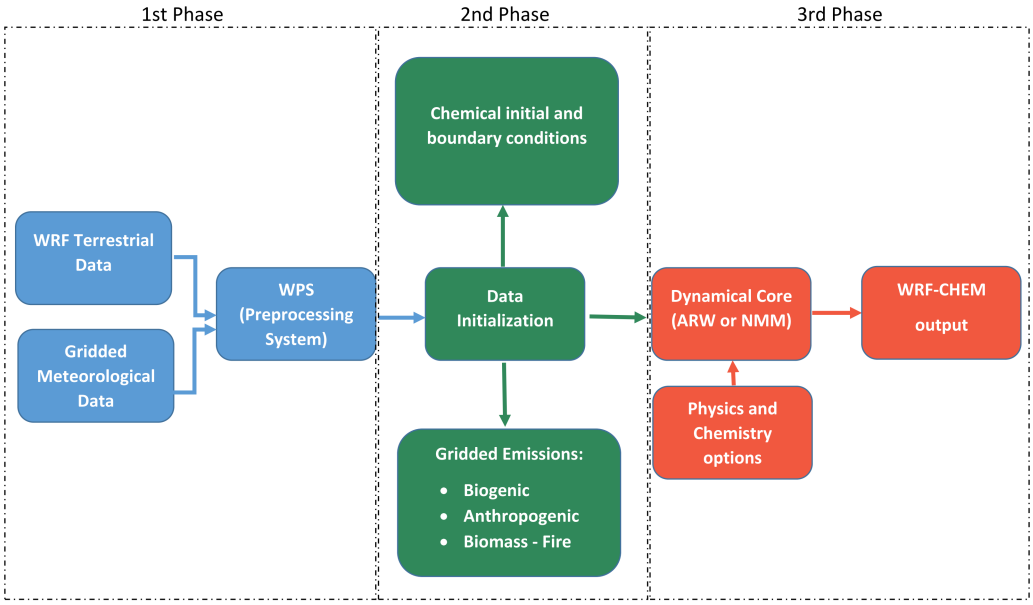

Figure 2.9: The three main phases of the WRF-CHEM simulation: 1st phase WPS; 2nd phase data initialization; 3rd phase dynamical solver

WRF-CHEM configuration[7]

Geographical settings : The WRF-Chem Version 3.5 with ARW core and real cases was employed to investigate the CO pollution plume on the Mediterranean

[7]Courtesy of Dr. Jean-Christophe Raut. The WRF-CHEM model was run by the LATMOS laboratoire in Paris www.latmos.ipsl.fr

area. The domain covers most of Italy and Spain, with a grid horizontal resolution of 10 km for a 230x140 grid. The output has 50 vertical layers with model top set at 5 hPa. The default settings include the United State Geological Survey (USGS) Terrestrial data and gridded GFS data, used as the main input parameters to the WRF preprocessing system. For this study, the National Center for Environmental Protection (NCEP) Final Analysis (FNL) data from Global Forecasting System (GFS), available at spatial resolution of 1° and temporal resolution of 6 hours (http://dss.ucar.edu/datasets/ds083.2/data/), has been used for initializing the meteorological fields in the model.

Physical settings : The physical schemes used in this study include: Morrison 2–moment microphysics Scheme [112], Rapid Radiative Transfer Model (RRTM) longwave radiation [109], Goddard shortwave scheme [31, 32], the MM5 similarity surface layer scheme [10, 44, 129, 194, 205], the Yonsei University Scheme (YSU) as Planetary Boundary Layer (PBL) Physics Options and the Unified Noah Land Surface Model [181]

Chemical settings : WRF-CHEM was run with the CBMZ (Carbon Bond Mechanism version Z) [202] chemical mechanism and MOSAIC (MOdel for Simulating Aerosol Interactions with Chemistry) model at 8 sectional aerosol bins [48, 203, 5], The model uses Fast-J photolysis schemes [197] and includes dry deposition of gas species and aerosols. The run includes anthropogenic emissions from the HTAP-v2 inventory[8]. This dataset includes emissions of CH4 (Methane), CO, SO2, NOx, VOCs, NH3 (Ammonia), PM10, PM2.5, BC (Black Carbon) and OC (Organic Carbon) for the years 2008 and 2010. HTAP-V2 uses nationally reported emissions combined with regional scientific inventories and complemented with EDGARv4.3 data for those regions where data are absent. Biogenic emissions are provided by MEGAN (Model of Emissions of Gases and Aerosols from Nature,[66, 158]), biomass burning emissions are from FINN-v1 and the simulation includes a plume rise calculation to distribute the emissions vertically. The run also includes online dust and sea salt emissions

The most relevant settings are summarized in table 2.3.

[8] $http://edgar.jrc.ec.europa.eu/htap_v2/index.php?SECURE=123$

Table 2.3: WRF-CHEM Settings

Physics	
Microphysics Scheme	Morrison 2-moment
Longwave Radiation Scheme	RRTM
Shortwave Radiation Scheme	Goddard
Surface Layer Scheme	MM5
PBL Scheme	YSU
Land Surface Model	Unified Noah

Emissions	
Anthropogenic Emissions	HTAP-v2
Biogenic Emissions	MEGAN
Biomass Burning Emissions	FINN-v1
Dust Emissions	MOSAIC and MADE/SORGAM
Sea Salt Emissions	MOSAIC and MADE/SORGAM

Chapter 3

Meteorological phases and aerosol regimes

3.1 Meteorology evolution during the campaign

3.1.1 Horizontal winds

The Meteorological evolutions over Po Valley was extensively analyzed during the period of interest (15 June 2012 - 5 July 2012) basing on the dataset of measurements collected at the SPC Supersito station. Vertical profiles, from ground up to 4km, of wind speed and direction were obtained from radiosondes (Vaisala RS92) launched each day at 00:00, 06:00 and 12:00 UTC. These profiles are shown in figure 3.1. Ground temperature at 12:00 UTC is also reported, superimposed to the wind speed profiles,

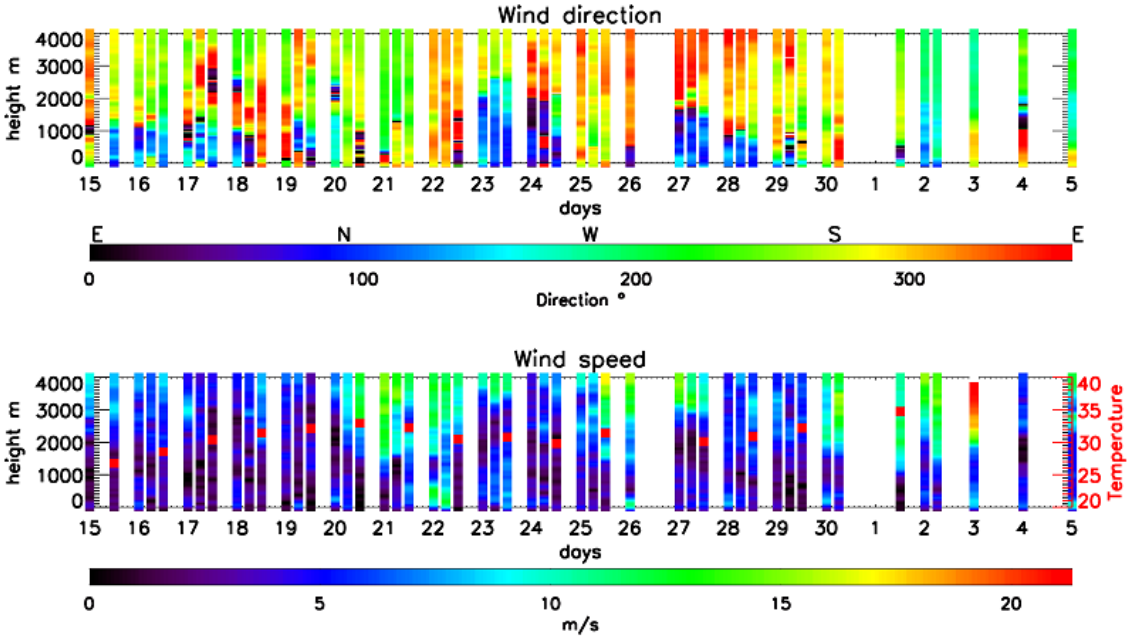

Figure 3.1: Radiosounding profiles measured at SPC: upper panel reports wind provenience direction, lower panel the wind intensity

The observation of wind profiles over SPC highlights a succession of different meteorological regimes:

1. **15th June - 19th June** This first period is characterised by a situation of stagnant conditions (wind speed less than 4 m/s below 2000m height) with a progressive warming of the air masses (up to 34°C at the ground).

2. **20th June - 21th June** During this phase higher wind speeds (between 11 m/s and 16 m/s) were observed above 2000m. Correspondingly wind direction profiles indicate a prevalent South and South-West provenience. Temperature remains above 30 °C.

3. **22th June - 29th June** Above the 2000m radiosounding profiles indicates a prevalence of South-Easterly or Easterly winds. Below this height is nevertheless possible to notice winds coming from North and North Easterly direction. This is visible in particular between the 23th and 24th June below 1000m, the 26th June below 500m (associated also to wind intensities up to 10 m/s) and the 27th June between 500m and 1800m. During this period ground temperatures first decreased to 30°C to increase again after the 27th June to 33°C.

4. **30th June - 5th July** During the last days of the campaign strong winds (between 12 and 15 m/s with a peak of 20 m/s the 3rd July) were observed above 1500 m. While the 30th June winds were coming mainly from South direction, the following days were characterized by a steering to South Westerly (1st July) and then Westerly flow (2nd and 3rd July). The 1st July ground temperatures reached a peak of 35°C.

A better understanding of the general synoptic circulation can be achieved by means of the 4-dimensional (x,y,z,t) WRF mesoscale output. A quick evaluation on the validity of the simulated wind fields has been done comparing them to the radiosoundings observations presented in figure 3.1. The corresponding WRF winds, obtained interpolating the model grid over the SPC coordinates and reported in the same color scale as figure 3.1, are presented in figure 3.2.

The comparison shows that the model reproduces correctly the vertical structure and the temporal evolution of the wind fields (as can be easily noticed in the coherent patterns of both the wind direction and wind speed time series). WRF wind intensity presents a total correlation of about 80% with the observed values and an overall root mean square error (RMSE) inferior to 2 m/s.

Figure 3.3 shows the WRF wind maps at 800hPa level (around 2000m height) over the Mediterranean basin for four different days, each one representative of the different meteorological regimes:

- panel (a), 16 June at 00:00, representative of stagnation phase (phase 1): winds over North Italy shows low intensities (less than 5 m/s) surrouded by a strong

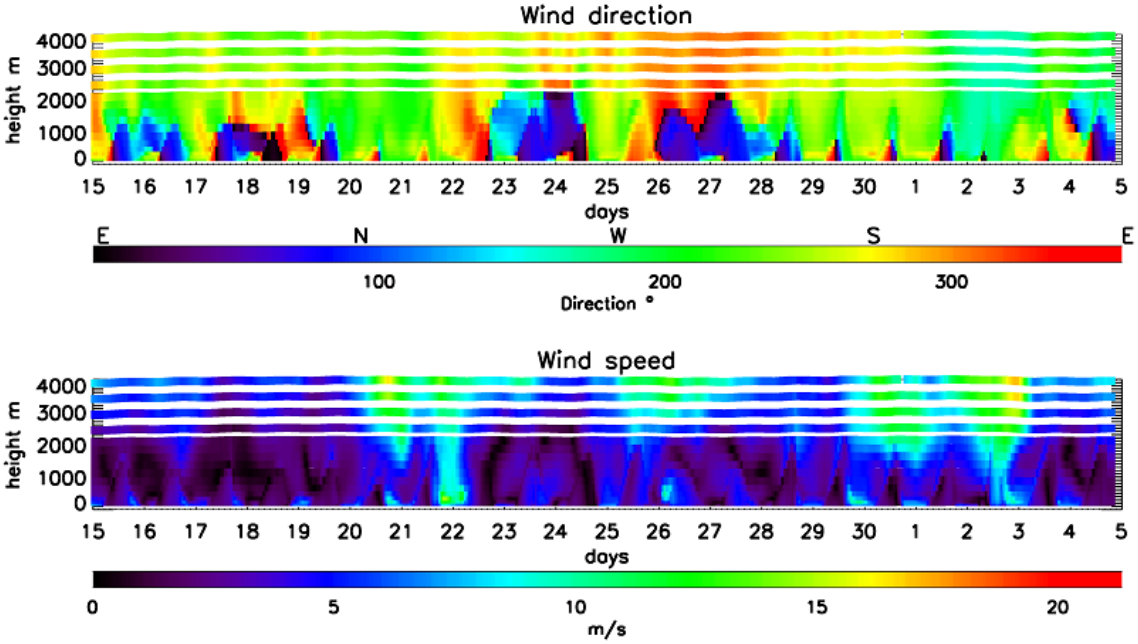

Figure 3.2: Reproduction of the wind profiles of figure 3.1 obtained from the WRF 4D wind field interpolation over SPC. Upper panel reports wind direction of provenience, lower panel the wind intensity

jet (winds intensities greater than 15 m/s) in the North-Western part of the Basin and an anticyclonic circulation over North Africa.

- panel (b), 20 June at 12:00, representative of conditions of advection from North Africa (phase 2). Air masses are transported directly from North Africa to North Italy within a wind stream of 12 to 15 m/s intensities.

- panel (c), 27 June at 00:06, representative of inversion in wind direction over Po Valley (phase 3). Wind field over North Italy is characterized by low intensity (less than 3 m/s) and a flux flowing prevalently toward South and South West. Strong South Easterly winds are present over the basin (between 5° E and 10° E)

- panel (d), 01 July at 12:00, representative of the second event of advection from North Africa (phase 4). Winds, reaching peaks of intensity higher than 15 m/s, carry air masses from Africa in a North-Easterly flux. Air masses are then advected toward Po Valley in a anticyclonic circulation centered over Italy.

3.1.2 Vertical mixing: The Planetary Boundary Layer

The troposphere can be divded in two main layers: the planetary boundary layer (PBL), that is the part in closest contact with Earth's surface and gaseous emissions from Earth's surface, and the free troposphere, that is above the PBL and which

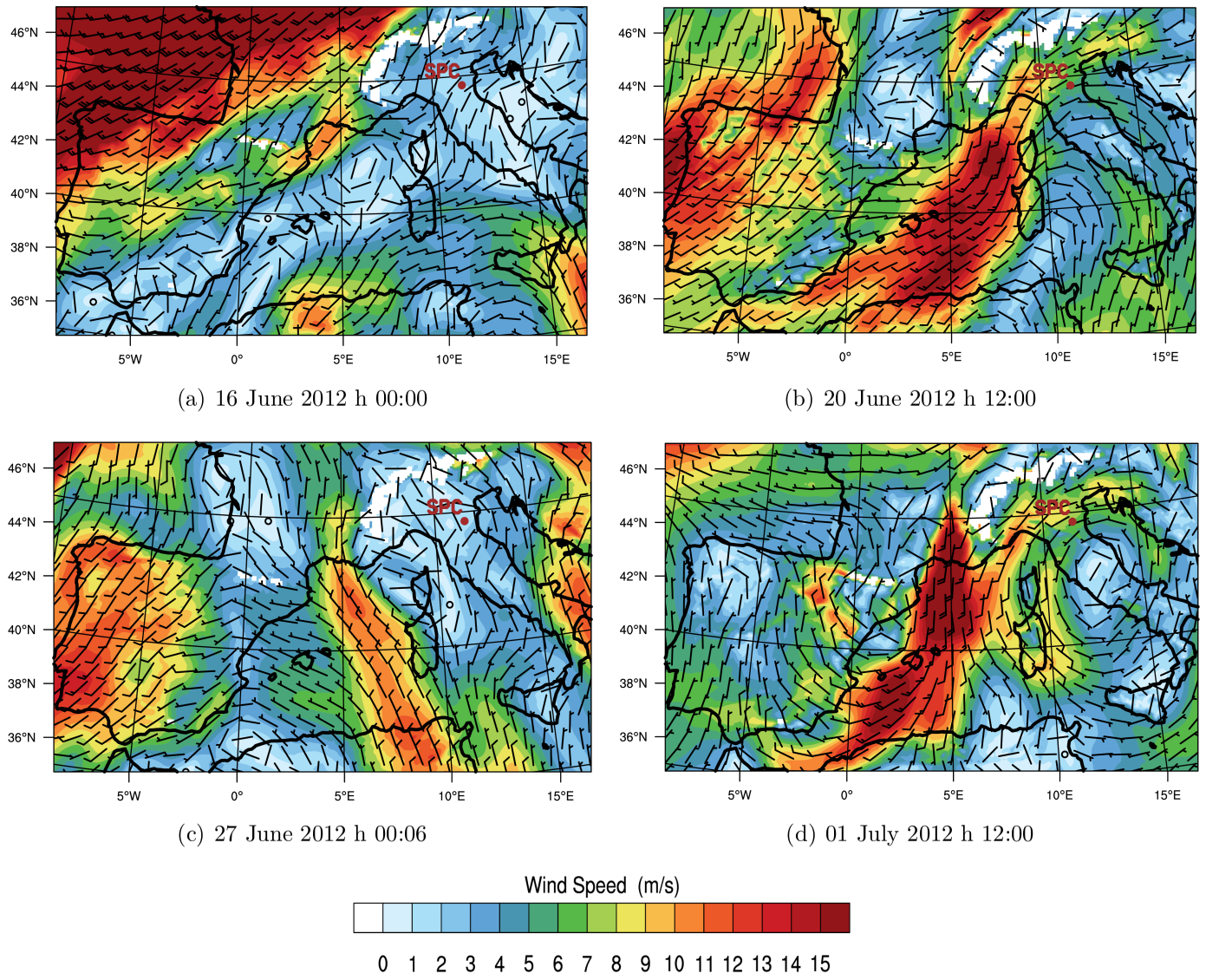

(a) 16 June 2012 h 00:00

(b) 20 June 2012 h 12:00

(c) 27 June 2012 h 00:06

(d) 01 July 2012 h 12:00

Figure 3.3: WRF wind maps at 800 hPa for four different days of the campaign, each one representative of different meteorological condition: panel (a), 16 June at 00:00: stagnation phase; panel (b), 20 June at 12:00: advection from North Africa; panel (c), 27 June at 00:06: inversion in wind direction over Po Valley; panel (d), 01 July at 12:00: second event of advection from North Africa. The red dot indicates the geographical position of the SPC station

is more decoupled, both chemically and dynamically, from surface processes. Stull (1988) [175] defined the Planetary Boundary Layer (PBL) as "the part of the troposphere that is directly influenced by the presence of the earth surface, and responds to surface forcings with a time scale of about an hour or less." The typical PBL evolution under high pressure conditions is illustrated in figure 3.4.

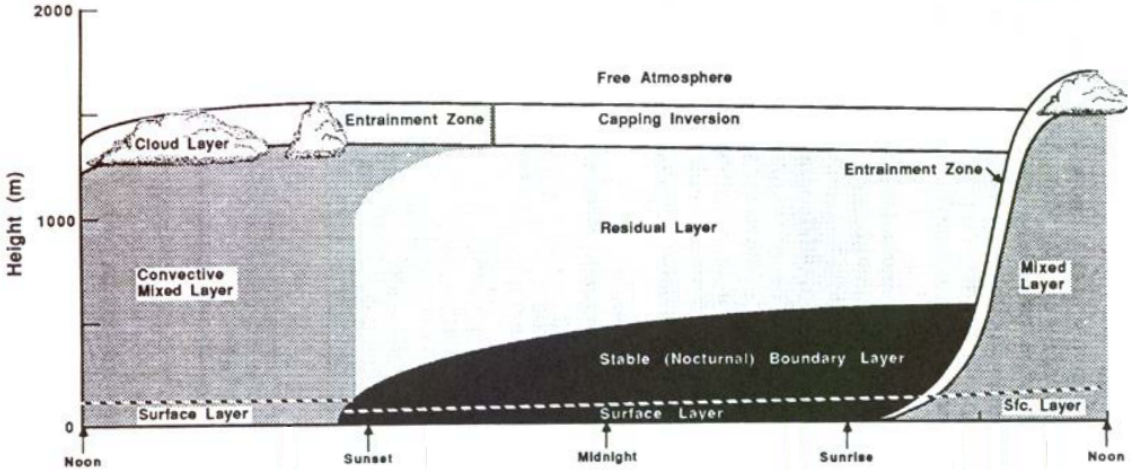

Figure 3.4: Typical diurnal evolution of the PBL over land under fair weather condition [175]

During day, and more generally during afternoon, when solar heating and convection are stronger, the PBL is at its maximum height: the solar forcing causes thermal plumes to rise, transporting moisture (that, mixing upward and cooling, will then causes cloud formation), heat and aerosols. The plumes rise and expand adiabatically until the top of the PBL where the thermodynamic equilibrium is reached. Inside this layer air is subject to rapid mixing (*Mixed Layer*, ML), causing potential temperature and humidity, as well as concentrations of aerosols and long-life chemicals, to be nearly constant with height. Near sunset the convection begins to decrease and mixing in the ML ceases. The surface cools by radiation and a shallow stable layer (called *stable nocturnal boundary layer*, SBL) forms and becomes decoupled from the layer above (called *residual layer*, RL). During this PBL phase, the air mixing volume is smaller than during daytime. For a pollutant that is emitted at a constant daily rate into a stagnant airmass, that means that its concentration near the surface will be higher respect to a well developed mixed layer condition. Generally the pollutants emitted during the night remains trapped into the SBL whereas the pollutants of the previous days tend to stay in the RL. After sunrise, solar heating triggers convection again and air from the stable bounday layer is uplifted and eventually mixed up with the residual layer air. A stable layer (potential temperature increasing with height) forms at the top of the boundary layer and it is called *capping inversion* layer. This inversion traps surface-induced turbulence and air pollutants below it, and cut any interactions of the surface with the free troposphere. This layer, during daytime, is called *entrainment zone* as air parcels from

the convective mixed layer and free troposphere can mix there. In case of cloudy or rainy conditions, as well as in case of advective weather situations, free convections are no more primarily driven by solar heating, but by ground thermal inertia, cold air advection, forced mechanical convection or cloud top radiative cooling. In those cases the PBL development shows slower growth and lower height maxima and its evolution is generally more difficult to describe [175].

As explained above, the PBL height is a key parameter for air quality analysis, pollutants dispersion and quantification of pollutant emissions as it determines the air volume available for the dispersion of all the atmospheric constituents and regulates the pollutant concentration near the surface. The evolution of the PBL height here is estimated both from LIDAR and radiosoundings profiles. Basing on the individuation of the maximum vertical gradient of R is in fact possible to evaluate the top height of the aerosol vertical mixing and therefore follow the evolution of the ML. An example is given in figure 3.5 where the time evolution of R profiles is reported together with the PBL height estimate from LIDAR (indicated in red stars). It is possible to notice that after afternoon hours it becomes difficult to individuate a sharp gradient in R, as the suspension of aerosol in the forming RL masks the contours of the PBL descent. Similar difficulties are encountered in presence of layers of high scattering aerosol, such as during dust events, or in presence of clouds and fog. During this campaign, when such conditions are present, the PBL height from LIDAR is not evaluated.

To check the validity of this method,the PBL height from LIDAR is compared with the one obtained from radiosoundings using the bulk Richardson number (R_{b_i}) method [104]. The profile of R_{b_i} is obtained as:

$$R_{b_i}(z) = \frac{g \cdot (z - z_0)}{\theta(z)} \frac{[\theta(z) - \theta(z_0)]}{u(z)^2 + v(z)^2} \tag{3.1}$$

where θ is the potential temperature [1], g is the gravity acceleration, z is the height, z_0 is the height of the surface, and u and v are the zonal and meridian wind components. The PBL top is then defined by the height at which R_{b_i} is greater than the critical bulk Richardson number $R_{b_{ic}}$, taken to be $R_{b_{ic}}$=0.21 [190]. Above this threshold air is considered to be decoupled from the PBL. From figure 3.6 is possible to notice that, when both methods are applicable, the resulting PBL height estimate is in very good agreement. Overall the the results shows that the top of PBL is under 1500m during the meteorological phase 1, with the exception of the 19th June, when it reaches 2000m. From 21th June to 27th June PBL maximum height is maintained around

[1] The temperature that an unsaturated parcel of dry air would have if brought adiabatically and reversibly from its initial state to a standard pressure, p_0, typically 1000 hPa. Its mathematical expression is $\theta = T \cdot \frac{p_0}{p}^k$ where θ is the potential temperature, T is temperature, and $k = R/c_p$. R is the gas constant of air, and c_p is the specific heat capacity at a constant pressure. For air k= 0.286

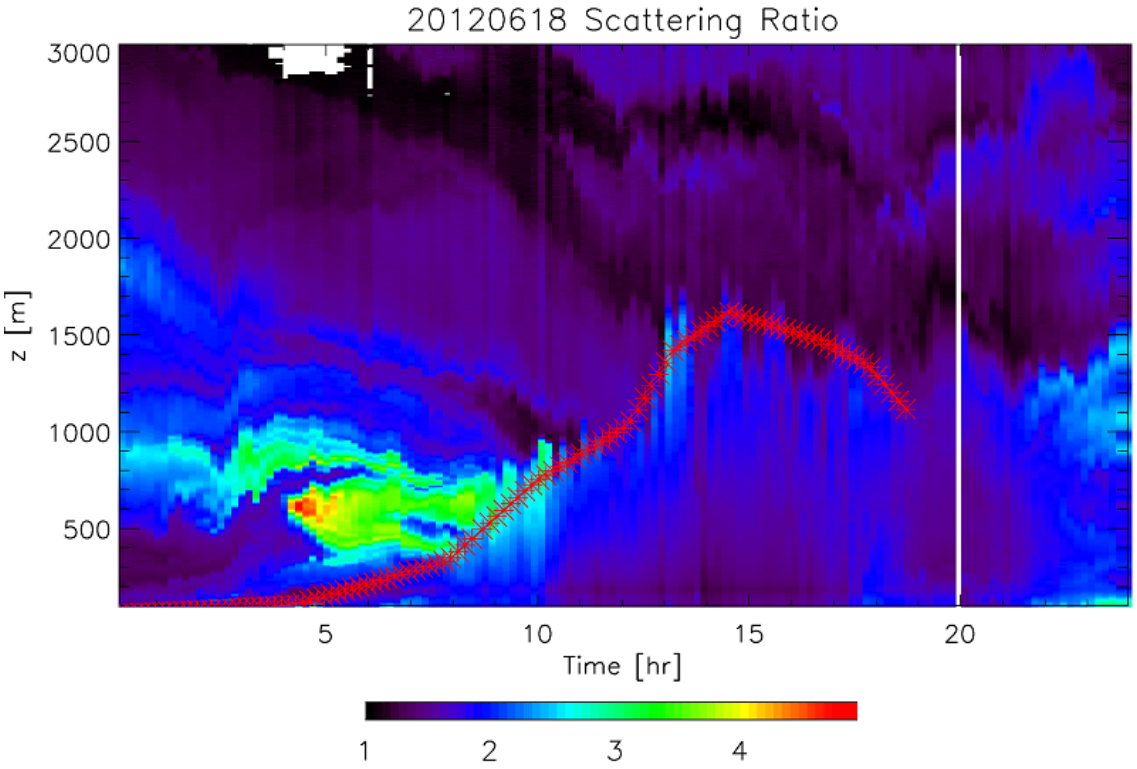

Figure 3.5: Example of LIDAR PBL height extimation based on the vertical gradient of R. Figure reports the R values for the 18th June. Red stars indicate the PBL height estimate

1900m, with a single peak of more than 2200m reached the 24th June and a minimum of 1700m shown the 26th June. During the following days it was not possible to retrieve the maximum PBL height because of the presence of high scattering aerosol layes (see figure 2.8 of section 2.2.3), until 3rd and 4th July, when PBL reached again maxima higher than 2000m. As explained above, the aerosol vertical distribution

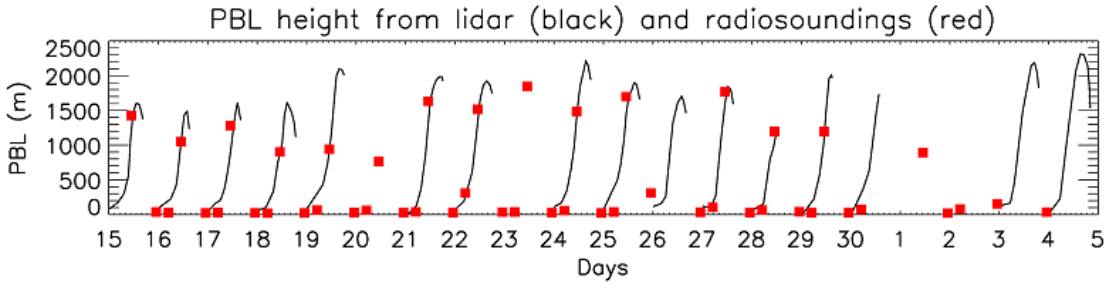

Figure 3.6: Diurnal evolution of the PBL over SPC inferred by lidar (black line) and radiosoundings by means of the bulk Richardson number (red squares)

is strongly affected by the PBL cycle. The following sections will show such effect on the Po Valley vertical aerosols distribution. It is important moreover to notice that the PBL can be also considered as a reservoir of pollution inside the basin. As the Po Valley is surrounded by mountains, pollutants usually remain confined over the region by this geographical barrier. However, when the PBL reaches height

comparable to the mountain peaks, pollution can be uplifted over the mountain heights and, under advection conditions, being transported toward more remote areas. This will be investigated in particular during the days of North-Easterly winds (22th June - 29th June, phase 3), when the concomitance of deep convective PBL may favour the export of Po Valley pollutants through uplift and subsequent advection over the Appennines ridges toward the Tyrrenian Sea. Figure 3.7 shows, for this range of days, the PBL top temporal evolution (between 06:00 to 15:00 UTC) along a vertical section between MTC and SPC (as shown in left panel). Solid lines reports the PBL top simulated by the WRF model, compared to the values (also averaged on the 22th - 29th June period) estimated from LIDAR over SPC (reported in squares). The WRF PBL top level appears to be underestimated respect to the LIDAR retrieved values. Both diagnostics indicate anyway that convection reaches a level from which uplifted pollution can overcome orography (red solid line). During days of phase 3 it is possible then to expect an export of air pollutants from Po Valley toward the North-Western part of the Mediterranean Basin. Such events will be investigated in detail in chapter 4.

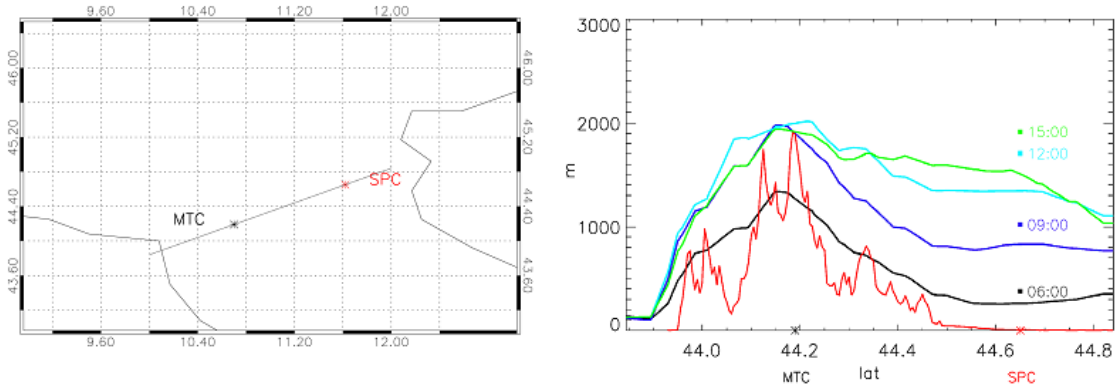

Figure 3.7: PBL vertical section between SPC and MTC. Left panel shows the geographical segment along which the vertical section was investigated. Right panel reports the PBL height (averaged over the period 22th-29th June) from WRF (solid lines) and LIDAR (squares). Different colors indicates different hours of the days. The red line indicates the real orography (taken from a geographical elevation dataset $http : //research.jisao.washington.edu/data_sets/elevation/$). SPC and MTC stations are also indicated respectively by a red and a black star

3.2 Aerosol regimes

3.2.1 Comparison between ground based in-situ measurements and LIDAR

A better understanding on the vertical evolution of aerosol properties was investigated integrating the optical information from the LIDAR profiles with the size

ground measures of the APS in SPC (near sea level, 11 m a.s.l) and of the OPC at MTC (2100 m). As explained above, below 800m the LIDAR signal is just partially retrieved. The consequent increasing uncertainties with decreasing height make the LIDAR profile not reliable under 100m. To evaluate if LIDAR retrieved profiles at this height can be anyway considered representative of ground conditions, and therefore can be significantly coupled with ground in-situ measurements, a comparison of the aerosol extinction at 532 nm near the ground (∼100m) and the APS particle counts is performed. Lidar aerosol extinction (which is integrated over the whole particle size distribution) at 532 nm tend to be dominated by the contribution of particles which size range is close to the range of the lidar wavelength (532 nm). Therefore aerosol extinction and concentration around this size range should be nearly proportional. For semplicity here it is shown the concentration of particles at 523 nm of diameter (Dp) only. Figure 3.8, that shows the comparison for the whole campaign period (15 June 2012 to 5 July 2012), indicates indeed a very good agreement in the temporal evolution of the two datasets. Both instruments captures the daily increase in particles at the ground, as well as single peaks events. The overall correlation along the whole campaign is 44%. This suggests a well mixed state and a similar aerosol distribution at ground and at 100m. During the analyzed period therefore the lower levels of lidar retrieved information can be considered reasonably representative of aerosol ground conditions.

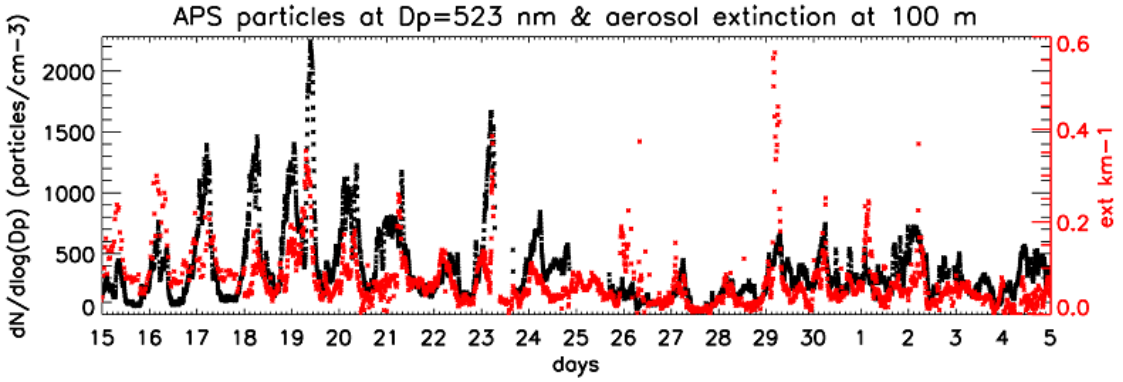

Figure 3.8: Lidar extinction (in Km-1) near ground (∼100, red line) and particles concentration (in dN/dLog(Dp) with Dp=523nm from the APS (black line)

3.2.2 Aerosol size distributions

The time evolution of the aerosol size distribution at SPC and MTC is reported in figure 3.9. First panel shows the time series of the aerosol Volume distribution per cm3 observed by the APS at SPC. Colours report the volume of particles per cm3 of air having diameters between $Log(Dp)$ e $Log(Dp) + dLog(Dp)$ while the y-axis indicates the diameters Dp of the particles in μm. The aerosol volume distribution

is expressed in $\mu m3/cm3$ and is estimated as[165]:

$$Vn(Log(Dp)) = \frac{\pi}{6} Dp^3 \cdot \frac{dN}{dLog(Dp)} \cdot dLog(Dp) \tag{3.2}$$

To provide, accordingly to Van Dingenen et al. (2004)[187], a clear indication about the eventual presence of mineral dust layer in free troposphere, lower panel of figure 3.9 shows the timeseries of coarse (diameter > 5 um) aerosol concentration observed at MTC. The evolution of the observed size distribution during the different aerosol

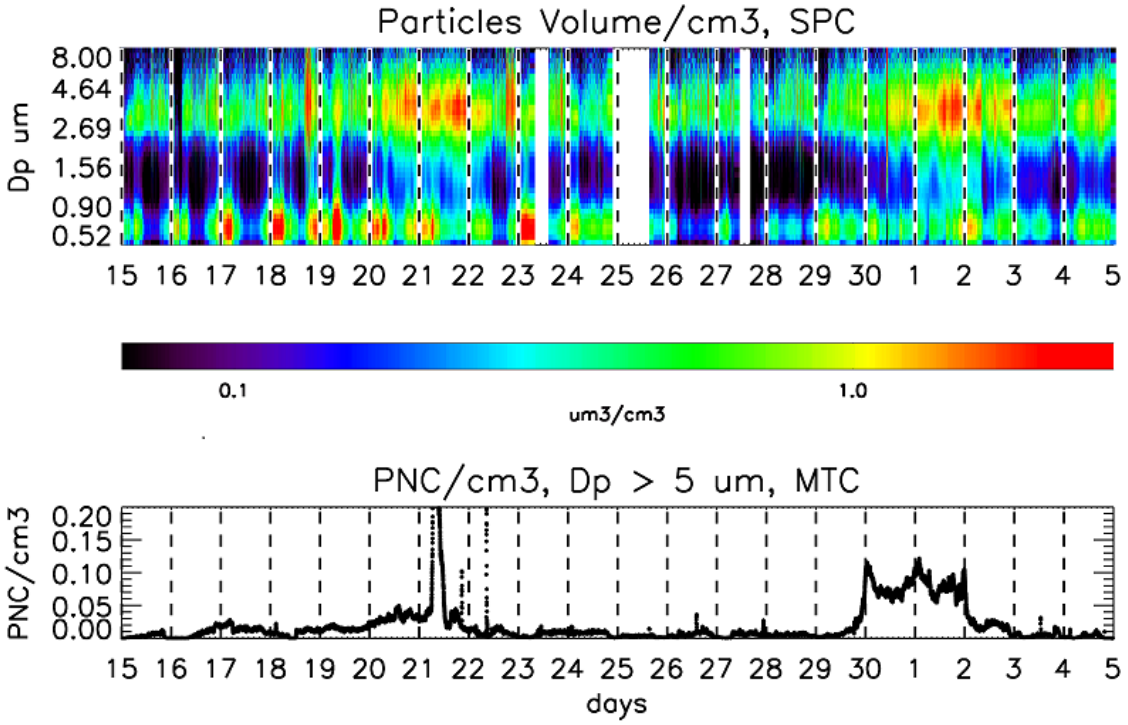

Figure 3.9: Size distributions at SPC and MTC. First panel: Aerosol Volume distribution observed by the APS at SPC. Colours indicate the volume of particles per cm3 as a function of the diameter Dp (in μm). Second panel: Particle Number Concentration (PNC) per cm3 of coarse (Dp>5μm) particles at MTC

phases is presented in the following section, along with LIDAR data analysis and trajectory study.

3.2.3 Aerosol during summer stagnant conditions

The meteorological analysis showed that the 15th June-19th June days (phase 1) where characterized by low winds (< 4m/s), low PBL heights (lower than 1500m) and increasing temperatures, with a behaviour typical of the Po Valley polluted summer conditions [153]. This phase is characterized by a marked daily aerosol cycle and a progressive accumulation of particles. This can be seen in the increase on the lidar extinction near ground (from 0.2 km-1 to 0.3 km-1) and on the in-situ number concentration (from 500 particles/cm3 to nearly 1500 particles/cm3) of

small particles ($Dp \sim 523nm$) visible in figure 3.8 during the early-morning hours (0-6 UTC, condition of stable nocturnal boundary layer). During this phase, lidar classification of figure 2.8 shows a constant background layer of spherical particles up to 2 km height, attributable to aerosol from anthropogenic pollution and modulated on the vertical by the PBL daily cycle. From figure 3.9 is possible to notice a bimodal aerosol distribution over SPC, the first mode for particles of diameter $0.5\mu m < Dp < 1\mu m$ and the second for $2\mu m < Dp < 5\mu m$ visibile during the whole campaign but more clearly marked during these days. The first mode shows the accumulation of particles with an increasing aerosol volume during the early hours of morning, growing from 0.8 $\mu m/cm3$ to 2.5 $\mu m/cm3$. No strong variation are noticed in the second mode. The OPC in MTC shows a Particle Number Concentration (PNC) less than 0.02 PNC/cm3.

3.2.4 Saharan dust transport

From 20th to 21th June 2012 and between 30th June and 2nd July, strong south-westerly winds, associated with a stable anticyclonic circulation, are observed above 2000 m height. Such synoptic condition can lead to events of dust advection from Sahara across the Basin. Over the Mediterranean area desert dust is found to be usually transported between 2 and 5 km of altitude (lower free troposphere) [125, 79] with a most intense aerosol load around 3 km [79]. Nevertheless there is evidence of episodes of mixing with local pollution near the ground [14, 62, 130] that can modify the local aerosol optical properties and increase the local PM concentration with an annual mean contribution that, in North Italy, is estimated to be 10 $\mu g/m3$ [128]. Such studies relied on in situ measurements, while a direct evidence of dust entrainment in the PBL, like can be offered from continuous observations of the vertical aerosol distributions, was missing. The use of a combination of the LIDAR profiles with the APS-OPC measurements and the FLEXPART model helped to describe both the dust events in free troposphere and its mixing inside the PBL. The first event (beginning the 19th June) can be observed between 2000 and 5000 m in figure 2.8 as a coherent layer of depolarizing aerosol (type 2, see section 2.2.3). The layer is clearly visible above 2000m, and until 21th June, as an enhancement in R profiles (1-1/R parameter up to 0.8) while, below that height, is not possible to discern the layer signal from the background value. The enhancement in R is accompanied with increased aerosol depolarization ($\delta_a \sim 10\% - 15\%$ during the whole event, with values higher than 20% reached the 20th June above 3000m). Intermediate polarization (aerosol type 3) is observed below the depolarizing layer, throughout the dust event, and persisting until June 22th-23th. As mentioned above, this class can be representative of dust mixed with local spherical particles. Such hypothesis is confirmed, for the 20th and 21th June, by a simultaneous enhancement of large particles observed both at the ground height, by the APS of SPC (first panel

figure 3.9), and at 2100 m height, by the OPC of MTC (second panel, figure (3.9). The APS shows an enrichment in the 2-7 μm particles Volume contribution up to 2.5 $\mu m3/cm3$ while the OPC detects an increase of coarse particles concentration up to 0.050 cm-3. The peak in coarse particles seen the 21 June at around 09:00 UTC (up to 0.360 cm-3) it is likely ascribable to a stronger aerosol load. This can be both caused by more intense dust episode within the main event, or by a possible enrichment of the dust particles on other pollutants captured during the transport from North Africa, as similarly shown in MTC observations in 2008 by Cristofanelli et al. (2009)[37]

The second events (beginning in the late hours of 28th June) is characterized by a second layer of enhanced R (1-1/R around 0.6) from 28th June at 23:00 UTC to July 3 at 0 UTC, Depolarization reaches values higher than in the previous event (with mean values of 15% and maximum exceeding 20%); this is clearly visible as a thick and persistent layer of depolarizing aerosol (type 2) that extends down and reaches the ground on July 1st. As in the previous case, close to the depolarizing layer it is possible to observe the presence of intermediate depolarization particles (type 2). Again, in-situ observations (figure 3.9) show an increase in coarse particles volume in correspondence of particles detection of type 2 and 3 close to the ground, with values slightly superior to the previous event and an increased contribution of 1μm-2μm diameter. MTC measures concentration nearly double the values of the 20th June, with mean values of 0.08 cm-3 and peaks of 0.10 cm-3.

3.2.4.1 Backward trajectories analysis: FLEXPART

FLEXPART analysis (Figure 3.10, upper panels) shows that the backplume for both the events originates from dust emissive regions (North Africa). Backtrajectories were released over a 0.1°x0.1°x1000m box centered over SPC at 3000m, height at which there is supposed to have the maximum advection. The transport for the first event (20th June at 12 UTC) appears to be more direct, with an average transport time of 2 days, respect to the 29th June event that originates from western Sahara and has a longer pathway around the anticyclonic circulation (around 4 days). Aerosol Optical depth from multimodel forecasts (SDS-WAS Sand and Dust Storm WMO warning advisory and assessment system http://sds-was.aemet.es/forecast-products/dust-forecasts/compared-dust-forecasts) have a spatial distribution in agreement with FLEXPART footprint for the two events. The coupling of FLEXPART footprint with DREAM emissions (figure 3.10, lower panel) allows to provide a quantitative time evolution of the dust concentration on the SPC site. To assess the impact of Saharan dust transport on aerosol concentration over North Italy, backward plumes were coupled with dust emissions from Africa taken from the Dust Regional Atmospheric Model (DREAM) inventory[2] [132], [133], [8] at 0.2°×0.2°

[2]http://www.bsc.es/earth-sciences/mineral-dust-forecast-system/bsc-dream8b-forecast

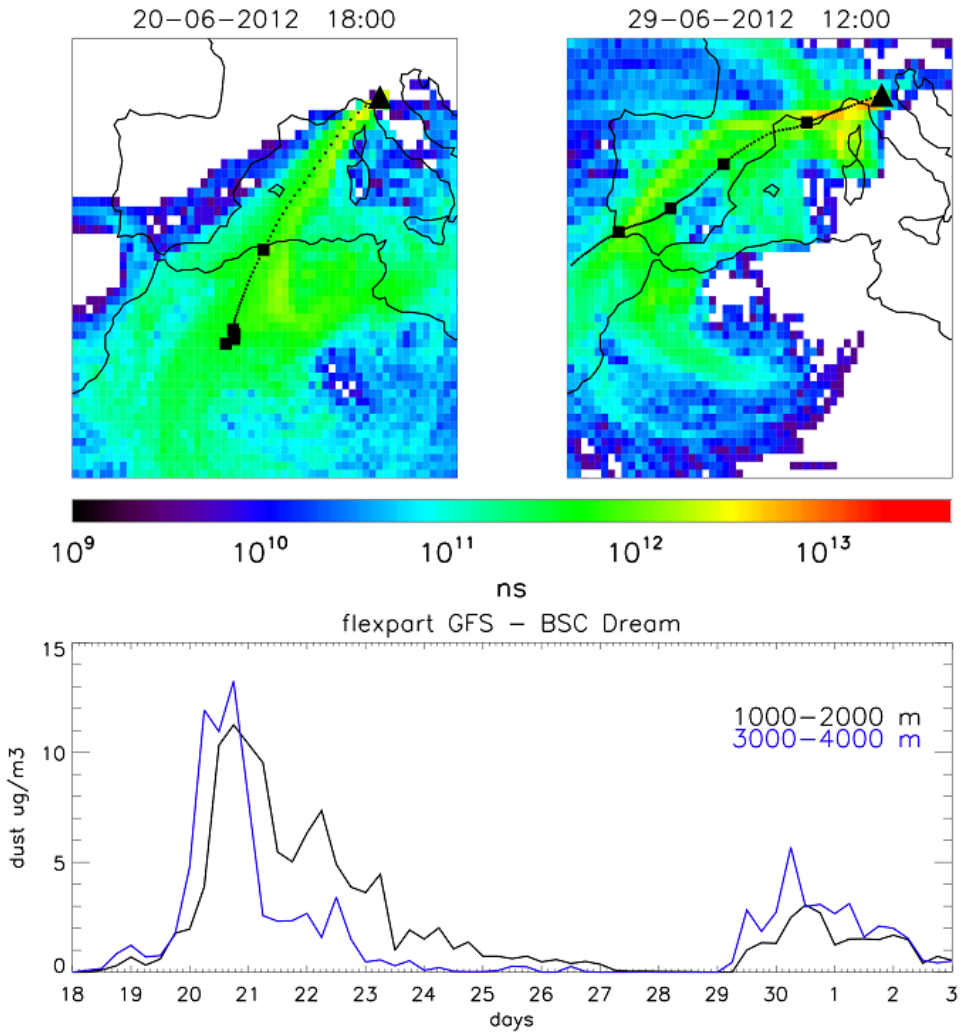

Figure 3.10: FLEXPART backtrajectories over GFS meteorological input: Upper panels show the footprint (in ns of residence over each bin) of the trajectories released over SPC at 3000m. Black triangle indicates the point of release, black squares mark the position of the center of mass each 24 hours. The pattern of trajectories released the 20th June at 18:00 UTC are shown on the left, while pattern released the 29th June at 12:00 UTC on the right. The simulated dust concentration over the SPC site, derived by the coupling with DREAM, is reported in the lower panel each 6 hours. Black line is relative to the particles released at the 1000m-2000m atmospheric layer and blue line to the 3000m-4000m one

resolution. Dust aerosol were considered to be injected uniformly below 1000 m above ground level. The convolution of the time of residence (given in nanoseconds of particles residence time over each geographical grid point) with dust emissions (given in kg/m2/h), integrated over the geographical domain, gives an estimate of the total mass of dust advected over SPC for each release. The upper panels of figure 3.10 shows the footprints of the retro-plumes released the 20th June at 18:00 UTC (left panel) and the 29th June 12:00 UTC (right panel). The footprint reports the total time of residence[3] of particles in each geographical bin, representing the sensitivity of the relase site to the emissive regions reached by the retroplume. The position of the center of mass of the cluster is indicated by black dots, with release point marked by a black triangle and position each 24h highlighted by black squares. The simulated dust concentration over the SPC site, derived by the coupling with DREAM, is reported in the lower panel for the period of interest with a time-steps of 6 hours. Black line is relative to the 1000m-2000m atmospheric layer and blue line to the 3000m-4000m one.

The simulation shows, in correspondence to lidar observations, the presence of two events with a progressive descent from the 3000-4000 m height layer to the 1000-2000 m height. The maximum mineral aerosol load, both at the upper layer (12-13 μmg/m3) and at the 1000m-2000m layer (11 μmg/m3), is reached on 20th June. These concentrations lie in the range of past observations in the Northern Mediterranean area (estimated to be around 10 μmg/m3 during June-July months [138]). According to FLEXPART, the import of dust persists until the morning of 23th June, 12 hours later than what the APS and lidar observations suggests. The second dust event has a correct timing with respect to observations with lower dust concentrations. The dust load is underestimated for this event with concentration between 3 and 5 μmg/m3 while the APS and the OPC indicate a dust burden similar (or even higher) to the first observed event. A quantitative assessment of the dust transport appears therefore to be difficult, with uncertainties possibly arising from the intrinsic limitations of the evaluation method (fixed height for PBL over desert, uncertainties on the emission estimate, uncertainties linked to trajectories simulation [173]). Nevertheless the model offers a robust characterization of the dynamics and a correct timing of the events.

3.2.5 Daily vertical distribution of depolarizing and non depolarizing aerosol

Despite the synoptic variability observed during the period, it is possible to derive a mean diurnal evolution of the aerosol type, classified based on their observed optical parameters (described in section 2.2.3). Figure 3.11 reports the frequency of

[3]evaluated as the fraction of the total particles mass on each bin, weighted by the timestep of simulation (1 hour)

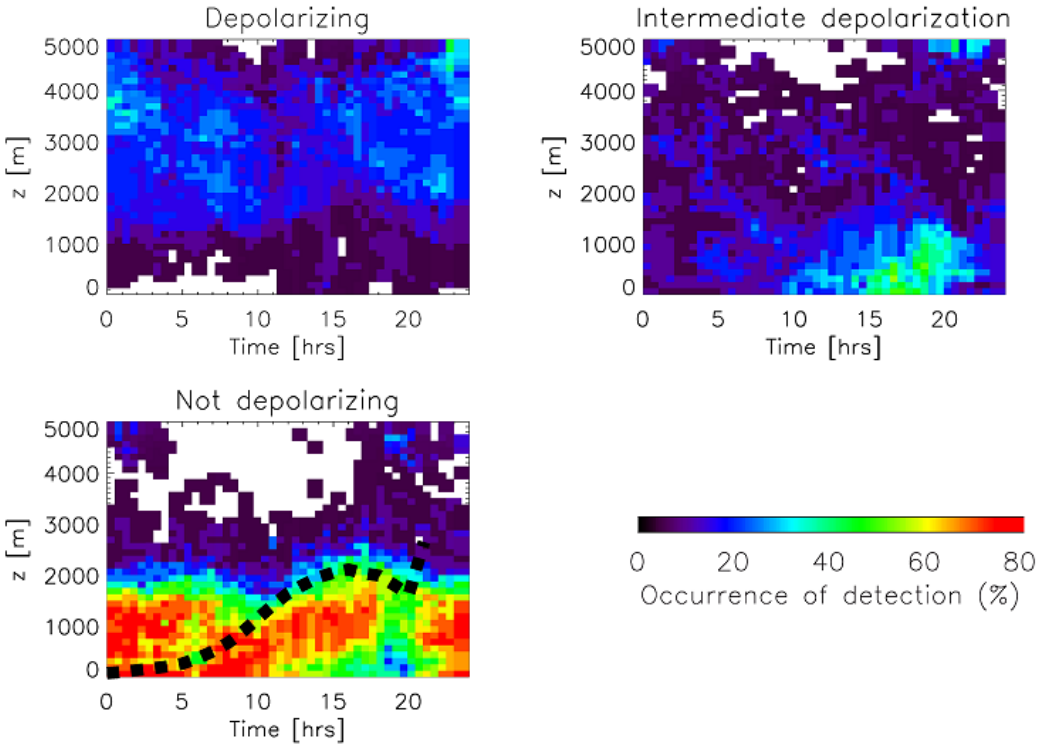

Figure 3.11: Mean diurnal frequency of the vertical distribution of each aerosol class: Depolarizing (Upper left), Intermediate Depolarizing (Upper right) and Non Depolarizing (Lower left). The mean PBL height, derived from LIDAR analysis, is reported in black dashed line over the non depolarizing distribution.

occurrence for each of the three classes for the period 15th June – 5th July. Each panel of figure 3.11 reports the ratio between the number of aerosol class detections and the number of days of measurements.

Depolarizing aerosol (upper left panel), that was demonstrated to be associated to desert dust, is mostly observed between 1500 and 5000 m height with a frequency of occurrence ranging between 15 and 30 %. Non negligible occurrences ($\sim$ 10%) are also observed close to the ground in connection to the dust descent of the second event.

Spherical aerosol (lower panel) clearly shows the signature of the PBL evolution with a constant occurrence (up to 80 %) in the residual layer between 0 and 5 UTC around 1000 m height. The mean daily PBL uplift (derived by lidar data and highlighted by black dots) is marked by frequent observations of spherical aerosol between 6 and 12 UTC, with the layer of maximum occurrence rising from the 0-1000 m to 2000 m height. Both the features indicate that, during the period of interest, the PBL starts to develop at 06:00 UTC and reaches its maximum vertical extension up to 2 km height between 17:00 and 18:00 UTC. The residual layer, visible in the evolution of spherical particles, but not determinable by lidar for the lack of sharp gradient in the observed signal, starts to develop around 20:00 from ground up to 1800m and persists until 05:00 UTC.

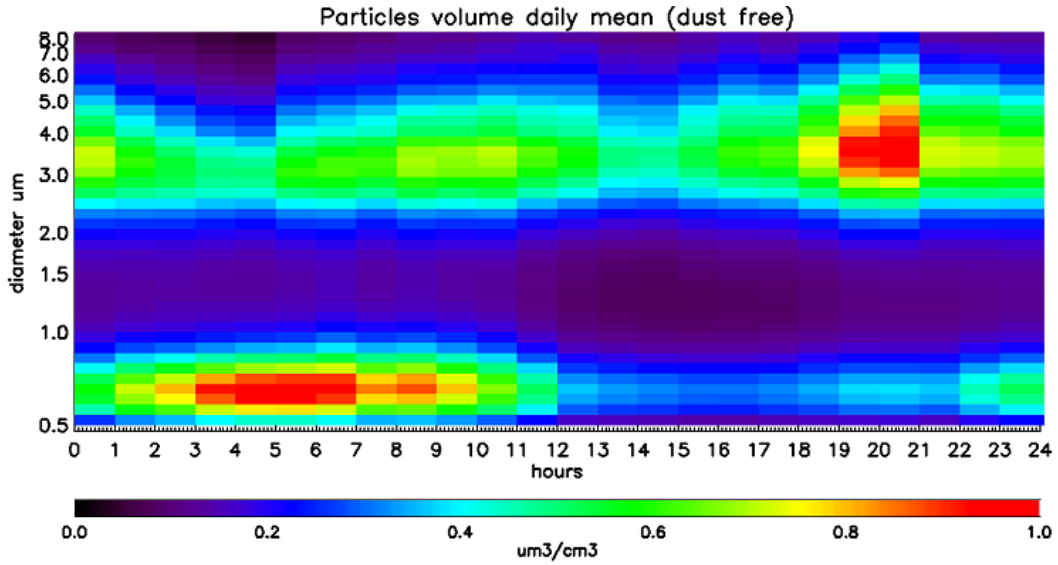

Figure 3.12: Mean diurnal evolution of aerosol volume distribution in dust-free days from the APS in SPC.

Non-depolarizing aerosols are still predominant at night-time after 21 UTC inside the residual layer. The minimum in occurrence observed in the afternoon between 16 and 19 UTC is correlated to the maxima in occurrence of the intermediate depolarization type (upper right panel), also visible in correspondence of several dust free days (see figure 2.8). Depolarization increase is observed mainly under 1000 m between 16:00 and 20:00.

Observations of particles with intermediate depolarization, not directly linked to the dust plumes, occur frequently during the campaign (13 days over 21), excluding 20th-22th June and 30th June-2nd July when the presence of dust makes difficult to identify this feature. These events are usually observed during afternoon-evening hours below 2 km (as also shown on the average in figure 3.11) associated to North-Westerly light winds at the ground. An increase in the ground coarse aerosol volume is simultaneously observed by the APS (figure 3.12). The image shows the daily mean of the Volume contribution of particles as a function of their size. From this figure the separation between the fine particles (Dp <1 μm) and the large particles (2.5 μm $<$Dp <6 μm) appears clearly. Fine particles show a semidiurnal cycle, (corresponding to the diurnal cycle of not depolarizing aerosol near the ground) with concentration increasing during the Stable Nocturnal Layer phase (late night - early morning) and strongly decreasing during the stages of well developed Mixing Layer. On the contrary, the larger particles mode shows two maxima during the day: a first one (showing volumes not superior to 0.8 $\mu m/cm3$) in correspondence of the uplift of the PBL layer and a second one, stronger, that follows the behaviour of the Intermediate Depolarization class, with values that start to increase at 15:00 UTC and reaches the maximum (1 $\mu m/cm3$) at 20 UTC. This class of aerosol deserves a more detailed analysis and it will be discussed in Section 3.2.6

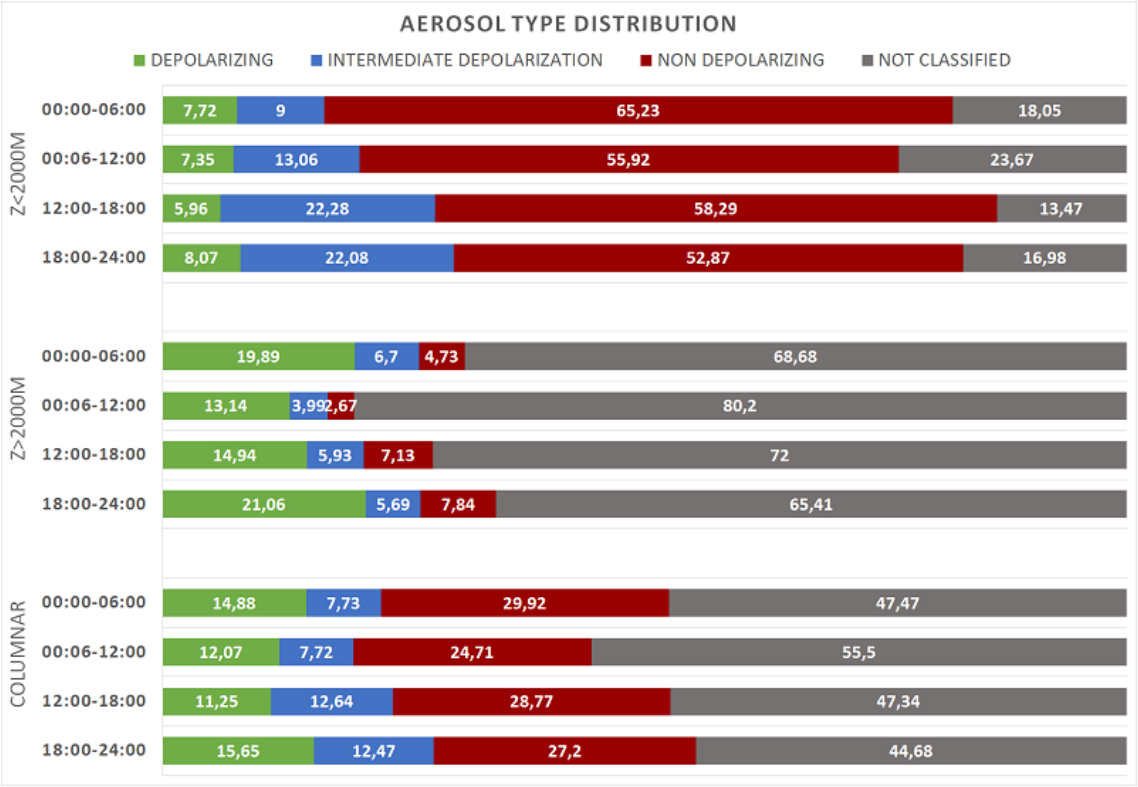

Figure 3.13: Mean diurnal frequency of distribution for the three aerosol classes (Depolarizing-Green; Intermediate depolarization-Blue; Non depolarizing-Dark Red and samples non classified as aerosol in Grey), below 2000m (panel A), above 2000m (panel B) and for the whole atmospheric column 0-5000m (panel C), integrated over the four synoptic intervals (00:00-00:06, 06:00-12:00, 12:00-18:00, 18:00-24:00)

The mean diurnal evolution of the different classes are summarized in figure 3.13: each column reports the frequency of occurrence of each aerosol classes below 2000m (panel A), above 2000m (panel B) and for the whole atmospheric column 0-5000m (panel C), and for the four synoptic intervals: 00:00-00:06, 06:00-12:00, 12:00-18:00, 18:00-24:00. Overall aerosol is mainly observed below 2000m with spherical aerosol as the predominant type (between 50% and 60% of the observations thorough thw whole day). Intermediate depolarizing type shows its diurnal cycle with an increase in detection from 9% of the early hours to the 22% of afternoon and late evening. Dust is observed at ground with a non neglibigle occurrence of 7% during the campaign. Above 2000m aerosol is observed in less than 50% of the detection and is mainly associated to dust presence (from 13% to 21 % contribution).

3.2.6 Non desert dust depolarizing aerosol

A plume of non-dust depolarizing aerosol is shown in detail for a typical day (July 3) in figure 3.14. The plume develops vertically from 15:00 UTC to 20:00 UTC, reaching the maximum height of 1500 m in late evening. The evolution and the shape of the intermediate depolarizing layer, occurred similarly during the other days (15th June, 18th-19th June, 22th-29th June, 3rd-5th July, as can be seen both

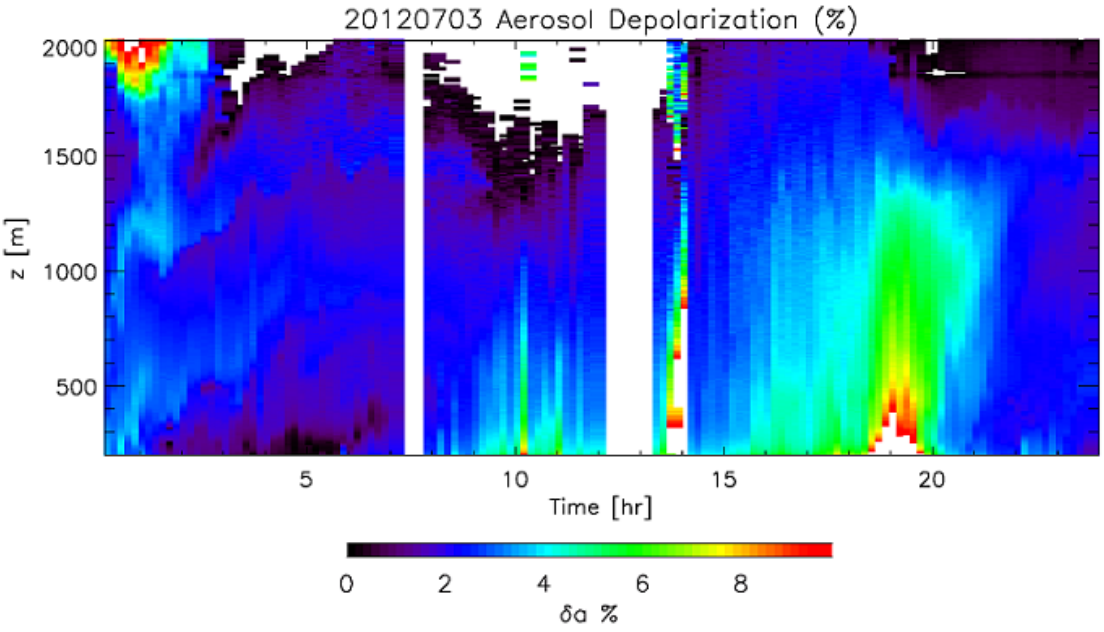

Figure 3.14: Vertical profiles of LIDAR aerosol depolarization, 3rd July 2012.

in aerosol mask and aerosol depolarization in figure 2.8), and suggests the occurrence of mineral particles inside the PBL not related to remote desert dust sources. The increase of depolarization in afternoon hours in a regime of convective PBL was already observed by Gibert et al. (2007a) [57] that demonstrated a positive correlation between depolarization ratio and vertical velocity, likely indicating an emission source of particles transported upward by convection. The actual nature of such depolarizing aerosol cannot be easily assessed. LIDAR depolarization is in fact observed in presence of irregularly shaped particles, usually soil and desert dust, but also in presence of marine aerosol [114] and ash particles [122]. Nevertheless the high-time resolution measurements of PM1 and PM10 aerosol chemical composition provided by MARGA shows no evident correlation between the depolarization increase and the presence of sea salt (not shown). Similarly, no correlation was found with black carbon, investigated by means of a multi-angle absorption photometer (MAAP) (not shown). The correlation with relative humidity was also studied to analyze the possibility of diurnal drying of particles with the consequent loss of sphericity, but that correlation was mainly found during late morning-early afternoon (between 10:00 and 16:00), therefore it does not directly impact the increase in the afternoon-evening plumes of depolarizing particles. Instead, MARGA observations reveal a maximum in calcium concentrations in PM10 at the same time of the day when depolarization and large particles APS detections increase (between 15:00 and 20:00 UTC). This can be seen in figure 3.15 where, in the upper panel, the increase in the PM10 concentration of the Calcium ion (Ca^{2+}) respect to the total PM10 ions concentration ($Ca^{2+}PM10/TotalPM10$) is shown. Lower panel of figure 3.15 reports the simultaneous increase of large particles (2.5 μm <Dp <5.5 μm) with

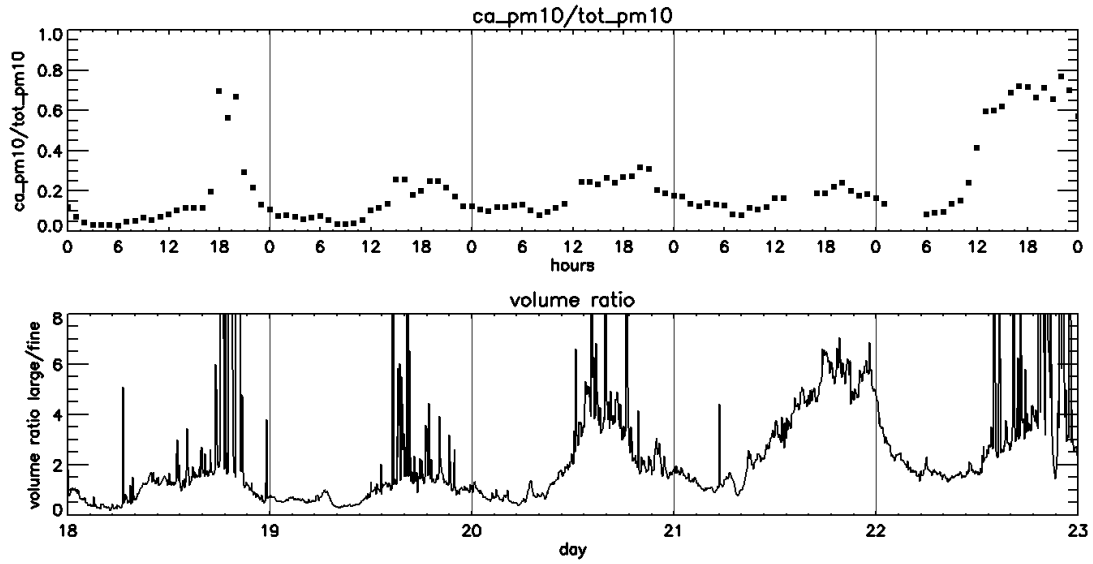

Figure 3.15: Upper panel: Increase in the Ca^{2+} PM10 ion concentration respect to the total PM10 ion concentration (from MARGA,SPC). Lower panel: Increase in large particles (2.5 μm <Dp <5.5 μm) fraction respect to the fine ones (0.5 μm <Dp <1 μm) (from APS, SPC)

respect to the fine ones (0.5 μm <Dp <1 μm). It is necessary to notice that these quantities are not directly proportional to dust burden, giving instead information on the relative contribution of Calcium particles and Large Volume particles respect to main observed aerosol background. Observations are limited between the 18th - 23th June as it is the only time interval in which continuos measurement both of Ca^{2+} and size distribution (APS) are present. Both the time series indicates a behaviour similar to the aerosol depolarization profiles, with corresponding late afternoon increases. It is worth to notice the peak in $Ca^{2+}PM10$ fraction on the 22th June (nearly 80% of all the PM10 ions), in correspondence of the strongest event of intermediate depolarizing plume (see figure 2.8). In this case the local source particles uplif can add to the resuspension of dust deposited on the ground in the previous days.

Similarly, the analysis of diurnal variation of non-desert dust aerosol at MTC, shown in figure 3.16 indicates an enhancement in the coarse particles fraction during afternoon/evening hours. Therefore, basing on these observation, is possible to hypotize that the late afteroon increase in depolarization observed at SPC can be caused by emissions and resuspension, up to free troposphere height, of soil particles from dried land sources. If so the Po Valley rural lands may act as a source of mineral particles that, under convective atmosphere conditions, can be injected into the whole PBL (as visibile in figure 3.11, right panel), with possible impact on particulate transport at regional scale.

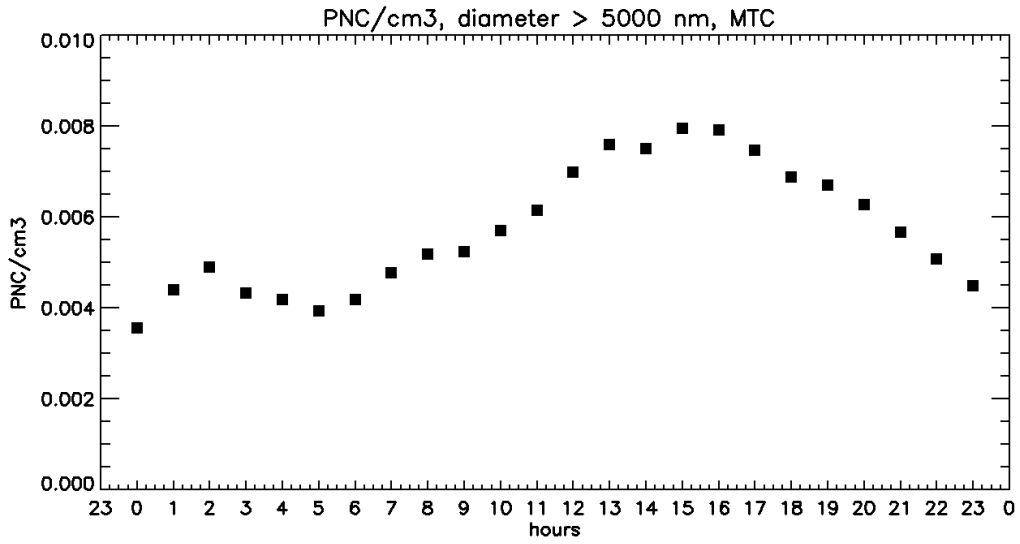

Figure 3.16: Daily mean, in dust-free days, of coarse (Dp > 5 μm) particle concentration (from OPC, MTC)

3.2.7 LIDAR evidence of aerosol hygroscopic growth

During the early hours of the day, is possible to notice, from LIDAR observations, a shallow layer of non-depolarizing aerosol below 500 m height inside a layers identified as dust and dust mixed with local pollution. This is for instance visible as a shallow layer of lower depolarizing and high scattering ratio in figure 2.8 between 00:00-06:00 of the 19th June and between 00:00-08:00 of 30th June. Decrease in depolarization is less evident in dust-free atmosphere but is nevertheless observed in several days of the campaign (19th June, 21th June, 22th June, 29th June, 30th June, 1st July, 4th July and 5th July). A detailed time-height evolution of depolarization and relative humidity, is reported in figure 3.17 for the 30th June and is representative also of the other events. Figure reports the vertical profiles of δ_a and the relative humidity from the radiosoundings at 05:00 UTC overlaid with a different color scale; the timeseries of relative humidity observed at the ground is reported as a red line. Between 1000m and 4000m, is possible to notice the dust plume (depolarization higher than 10%), associated to drier air (RH $< 50\%$). The lowermost troposphere is instead characterized by a layer with δ_a around 4% and RH between 50% and 60%. Descending below 400m is possible to notice a sharp increase in values of RH (larger than 80%) corresponding to low δ_a (less than 2%). This low depolarization near ground suggests the presence of increasingly spherical particles, which can be originated by two different processes:

- the presence of fine particles of anthropogenic origin that may deliquesce: The stagnant meteorological conditions that characterize Po Valley during anticyclonic phases are, in fact, favorable for the formation of Secondary Organic Aerosol. A recent study [73] demostrated for instance that, during summer

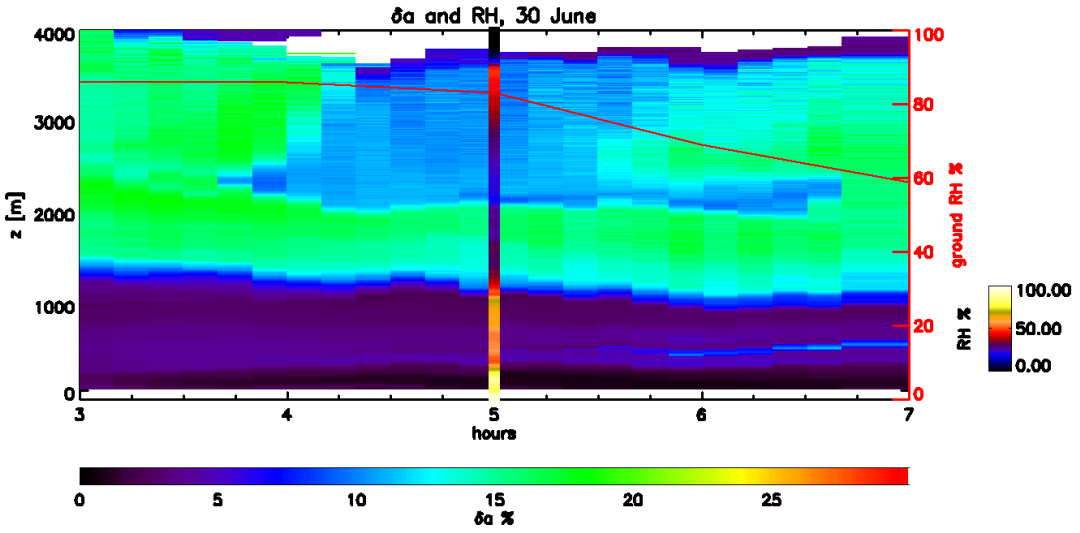

Figure 3.17: Early morining (03:00-07:00 UTC) aerosol depolarization profiles compared to vertical profiles of relative humidity from radiosounding (colored column) and relative humitidy at the ground (red line) for the 30th June

2012 campaign, the aerosol liquid water was mainly driven by locally formed nitrate.

- the condensation of water around dust particles enriched of hygroscopic components: High relative humidity conditions are deemed to cause hygroscopic growth on dust particles enhancing scattering and extinction and causing a reduction on the aerosol depolarization ratio [114, 121]. In fact, also if mineral dust is primarily an hydrophobic aerosol, it can become hydrophilic because of chemical reaction occurring on the particles surfaces during long-range transport [121, 177].

During the summer 2012 campaign, under the observed conditions, both processes can be relevant: MARGA shows in fact that nitrates in the PM1 channel (shown in figure 3.18) are increasing during the first stagnant phase with a variability similar to what shown by the APS.

This can be due to the accumulation of small particles and to the enhancement of relative humidity that favors the formation of this secondary aerosol. This is particularly marked on 19th June when two distinct peaks are observed in the same hours both in the nitrates concentration and in the APS countings. The PM10 nitrates channel of MARGA shows similar values with the PM1 channel with an increase during dust days. Dust particles can indeed transport nitrate, condensed during transport on dust surface, offering therefore a preferential condensation surface for water [166]. During the dust events this contribution may be predominant as the intensified ventilation decreases the accumulation of anthropogenic particles and, carrying dryier African air masses, makes the chance of condensation on coarser particles surface prevail over condensation on accumulation mode aerosol.

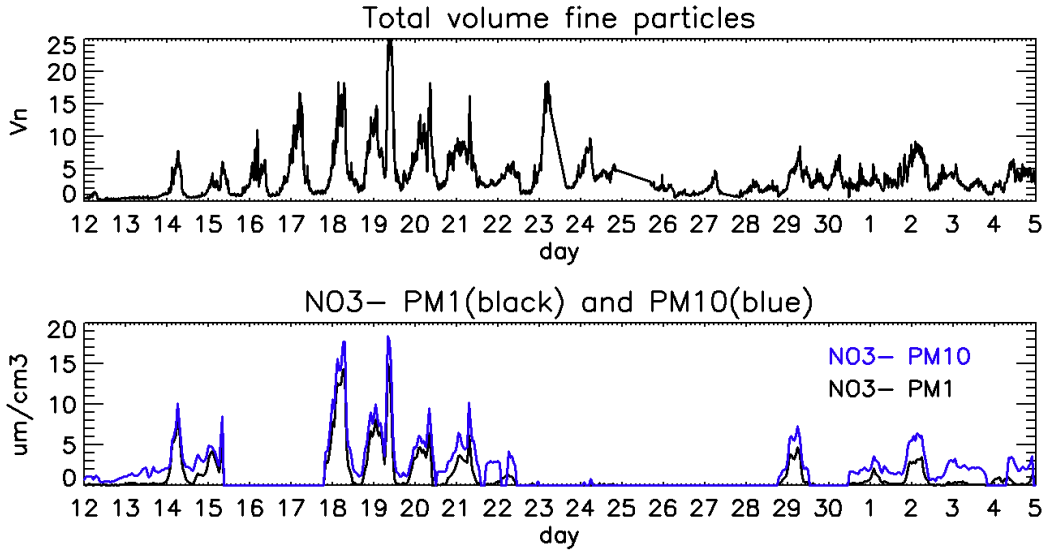

Figure 3.18: APS fine particles ($Dp < 1$ μm) volume contribution (upper panel) compared to nitrates ions concentration (NO3-) both in the PM1 (black) and PM10 (blue) channel (lower panel)

Chapter 4

Events of pollution outflow from the Po Valley

The meteorological analysis presented in section 3.1 indicated that, while during the other phases westerlies were dominants, between 22th June and 29th June (phase 3) it was possible to observe days with wind flowing prevalently from the North-East direction. This was particularly identified during 23th-24th June and 26th-28th June below 2000m. For the 23th June WRF meteorological simulations at 925 hPa pressure level (figure 4.1, left panel) show a cyclonic pattern above the Po Valley with wind intensities around 7 m/s (as also observed in SPC site, figure 3.1). Under such pattern, pollution emitted and accumulated over Po Valley can be exported over the Tyrrenean Sea. A similar condition is found for the 26th June, with stronger intensities (wind speed up to 15 m/s) and North-easterly oriented wind that can lead to a more direct transport from Po Valley towards the Gulf of Genoa. The possible extension of export events and their impact on the background levels of pollution is investigated in the following sections. For this purpose carbon monoxide (CO) is used as a tracer of pollution. The analysis is mainly based on the WRF-CHEM simulation, the trace gas aircraft measurements from the TRAQA campaign and the FLEXPART-WRF forward trajectories.

4.1 WRF-CHEM model CO concentration

WRF-Chem has been used and evaluated in past studies to assess air quality and composition over the Po-Valley regions (see for instance Tuccella et al., 2012 [185] and Carnevale et al., 2015 [25]). Nevertheless, to evaluate if the model has a correct reproduction of the background concentrations over the area of interest, and if it reproduces the vertical pollution plume development (that, as described in the previous sections, can develop up to the free troposphere and that can lead to a westward outflow in presence of favourable meteorological conditions), the simulated CO concentrations are compared to all the available CO observations. For this purpose

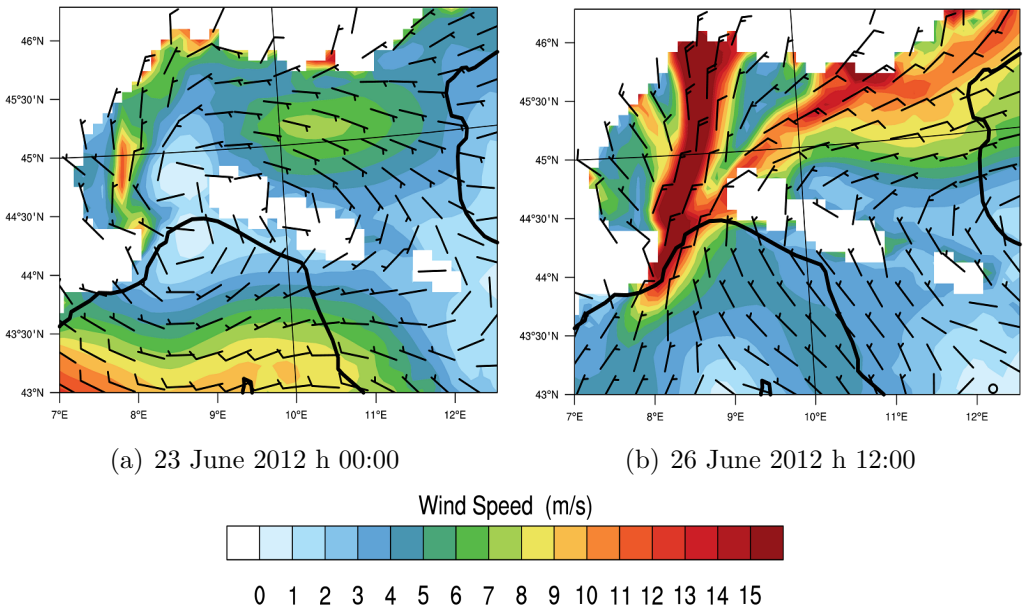

(a) 23 June 2012 h 00:00 (b) 26 June 2012 h 12:00

Figure 4.1: WRF wind maps at 925 hPa for the two possible export events of the campaign: left panel (a), 23 June at 00:00 and right panel (b) 26 June at 00:00

WRF-Chem CO is confronted with the ground level observations performed during the PEGASOS mobile lab measurements and with the MTC (2100m height) data (see figure 4.2), respectively considered representative of the CO concentration over the Po Valley ground level and at the top of the Appennines ridge. Figure 4.2, lower panel, reports the WRF-Chem CO interpolated on the mobile observations and at MTC site from 15th June to 5th July. Higher values detected by the mobile lab observations (for instance when passing close to hot spot sources like road and cities) are not reported in the plot since the model is driven by database emissions that cannot reproduce extremely intense and very localized sources. The comparison appears satisfactory along the campaign, with a good agreement in reproducing the mean concentration over the region. CO mixing ratio lies in the range of 120-180 ppbv with an average value along the campaign of 146 ppbv. The model reproduces these values with a RMSE of 29.2 ppbv, a mean bias of 11.9 ppbv and has an average value of 140 ppbv. Within these limits we can consider the WRF-Chem concentration representative of the Po Valley concentration near the ground. The reliability in the vertical transport of pollution is investigated by comparison with MTC data (figure 4.2, upper panel). The model concentrations lie in the observation range (80-140 ppbv) and reproduces the synoptic evolution (although with a less marked variability) of the campaign. The model also partially reproduces the daily cycle, instead clearly visible in the observations, that is due to the rise of PBL air from the surrounding region [36]. Such explanation is also supported by the PBL analysis shown in section 3.1.2 that indicated that, during the analysed period, the Mixing Layer reaches height comparable to the orography top during daytime.

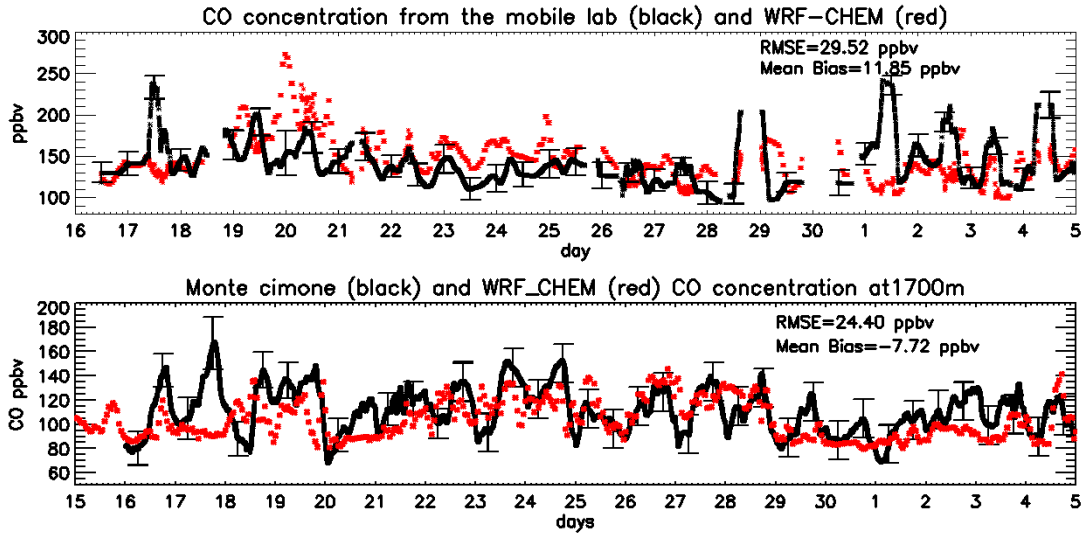

Figure 4.2: WRF-CHEM CO concentration (red) compared to the mobile lab (black, upper panel) and to the MTC (black, lower panel) measured concentration. The Root Mean Square Error (RMSE) and the mean bias between the model and the observations are also reported

4.2 TRAQA aircraft observations and WRF-CHEM simulation

Evidence of pollution outflow toward the Tyrrenian Sea are looked for in the data collected by the TRAQA aircraft. Two flights in particular investigated the area of the Gulf of Genoa during the possible export events(see also figure 2.1): flight 19 (26th June, 10:42 - 13:41 UTC) and flight 21 (27th June, 9:41 - 13:08 UTC). Instruments on board of the aircraft measured CO concentration travelling in a 3-dimensional pattern, as shown in figure 4.3.

CO observations of flight 19 (26th June) and 21 (27th June) are reported (in black) in the middle panel of figure 4.4 together with flight height (upper panel). Boxes highlight vertical dives inside the plume and are reported in figure 4.5. Measurements are also compared to the WRF-CHEM CO values interpoled along the aircrafts position both in times and position (blue) and to the CO baseline concentration (red line), evaluated as the minimum values of CO mixing ratio on the dives performed in the Gulf of Genoa during the whole campaign. Along with CO measurements, the aircraft collected ozone (O3) observations, reported in the lower panel. O3 measurements are here exploited to investigate the O3-CO correlations inside the plume. Several studies evidenced in fact that strong and positive correlation in troposphere are observed during summer when photochemistry activity is at its peak [97, 90] and O3 was producted from its precursors (including CO). Contrarily, in the winter, when pollution increase, negative correlation related to O3 destruction through NOx (NO + NO2) titration can be observed [97, 90]. Aircraft position, respect to the CO concentration as estimated by WRF-CHEM, is reported

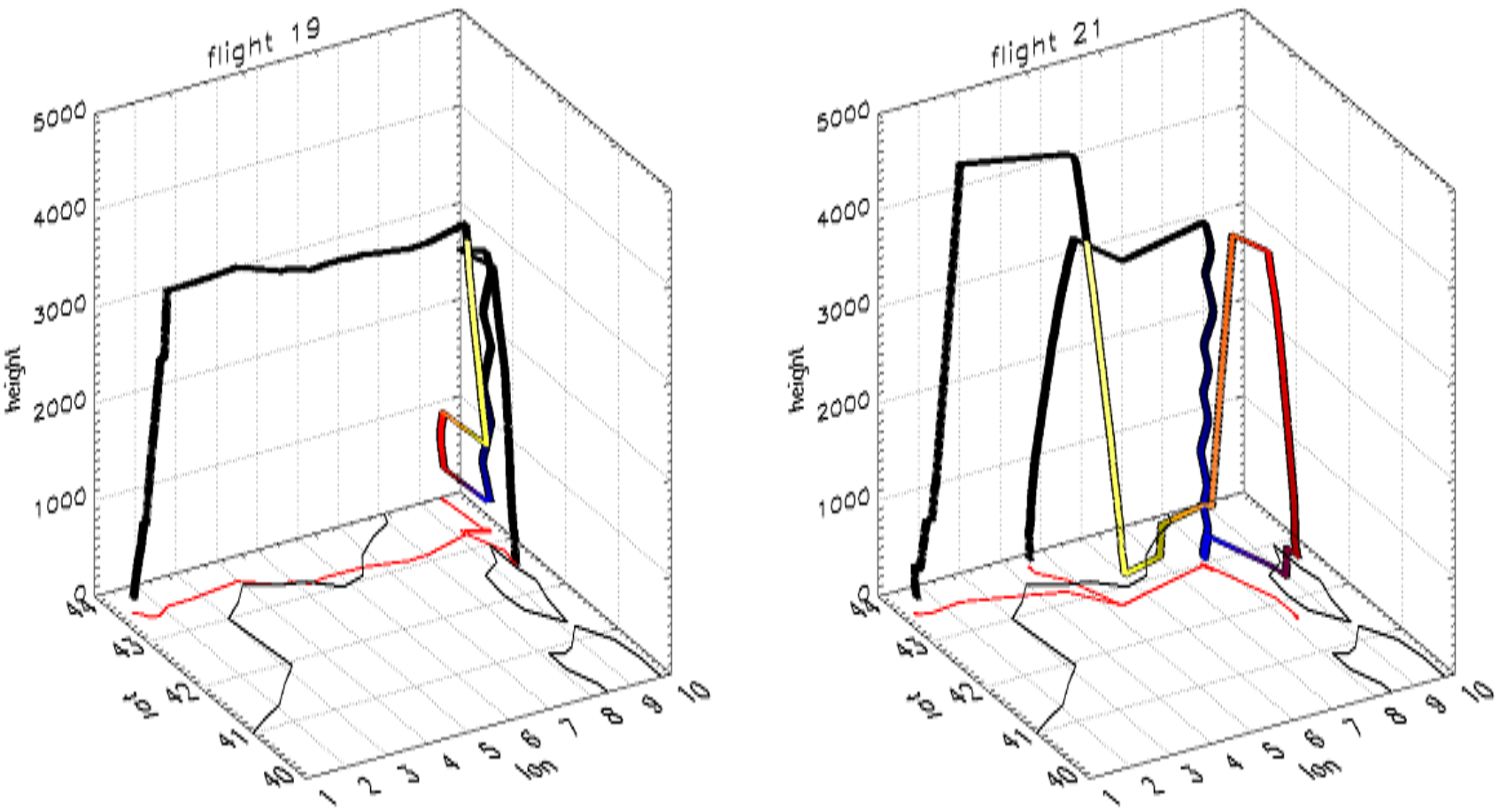

(a) Flight 19

(b) Flight 21

Figure 4.3: Three dimensional tracks of flight 19 (left panel) and fligth 21 (right panel). Red line indicates the projection of the track on the horizontal plane. Color shades refers to time intervals of interest (see figure 4.4)

in figure 4.6 using the same color code than the one used for time in figure 4.4 while the scatterplot between CO and O3 are reported, with the correspondent correlation value, in figure 4.7.

Flight 19 (26th June, left panel) shows a progressive enhancement in CO, from 90 ppbv to 120 ppbv, in the first plateau (at 500 m, from time 11.3 to 11.65). In this phase, the aircraft approached Liguria Coast from south (panel (a) in figure 4.6) entering in a CO plume as simulated by the WRF-Chem model. Enhancement in CO is also observed in the second part of the flight (panel (b) in figure 4.6) when the aircraft performed a reverse route at 900 m height (time from 11.7 to 12.1), finding an increase in concentration from 90 ppbv to 130 ppbv. Panel (a) of figure 4.5 shows the profile collected at 12:00 UTC. An enhancement in CO concentrations is observed below 2000 m height, with an increase up to 40 ppbv with respect to the baseline. It is worth to mention that also above 2000m the measurements indicates a positive anomaly of around 20 ppbv. WRF-Chem simulated CO follows a behavior coherent with observations thourough the flight though slightly overestimating concentrations in the first part. Overall the RMSE respect to flight 19 observations is 17.18 ppbv and the Mean Bias is 7.99 ppbv. O3 concentration varies between 50 and 65 ppbv. In both the plateau section of the flight (figure 4.7, left and right upper panels) O3 measurements appears to be moderately correlated to the CO mixing ratio (respectively 57% for the first plateau and 55 % for the second). As also shown in figure 4.6 the flight is crossing a region of moderate pollution and no strong photochemical evidence is found.

Flight 21 (27th June, right panel) observes a CO peak of 140 ppbv during the first dive (time 10.7) in a region close to the coast (see panel (c) in figure 4.6). Panel (b) of figure 4.5 reports the measured profile at 10:30 UTC. Conversely to the previous case, this profile shows pollution free conditions in the higher part of the dive (with a small anomaly of 20 ppbv around 3000m) with a strong increase (between 50 and 60 ppbv) below 1000 m height. Travelling southward (figure 4.4) the CO concentration decreases down to the baseline value of 90 ppbv and a similar behaviour is observed in the O3 mixing ratios reducing from 85 ppbv to 50 ppbv. Correlation between the two species in this case is strongly positive (98%, see lower left panel of figure 4.7) indicating the presence of photochemical activity. A second dive is performed in correspondence of the plume as simulated by WRF-Chem at time 11.7 (panel (d) in figure 4.6) observing again an enhancement in CO with values of 150 ppbv. Starting from this time, according to the model, the aircraft gradually left the plume travelling westward. Observed values indeed decreases, reaching at time 12.2 an area characterized by lower values of CO (90 ppbv). Correspondingly ozone concentration are increasing from 75 ppbv to 90 ppbv. Correlation in this measuring region is strongly negative (-70%, see lower right panel of figure 4.7). Such anticorrelation, being not related to ozone intrusion from troposphere (as suggested

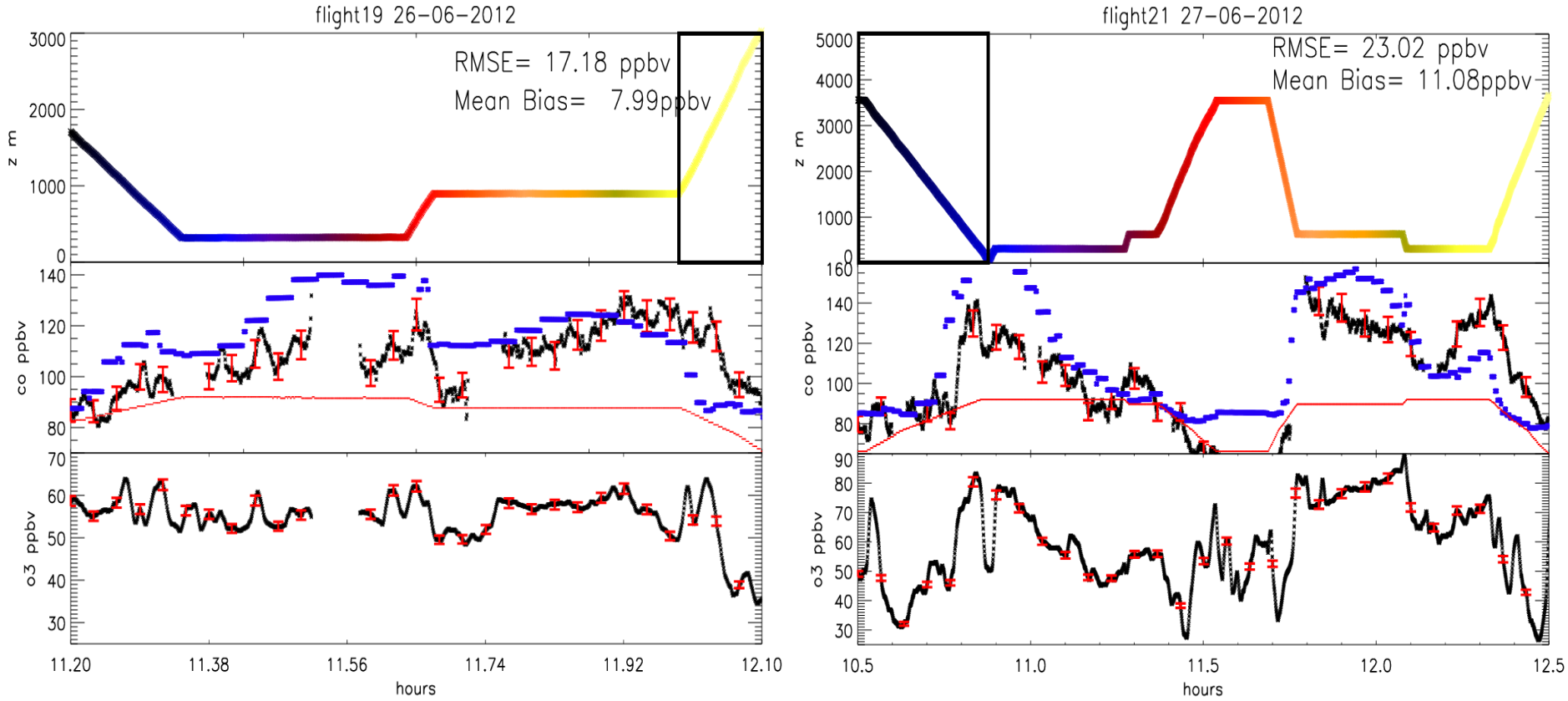

Figure 4.4: Airborne CO measurements from flight 19 (26th June, left panel) and flight 21 (27th June, right panel). Upper panels reports the height of the flight as a function of time. Color shades indicates the position of the flight (see figure 4.6). Middle panels report the corresponding measured CO concentration (black line), the WRF-CHEM modelled concentration (blue line), and the background concentration (red line). The Root Mean Square Error (RMSE) and the mean bias between the model and the measures are also indicated. Lower panels reports the O3 concentrations. Black boxes highlight the part of flights profiles that are analyzed in more detail in figure 4.5. Error bars are reported in red.

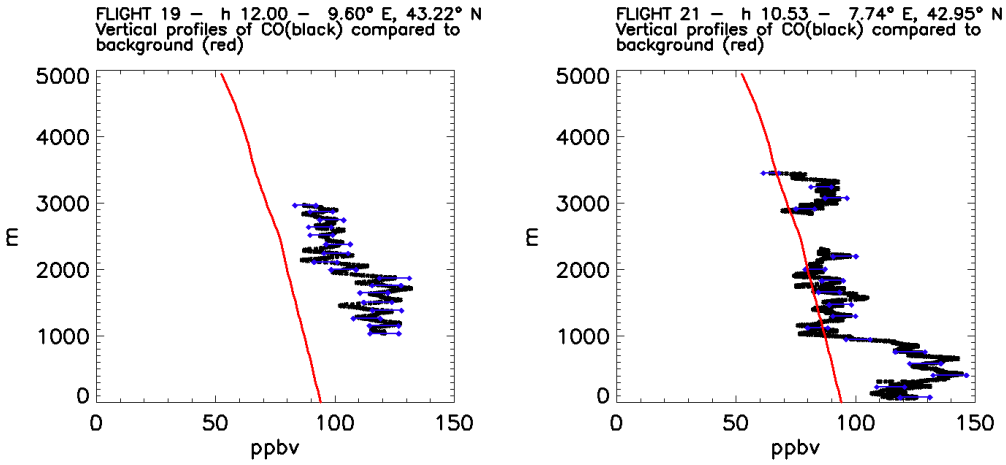

(a) 26th June 12:00 UTC

(b) 27th June 10:53 UTC

Figure 4.5: CO concentration profiles from flight 19 (26th June, panel (a)) and flight 21 (27th June, panel (b)) corresponding to the boxes highlighted in figure 4.4. Measurements (black line) are compared with the estimated background profile (red line). Error bars are reported in blue

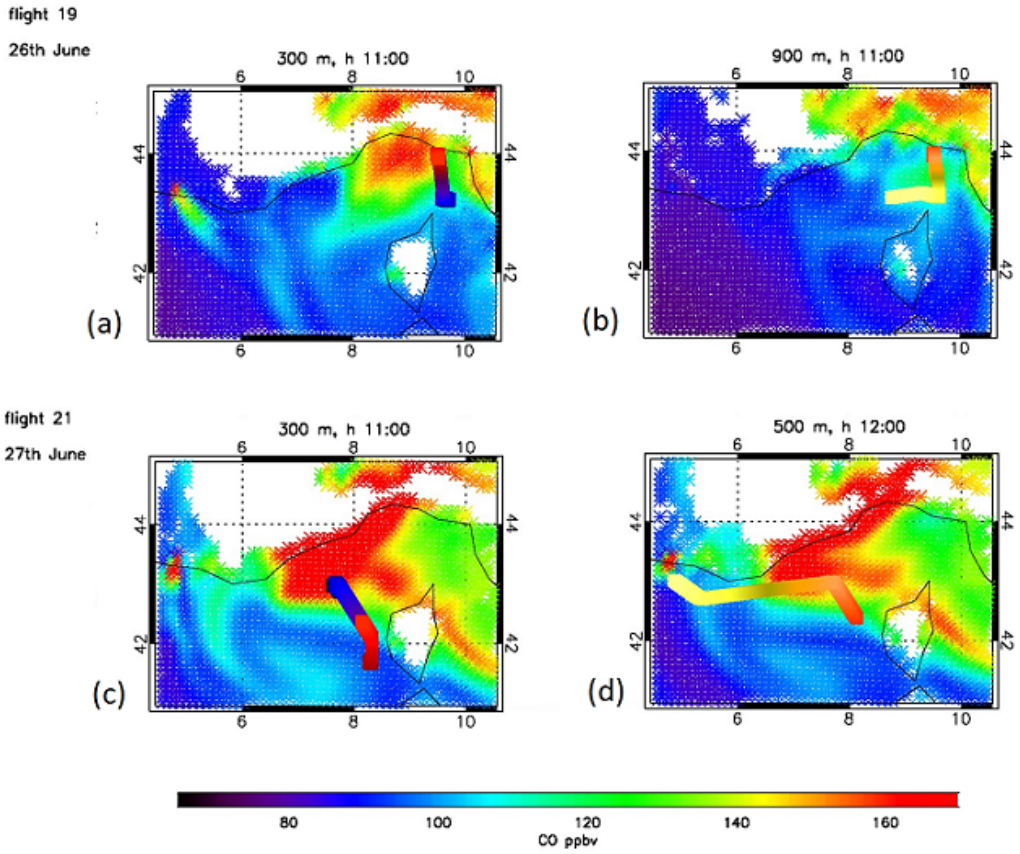

Figure 4.6: Flights position respect to the horizontal section of CO concentration from WRF-CHEM simulations. Colored tracks represents the time evolution of the flight measurements accordingly to figure 4.4. Upper panels refer to flight 19 (26th June), lowers panel to flight 21 (27th June)

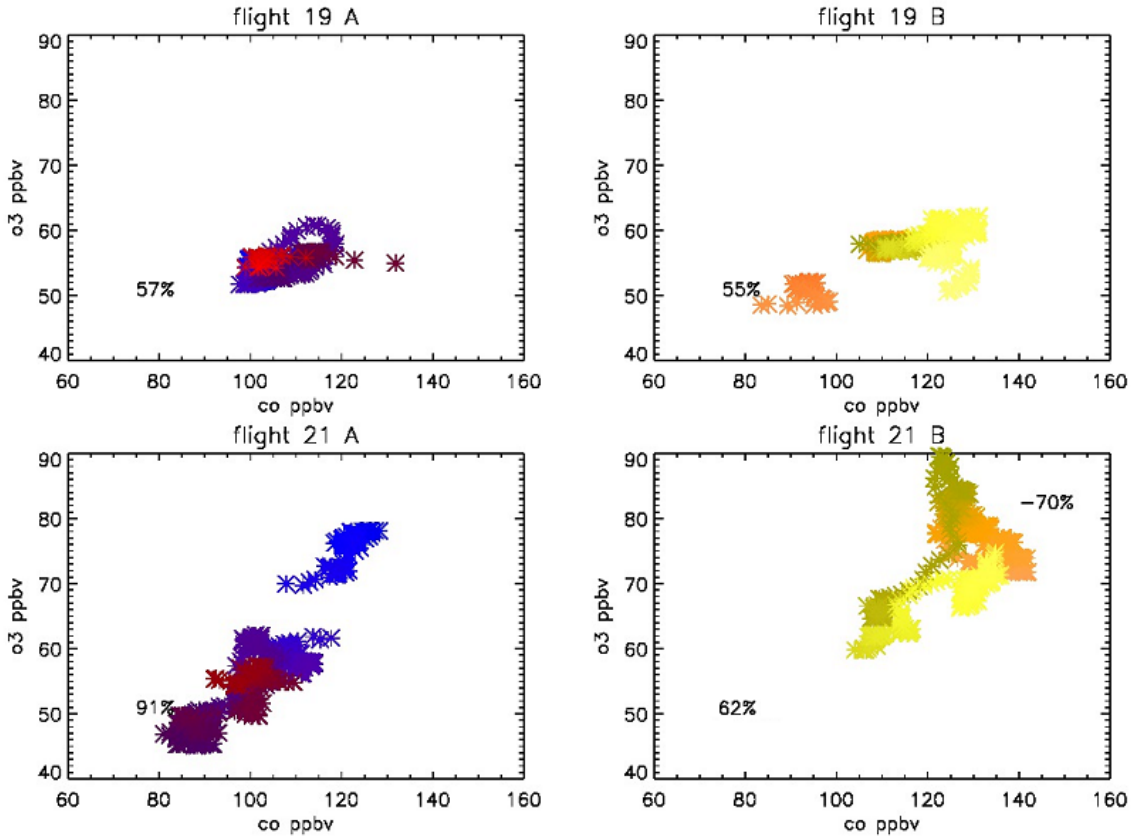

Figure 4.7: Scatterplots of O3 - CO concentrations for flight 19 (upper panel) and flight 21 (lower panel). Colors indicate the position of the flights as reported in figure 4.6. The correlation between the two quantities is also reported

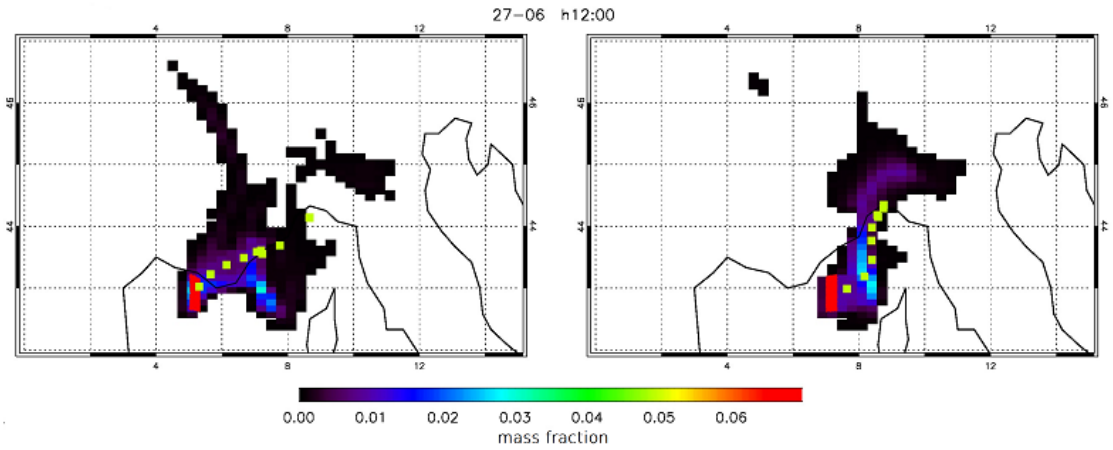

Figure 4.8: Backtrajectories released from two different point of flight 21 (indicated in red): Longitude 5°E (left panel) and 7°E (right panel). Colors indicate the massfraction that will influence the concentration observed by the flight. Squares indicate the position of the center of mass each 3 hours.

by relative humidity, registered during the flight, of around 70%) can be explained by a ozone destruction caused by titration by NOx near the source/inside the plume [97, 90]. Nevertheless, due to the absence of NO_2 observation on board of the aircraft, this hypotesis can not be directly proved. Subsequently (after time 12.3) the flight entered in a different pollution plume with again an increase in both CO concentration (from 120 to 140 ppbv) and O3 concentration (from 62 to 70 ppbv) and a positive correlation (62%). This region, accordingly to backtrajectories, is no more under the influence of the Po Valley outflow but instead if affected by short range air transport from the French coast (see figure 4.8 comparing left panel, indicating French influence, to right panel, indicating Po Valley contribution to the flight section). This is visible also as a small and confined CO plume in figure 4.6 panel (d), at 5°E Longitude. The WRF-Chem simulation again shows a coherent evolution with observations with a general overestimate of the CO plume intensity. The RMSE respect to the CO observations is 23.02 ppbv and the Mean Bias is 11.08 ppbv.

Observed CO enhancement, with respect to the baseline, ranges in general between 30 and 50 ppbv, mostly occurring below 2000 m height. Airborne in-situ observations are therefore clearly indicating enhancements in the CO concentration in the Gulf of Genoa area. The WRF-Chem simulations shown in figure 4.6 suggests the presence of polluted plumes that seems to originate from the Po-Valley. The following section will present a combined use of WRF-Chem outputs with FLEXPART-WRF trajectories to help identify and quantify the effective contribution coming from Po-Valley.

4.3 Dynamics of the export process episodes from the Po valley

To investigate the dynamics a possible outflow plume from the Po Valley, FLEXPART-WRF simulations were performed in forward mode. A cluster of 5000 parcels was released each 6 hours for a time range of 36 hours over the Po Valley region (indicated as a grey shade in figure 4.10 from ground level up to 500m. The outflow plume pattern relative to the 23th-24th June event are presented in figure 4.9: colors represent the fraction of the total released mass (expressed as unitary) advected in each bin during the 36 hours. The figure reports the mass fraction for parcels emitted the June 23 at 00 UTC, when outflow conditions occurs and the plume reaches the Gulf of Genoa area. The temporal evolution of the plume barycenter (marked by red squares each 3 hours) indicates that the plume reaches the Gulf 27 hours after the instant of emission. Figure 4.9 reports also the vertical section of the plume along the barycenter axys each 12 hours. The cross section is an istantaneous picture of the outflow that takes also in account the eventual contribution from previous or subsequent releases with respect to the first release instant (23 June 00:00 UTC). The simulation suggests therefore a cyclonic transport of air masses (visible in the barycenter pattern) reaching the Gulf of Genoa (43-44 °N) after 24-27 hours from release (around the first hours of 24th June). Vertical cross section of mass fraction shows that air masses are uplifted up to 2500-3000 m (see 23th June at 12:00 UTC) coeherently with the PBL analysis of section 3.1.2 that indicates, for these days, a PBL top above 2000m). Air reaches the Gulf of Genoa (between 43.5°N and 44° N) with a plume developed vertically up to 2500m. The cross sections indicates also that the highest contribution is observed below 1000 m near the Ligurian Coast (between 43.6°N - 43.8°N and 7°E - 9°N, see 24th June 06:00 UTC in figure 4.9). Large fraction of the air masses remains over the release area, from 3 to 5 times the fraction that reaches the sea. The shape of the trajectories cluster follow closely the CO plume from WRF-Chem (shown at 500m in figure 4.11) as expected since the two models are driven by the same meteorological fields.

The outflow plume pattern for the 26th-27th June event is presented in figure 4.10. This plume reaches the Gulf between 12 and 30 hours after the instant of emission. Again is visible a cyclonic transport of air masses toward the Gulf of Genoa, with a maximum contribution from the Po Valley expected between 12:00 UTC of 26th June and 12:00 UTC of 27th June). Vertical cross section of mass fraction of the 26th June 12:00 UTC and 27th June 12:00 UTC (corresponding to the times of dive of figure 4.5) shows the presence of air that, originating from the Po Valley, overpasses the orography barrier (reported as a red line) and reaches the Gulf of Genoa with a vertical extended plume up to 1000m in the Southern part and up to 3000m near the coast. A similar pattern, but with a larger fraction of particles

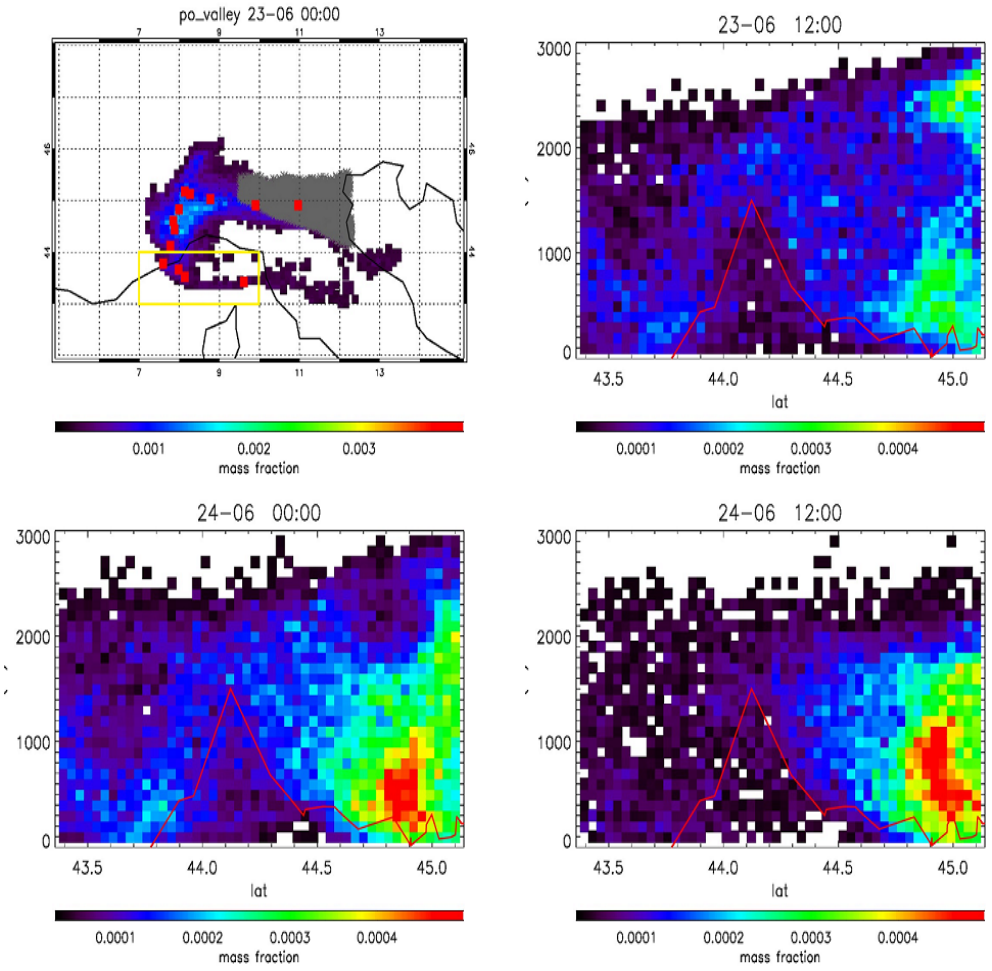

Figure 4.9: Forward trajectories released the 23th June at 00:00 UTC. In the first panel the grey area represents the emissive region of the particles. Colors represent the columnar mass fraction of the total released mass. Red squares indicate the position of the center of mass each 3 hours. The yellow box highlight the region over which the vertical time series of CO will be extracted (see figure 4.14). The following panels report the vertical section of the mass fraction along the center of mass pattern, each 12 hours. Red line represents the orography (extracted from a geographical atlas) met by the plume along the advection

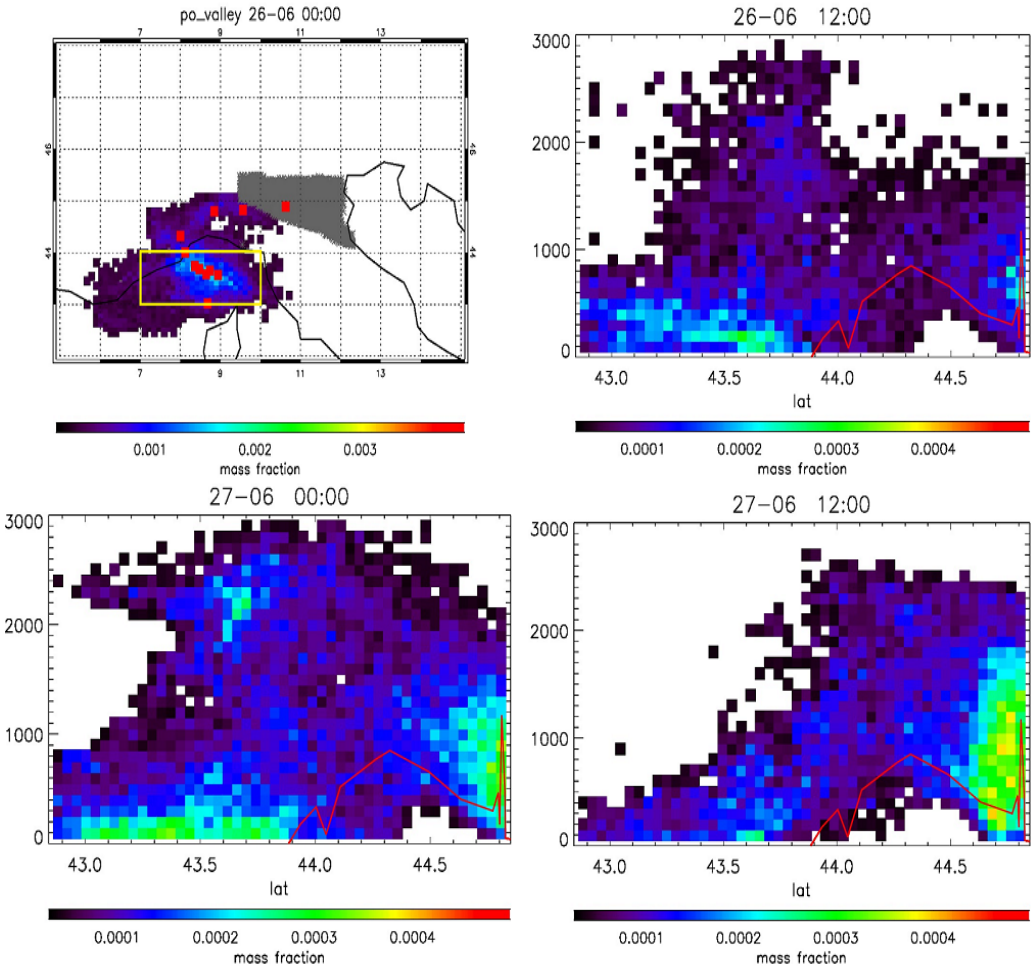

Figure 4.10: As in figure 4.9 but for the 26-06-2012 00:00 UTC release

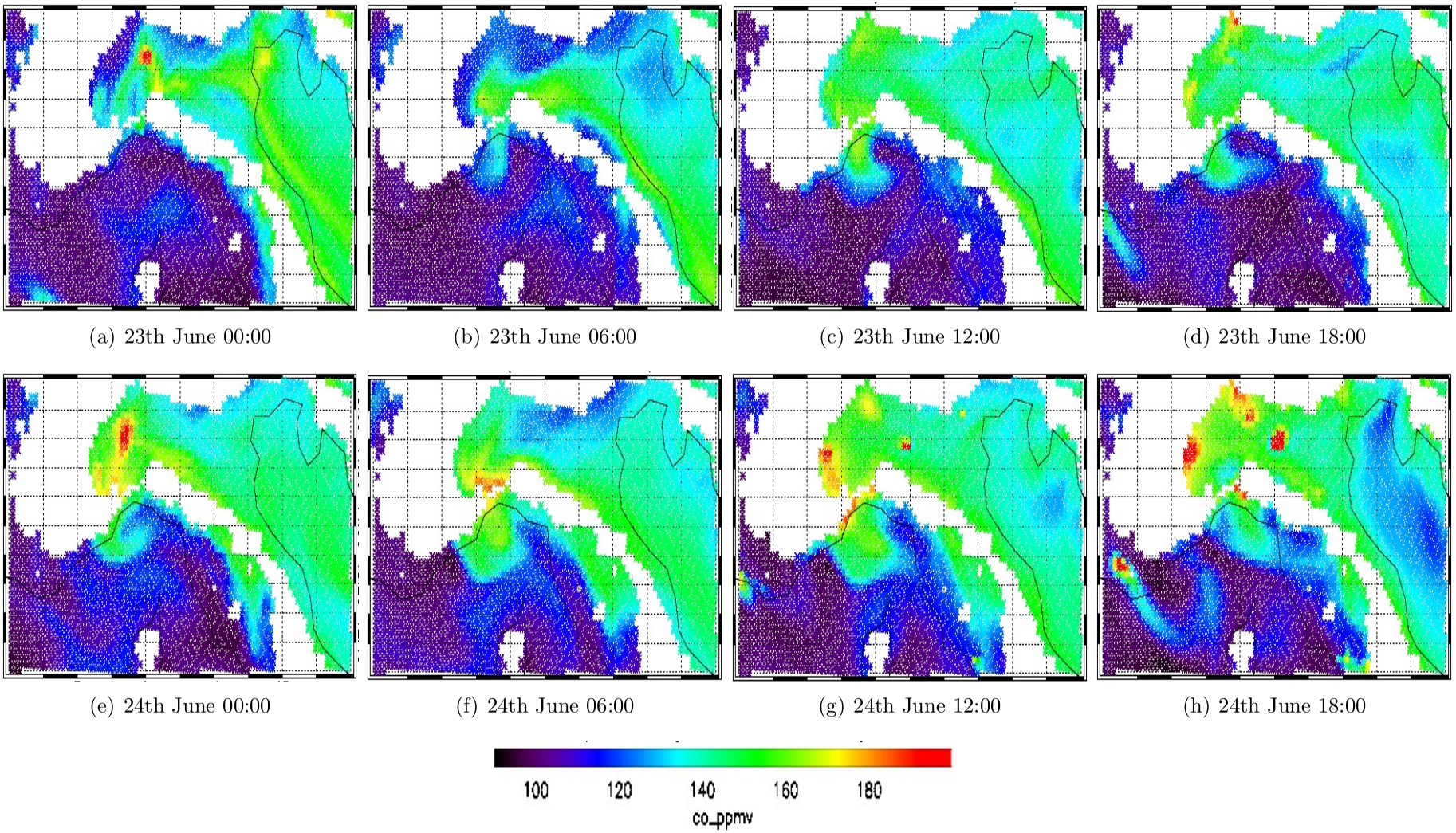

(a) 23th June 00:00 (b) 23th June 06:00 (c) 23th June 12:00 (d) 23th June 18:00

(e) 24th June 00:00 (f) 24th June 06:00 (g) 24th June 12:00 (h) 24th June 18:00

Figure 4.11: Horizontal section of CO concentration at 500m from WRF-CHEM. Each label is a 6 hours step from the beginning of the events as indicated by FLEXPART, figure 4.9

(both under 1000m and at 3000m), is observed the 27th June at 00:00. At 12:00 UTC of June 27th the model shows a descent of the plume below 1000m on the Southern side of the plume section and an accumulation of air masses above the Po Valley. Overall the simulated vertical extent is coherent with the observed vertical profiles (see figure 4.5) that show a main enhancement of CO from sea level up to 2000 m height (and a weaker one above that height) on the 26th and up to 1000 m height on the 27th. The CO plume evolution from WRF-Chem again reflects the Po Valley outflow pattern and is shown at 500m height in figure 4.12.

The CO contribution of the Po Valley plume is evaluated on the whole outflow period (from 23th June to 27th June) on a vertical column situated in correspondence of the yellow box of figures 4.9 and 4.9. The FLEXPART forward simulation where coupled with the total mass of CO contained in the release volume, extracted from WRF-CHEM simulations. Is possible then to estimate of the enhancement in concentration, computed as the fraction of the total CO mass released from the Po Valley over the volume of the column taken in analysis. The timeserie of the mean concentration is reported, expressed in ppbv, in figure 4.14. The two events of outflow (23-25 June and 26-28 June) are visible as CO enhancement up to 50 ppbv below 500 m height for the first event and up to 70 ppbv for the second event. The simulation indicates contributions between 10 and 20 ppbv above 1000m height in both events, up to 3000m. As the outflow pattern encompasses also the Northern-Western Part of Italy the role of local emissions have also been estimated. Forward plumes are emitted from the Ligurian coast and initialized with CO derived from WRFChem as done for the Po-Valley experiment. The release area is indicated as a grey shade in figure 4.13. CO contribution is reported in figure 4.14 bottom panel; Ligurian CO influence on the Gulf o Genoa is more continuos during the 23th-28th days but with a maximum contribution inferior to 10 ppbv. This provide indication that, based on this model-driven analysis, Po-Valley export has a substantial impact on the CO budget observed over the Northern Tyrrenhian Sea.

This joint analysis shows clearly that the observed CO enhancement, quantified to be between 30 ppbv (for the 26th event) and 60 ppbv (27th event), is attributable to the outflow from the Po Valley.

4.4 Systematic estimate over the whole 2012 year

A continuous FLEXPART-WRF run for the whole 2012 year was performed to identify any seasonal variability in the export events. WRF meteorological input used for this analysis are taken from a one year run with a configuration similar to the one adopted for WRF-Chem but with a coarser resolution (30x30km). A comparison (not shown here) between the two simulations were performed basing on the FLEXPART trajectories showing that both the WRF fields reproduced the same

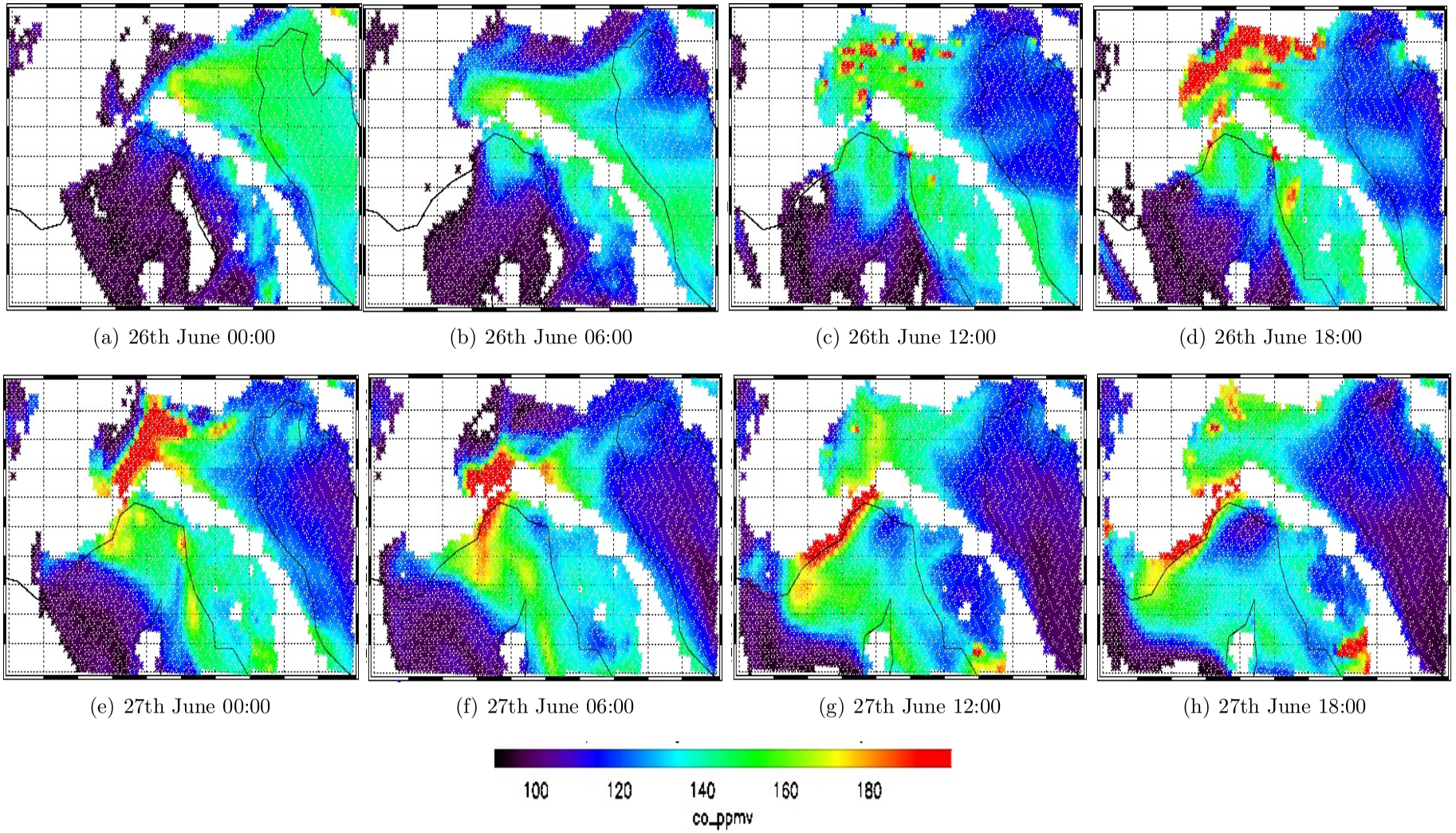

(a) 26th June 00:00 (b) 26th June 06:00 (c) 26th June 12:00 (d) 26th June 18:00

(e) 27th June 00:00 (f) 27th June 06:00 (g) 27th June 12:00 (h) 27th June 18:00

Figure 4.12: Horizontal section of CO concentration at 500m from WRF-CHEM. Each label is a 6 hours step from the beginning of the events as indicated by FLEXPART, figure 4.10

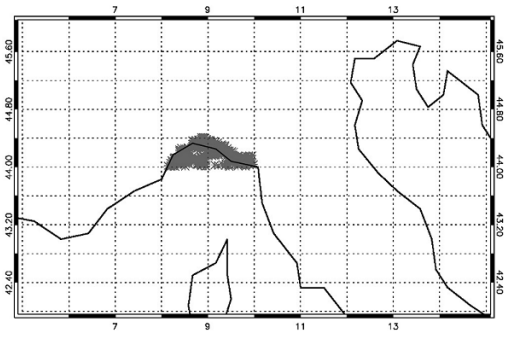

Figure 4.13: Release area for forward trajectories relative to Ligurian Coast contribution, indicated as a grey shade.

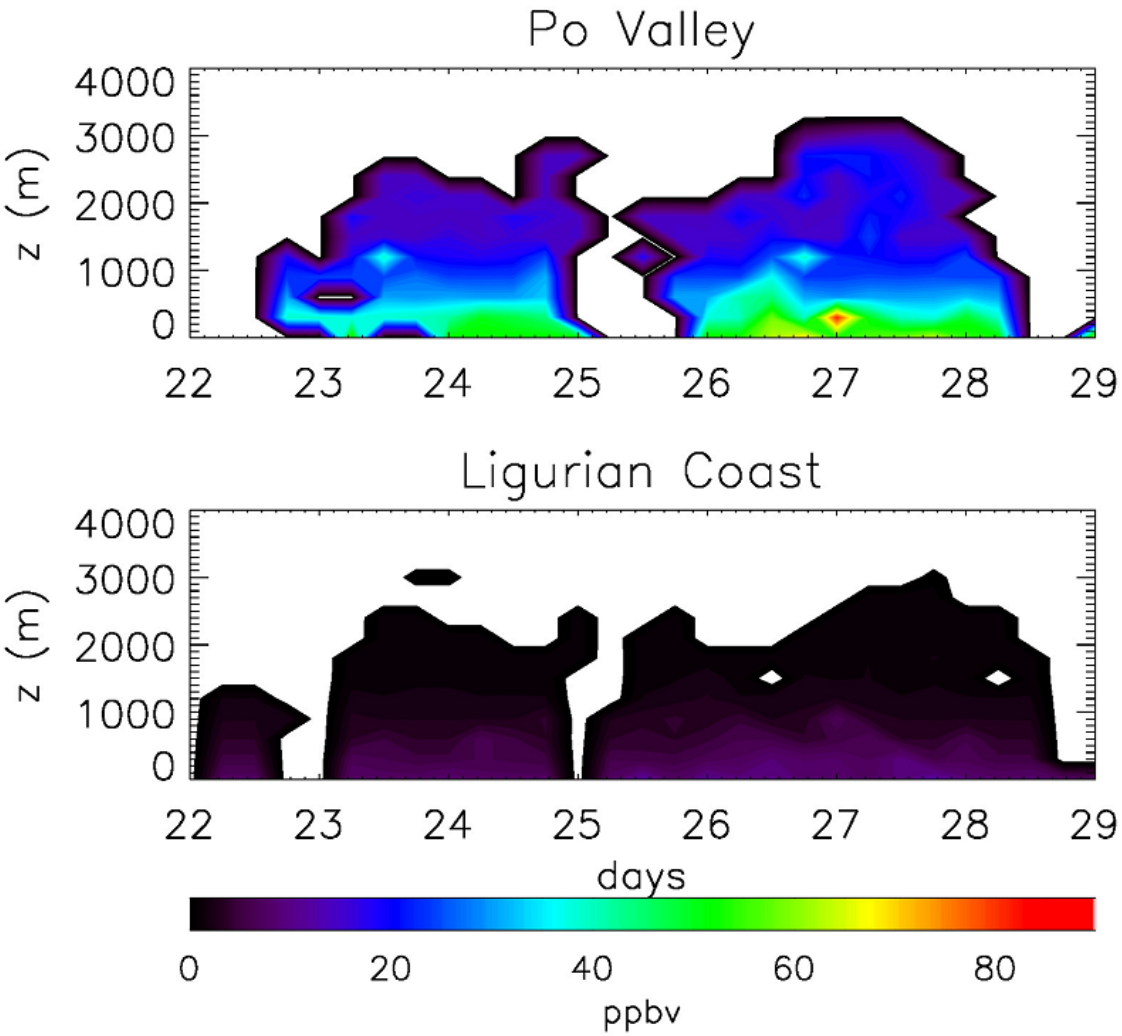

Figure 4.14: CO contribution over the background concentration of Po Valley (upper panel) and Ligurian Coast (lower panel) on a vertical column delimitated by the yellow box of figure 4.10

export events for the June 2012 month. Using the one year long WRF meteorological input, 5000 FLEXPART-WRF particles were then released each 6 hours for 36 hours forward in time, from the same volume box used for the June simulation of figure 4.14. As the chemical simulation was not available for the other months, the BRACE stations (see figure 2.1) observations along the year were used to have an estimate of the annual evolution of the Po Valley CO concentration. In figure 4.15 each grey star reports a single hourly measurement from each of the eleven BRACE stations. High values of CO concentration (higher than the 10mg/m3 limit set by the European Air Quality standards, http://ec.europa.eu/environment/air/quality/standards.htm) is explained as the majority of the BRACE stations is situated near urban and traffic sites. The continuous line represents the daily mean over the whole dataset. The annual cycle shows higher concentrations of pollution during winter months and minima during summer season. Such variability was already observed over Italy [28, 38] and it can be explained as the result of several contributions: a variability on natural and anthropogenic emissions as during winter increased strength of specific sources (mainly residential heating) causes higher concentrations with respect to warmer seasons; a variability on the PBL evolution that in winter is less developed with respect to summer, causing an increased accumulation of pollution close to the ground; a variability on the production and removal processes with reduced solar radiation during the cold months and therefore a reduced OH production. CO therefore shows a longer lifetime in winter with subsequent accumulation [200]. Annual evolution in the CO mass over Po Valley (CO_{annual}) is estimated normalizing the BRACE daily mean over the year ($CO_{annual_{BRACE}}$) with the mean BRACE value over the last week of June ($< CO_{week_{BRACE}} >$) and then multiplied for the mean CO mass predicted by WRF-CHEM for the same week ($< CO_{week_{BRACE}} >$):

$$CO_{annual} = \frac{CO_{annual_{BRACE}}}{< CO_{week_{BRACE}} >} \cdot < CO_{week_{WRF-CHEM}} > \tag{4.1}$$

The resulting value was therefore used as input for the annual series of forward FLEXPART-WRF simulations. Results are shown in figure 4.16. The upper panel reports the mass fraction over a 1000m column on Gulf of Genoa (highlighted by the yellow box of figure 4.9 and 4.10) coming from Po Valley export. Trajectories indicate a seasonal cycle on the export events: persistent export of Po Valley air masses toward the Tyrrenean sea are observed between February and March and between November ad December when up to 20% of the released mass reaches the Gulf of Genoa. More isolated events were also observed in mid April and May and in the last week of August. The June events analyzed in the previous sections appears to be among the less intense export episodes, with a mass fraction contribution of around 5% of the total released mass from the Po Valley. The coupling with the CO mass annual variability lead to a more marked seasonality, where greater contributions are found in the month of February (1500 tons of CO with a maximum

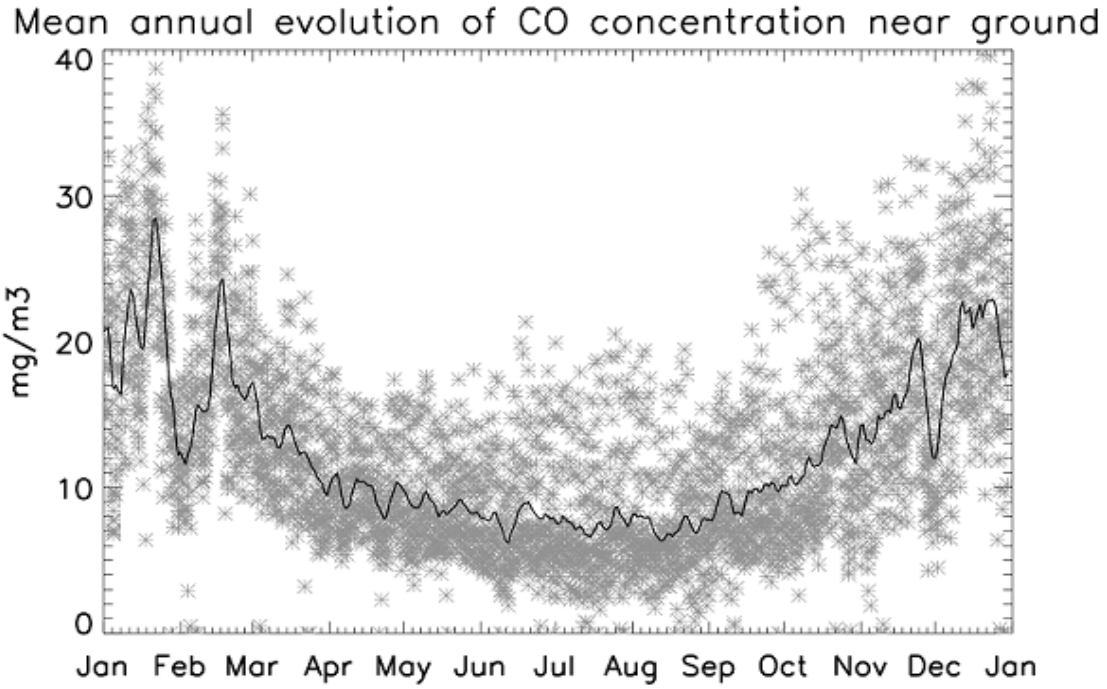

Figure 4.15: Annual evolution of CO concentrations at the ground over Po Valley estimated as a mean from all the BRACE stations.

of 2000 tons at the end of the month). The exported mass is then decreasing to reach a minimum in the June-July months and start to increase again after September, with a second strong export phase between November and December (around 1000 tons contribution). Last panel reports weekly CO concentration computed as "plume contribution": the CO concentration was evaluated as total mass exported on the volume of the outflow plume. Reader should notice therefore that the values of concentration are an evaluation of a local enhancement, related on the geographical extension of the plume. In general is possible to notice that the local increase due to export is varying between 30 ppbv (observed mainly during spring-summer months) and 60 ppbv (February-March, October-November).

Finally, figure 4.17 shows the seasonal pattern of Po Valley outflow as exported mass fraction. Is possible to notice that the winter season (December-January-February, DJF, panel (a)) shows the most extended plume, both in the West and East side of the Mediterranean, with a relevant fraction of trajectories (around 0.07%) extending southward to 42°N. Almost no transport toward North is found. Such tendency is inverted in spring months (March-April-May, MAM, panel (b)), when the flow indicates an increasing presence of North-Eastward transport with a noticeable influence on the Gulf of Genoa area (up to 0.1% mass fraction between 43-44 °N). During summer months (June-July-August, JJA, panel(c)) the largest part of the transport is directed toward North-East. Advection to the Tyrrenean sea is limited both in extension and intensity, with mass fractions around 0.07%

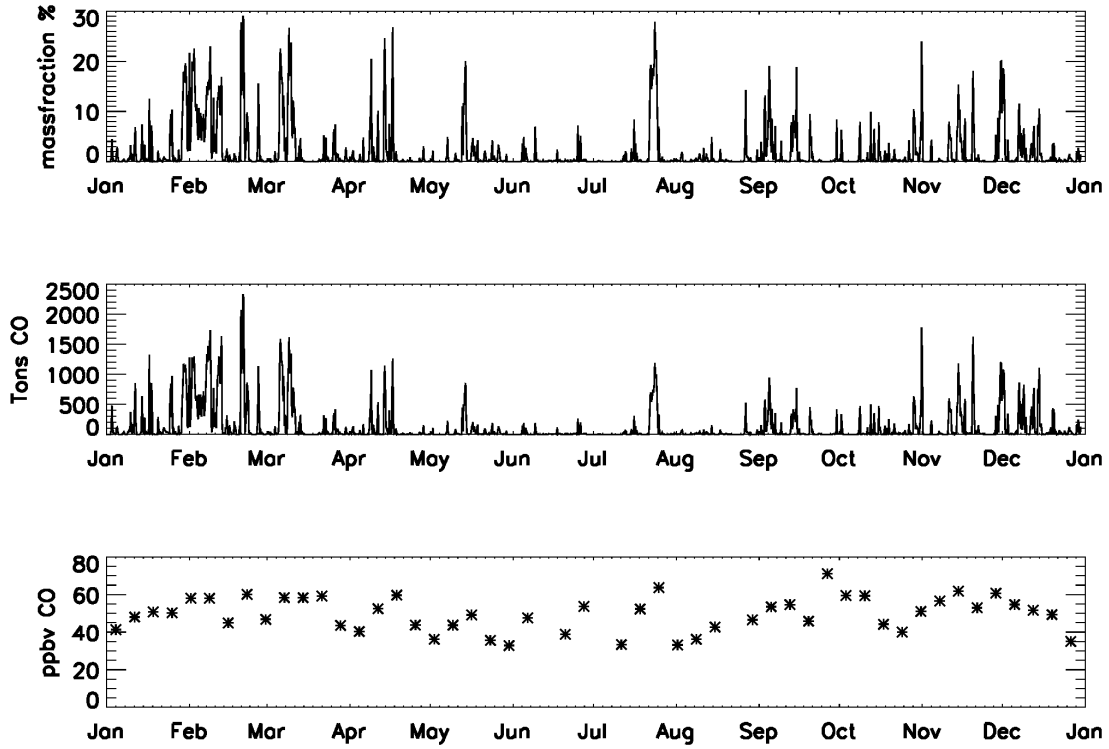

Figure 4.16: Annual evolution of Po Valley contribution over the Gulf of Genoa (yellow box of figure 4.10 and 4.9) expressed as a fraction of the release mass (upper panel), total tons of CO (middle panel), concentration inside the plumes (lower panel)

near the Ligurian coast, rapidly decreasing to 0.05% south of 43°N. During Autumn season (September-October-November, SON, panel (d)) the mean flow approaches winter conditions showing less transport toward North and an increasing contribution in South-West direction. The pattern is then similar to the DJF, but with less extension in latitude and a larger impact on the Ligurian coast area, with mass fraction contribution up to 0.1%.

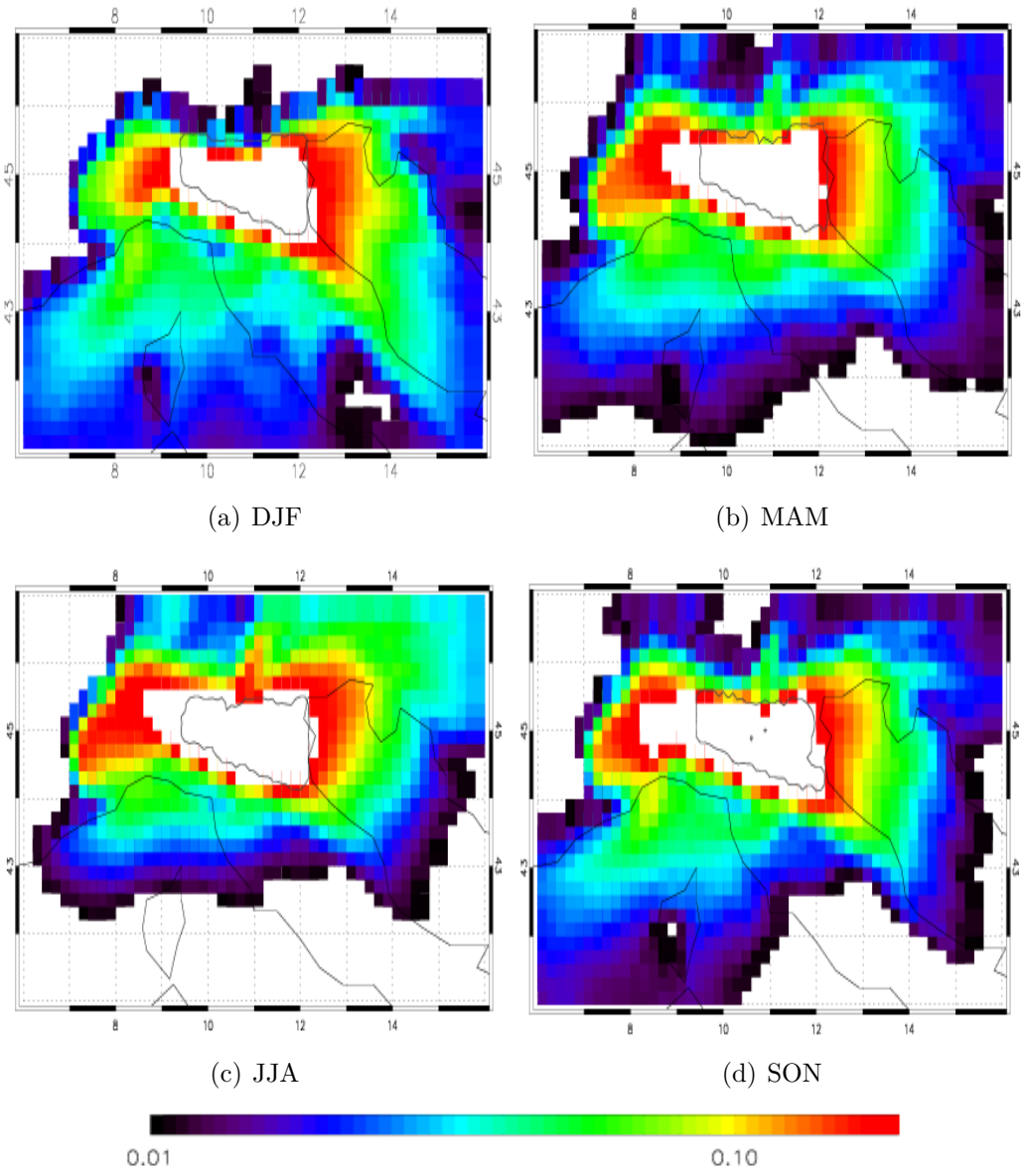

(a) DJF (b) MAM

(c) JJA (d) SON

Figure 4.17: Seasonal fraction of mass of outflow from the Po Valley (the release region is indicated by a contour line). Panel (a) reports the winter season mass fraction (December-January-February), panel (b) spring season (March-April-May), panel (c) Summer season (June-July-August), panel (d) autumn (September-October-November)

Chapter 5

Conclusions

This thesis presents an integrated analysis on the interactions between the summer atmospheric dynamics over Mediterranean Basin and the spatial distribution and chemical/physical properties of several atmospheric compounds. In particular, the main objectives of this thesis were:

1. to describe the vertical evolution of aerosol of different nature, from ground to the top of PBL, as a function of the evolution of transport regimes.

2. to identify and quantify possible episodes of pollution export from the Po Valley to the Gulf of Genoa.

In order to have an insight on the effect of meteorological regimes on aerosol evolution, the analysis of meteorological data was coupled to LIDAR data and in-situ measurements of aerosol size distribution and chemistry. A classification of particles, based on optical and dimensional properties, is presented. Particles were divided in dust aerosol, local spherical particulate and an intermediate class that, basing on the local transport and chemical properties, was alternatively identified as a mixture of dust with local pollution or as local soil mineral aerosol.

Overall the analysis lead to the identification of distinct aerosol regimes:

- The first phase of the campaign (15th-18th June), was characterized by a stagnant meteorological condition (with winds intensities inferior to 5m/s below 2000m), that led to a progressive accumulation of local spherical aerosol in the lower troposphere with increase of the fine aerosol concentration and extinction near the ground. Particles accumulation at the ground followed a clear diurnal cycle with maxima during the early hours of the day when the PBL was still not vertically developed. During daytime particles are instead uplifted and mixed up to 2000m and their vertical distribution reflect closely the PBL evolution.

- Observations and lagrangian analysis allowed a detailed description of two events (19th-21th of June and 29h June-2nd July) of Saharan dust transport.

In addition to other studies that have focused on dust events over North Italy, this work offered evidence of dust entrainment inside the PBL, mixing with local particulate and dust particles descent to the ground. Dust layers were advected above Po Valley from Sahara, travelling along anticyclonic patterns at high level (around 3000-4000 m) and carrying depolarizing aerosol (δ_a varying between 15% and 25%). In both cases the plumes descended to lower heights leading to an increase in the detection of coarse particles (>5 μm) at the ground (from 0.6 μm3/cm3 to more than 1 μm3/cm3). During the second event, dust enters the PBL and mix with local pollution to a larger extent as seen by LIDAR and confirmed also by APS in-situ measurements that detected larger particles concentrations at the ground with respect to the first dust advection episode.

- The intermediate phase (22th-28th of June) was characterized by a decrease in aerosol scattering and particles concentration at the ground. A change in the synoptic patterns indicated conditions of export of polluted air masses toward the Western Mediterranean sea that was analyzed in detail the last part of the thesis.

The combined analysis of in-situ and LIDAR profiles sheds light on less known processes, as the observation of hygroscopical growth in dust rich air. Possible origins of such particles can be found in secondary organic aerosol formation and hygroscopical growth on dust particles with nitrate-enriched surface. As these processes have deep implications on the chemistry, radiation balance and aerosol burden[73] a more complete description based on additional chemistry and dynamics observations would be desirable for a better understanding on the particulate properties over the Po Valley region.

Several events of non-dust intermediate depolarizing aerosol, were also observed up to 2000 m height with a frequency of occurence up to 50% during afternoon-evening hours (15:00-20:00 UTC). Although the available data were not enough to unambiguously identify the nature of such particles, they were reasonably attributed to processes of vertical uplift of soil particles. These events are still not fully characterized and deserve a more in-depth analysis as they may significantly contribute on the local and regional PM concentration.

The intensity and the temporal-spatial extension of export events were extensively analyzed by means of aircraft measurement, FLEXPART forward trajectories and WRF-CHEM simulations. Meteorology and CO fields from WRF-CHEM were first compared with independent observations in the Po-Valley, showing that WRF-CHEM correctly reproduces the meteorological variability over the area and that CO outputs are quantitatively representative of the CO concentration close to the ground. A good agreement is obtained also from the comparison with the MTC

observations of CO at 2100 m height, indicating that the model correctly simulates the vertical motion of pollutants uplift inside the PBL. This mechanism is relevant as, if pollution is transported above the Appennines mountain peaks, it can overcome the orographic barrier and hence can potentially be exported toward the sea. WRF-CHEM and FLEXPART-WRF simulations were then compared to the aircraft observations carried out over the Western Mediterranean basin, showing that models slightly overestimate CO concentration with respect to the observation but offer a very good reproduction of the temporal and spatial evolution of the export plumes. The outflow, transporting pollution over the Gulf of Genoa area, takes place between 23th and 24th June and between 26th and 27th June. There were no flight measurements during the 23th-24th June but the good agreement observed between measurements and models supports the reliability of the simulations results: for the 23th-24th June the outflow transport followed a wide cyclonic pattern, reaching the Gulf of Genoa after 27 hours. The plume extentded up to 2000m height and carried the main CO contribution under 1000m (local increase of around 50 ppbv). During the 26th-27th event, the transport was faster, more direct (reaching the Gulf of Genoa after 12 hours), and more vertically extended (up to 3000m height during the 27th June). During 27th June the influence of the export plume on the Gulf of Genoa appears to be more intense with contribution of up to 60-70 ppbv with respect to the background value. Moreover, a correlation study between O3 and CO observations for the 27th, highlighted the presence of strong photochemical activity with O3 production inside the plume and a region of anticorrelation between O3 and CO that was hypotized to be due to O3 distruction caused by the presence of high concentration of other pollutants like NOx. Genoa export contribution to the CO concentration over the sea was also investigated: results revealed that the impact was limited to values below 10ppbv during both the events. FLEXPART simulations were extended to the whole 2012 year to obtain an estimate on the eventual seasonality of the Po Valley outflow events. The study highlights that pollution export toward the Tyrrenean sea is more likely to happen during Winter months (in particular February and November-December) when the plume can extend down to 42°N, affecting the largest part of the Gulf of Genoa and part of the Corsica region.

Research perspectives This thesis, inserted in the framework of climate change and air quality study, can offer valuable indication on further research in the field of air pollution retrieval.

- The analysis of vertical resolved LIDAR measurement, complemented with in-situ observations, gave an insight on the vertical variability of aerosol of different nature under summer meteorological conditions. A continuos retrieval of LIDAR profiles, both on different season and different years, can give a valuable understanding on the evolution and recursiveness of aerosol events at

local and regional scale. As shown in this work in possible in fact to retrieve information on the level of local accumulation of particles, on the vertical uplift inside the PBL and on the frequency of long range transport events.

- As stated above, the study brought attention to less understood processes as possible hygroscopic particles growth and soil mineral aerosol uplift that may be strongly related to the peculiar characteristics of the analysed region (high levels of anthropogenic pollution, presence of large agricultural field, frequent stagnant conditions, high humidity levels). Additional chemistry and aerosol observations should therefore be implemented to have a deeper comprehension on these processes that may have implication on local and regional air quality.

- The export analysis should also be extended to other pollutants and to longer time period. The insight on the spatial, temporal and chemical properties of the outflow events that such analysis can offer, may constitute valuable knowledge for radiative transfer studies. As already pointed out in the introduction section, export of pollution over the Mediterranean sea can indeed significantly affect the radiative balance of the region with global climatological impacts.

Appendix A

In-situ and remote sensing comparison

A.1 Exctinction profiles indipendent comparison

During the PEGASOS project the Zeppelin NT airship was employed to study aerosols at altitudes between 50–800 m above ground. On 20 June 2012 the Zeppelin collected vertical profiles of aerosol optical properties (aerosol size distribution, hygroscopic growth factor, effective index of refraction and light absorption coefficient) between 50–800 m near the SPC ground station between 08:00 local time (LT) and 14:00 LT with a short refuel break at 10:00–11:00 LT. This offered a unique opportunity for a comparison of the in-situ profiles measurements and LIDAR profile. In-situ aerosol extinction coefficients were computed at the specific wavelenght of $\lambda = 520nm$, as the sum of the absorption aerosol coefficient $\alpha_{a,abs}$ measured by the portable aethalometer (AE42, MAGEE Scientific) mounted on the Zeppelin, and the scattering coefficient $\alpha_{a,sct}$ computed using the particle size distributions, the effective index of refraction and Mie theory (with the assumption to observe spherical particles) [105, 12].

$$\alpha_a = \alpha_{a,abs} + \alpha_{a,sct}$$

$\alpha_{a,sct}$ is determined in dry condition so, to compare with LIDAR profiles (that are measured in ambient condition), it has to be corrected for the umidity. The airborne results where also validated at the ground using aerosol scattering and absorption coefficient from an nephelometer and a multi-angle absorption photometer (MAAP) from the SPC station. Details are explained in Rosati et al. (2015c) [151]. As discussed in section 2.2.2 for the LIDAR equation inversion, the chosen value of LR determines the aerosol extinction coefficient, once the aerosol backscatter, β_a, has been retrieved from the LIDAR measurements. Therefore a sensitivity study on LR has been performed, showing the LIDAR extinction values for LR set to 30, 50 and 70 sr(see figure A.1).

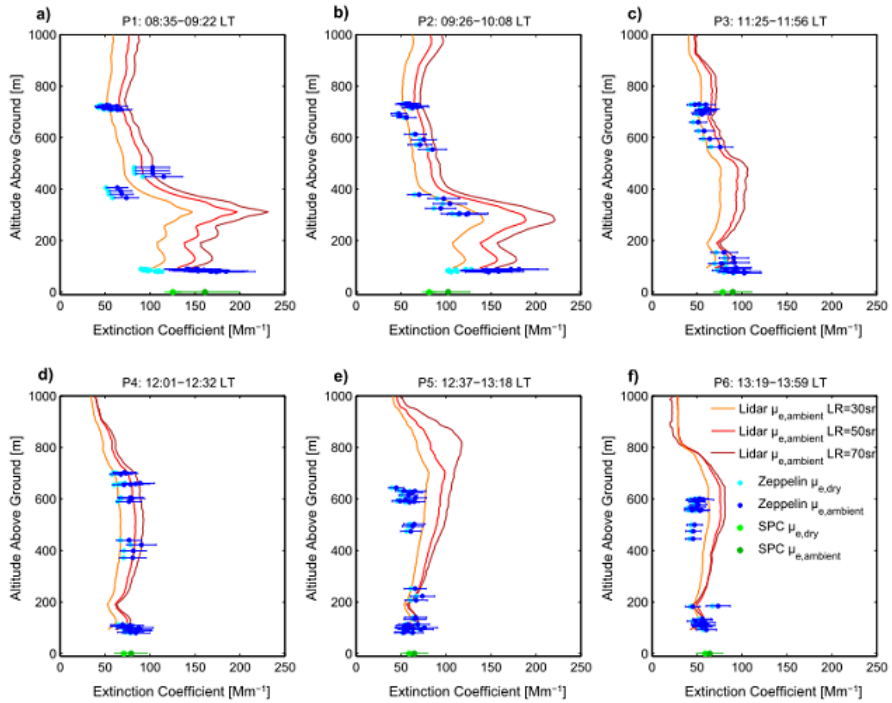

Figure A.1: Extinction coefficients profiles (in Mm-1) over SPC. The continuous lines indicates LIDAR results for LRs values of 30 (orange), 50 (red) and 70 (dark red) sr. The dots describe in-situ results. Light and dark blue dots are dry and ambient airborne extinction coefficients from the Zeppelin measures while the light and dark green dots represent the dry and ambient ground based results, respectively. [151]

The extinction profiles agree quite well in most of the hours, with a general concordance (within 15%) for all the LR values. Largest discrepancies (up to 50%) are found for LRs of 50 and 70 sr above 600 m from the ground after 12:30 Local Time. Choosing LR = 30 sr instead results in a better agreement (within 5–20 %). This altitude dependence may on the one hand be related to actual differences in aerosol properties at different altitudes (not reproduced by a constant choice of LR), but on the other hand potential systematic biases in the overlap correction for low altitudes may also play a role. The comparison in this case appears to be affected by several factors that increase the uncertainties of the analysis like the small temporal window and the low altitudes taken in consideration and the variation on the vertical aerosol distribution that characterized the analyzed day (around midday the 20th June 2012 an event of dust transport reached the ground, as will be shown in the next sections). For this reasons the lidar extiction values, integrated over the whole column, were also compared with a ground based sky-radiometer that collected measures on a longer, continuous period.

A.2 Aerosol optical depth comparison

The aerosol optical depth (AOD) obtained from the column-integrated LIDAR extinction (at 532 nm) was compared to the AOD from a sky radiometer (at 500 nm) operating at the same SPC site [22] within the framework of the SKYrad NETwork (http://atmos2.cr.chiba-u.jp/skynet/). The AOD is a measure of the extinction of the solar beam by dust and haze. In other words, particles in the atmosphere (dust, smoke, pollution) can block sunlight by absorbing or by scattering light. AOD tells us how much direct sunlight is prevented from reaching the ground by these aerosol particles. Usually, for the wavelenght used (500nm), a value of 0.01 corresponds to an extremely clean atmosphere, 0.1-0.2 to average conditions and a value of 0.4, or higher, would correspond to an high aerosol load and very hazy sky [148]. The AOD from LIDAR can be retrieved as [29]:

$$AOD = \int_0^{z_{max}} \alpha(z)dz \tag{A.1}$$

where z_{max} indicates the maximum altitudes of the LIDAR profiles, that in our case is taken to be 7 km. The comparison of the AOD variability during the time frame of the campaign (15 June 2012 to 5 July 2012) is shown in figure A.2:

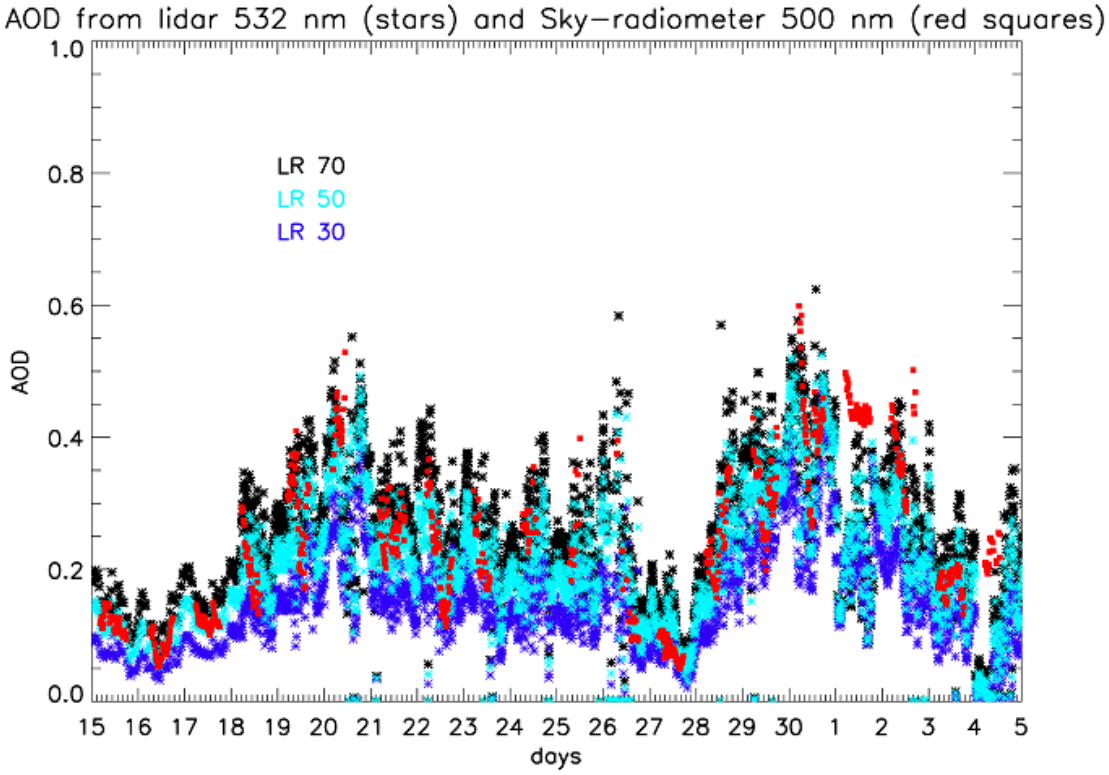

Figure A.2: AOD values retrieved from LIDAR (stars) for different chosen values of continental aerosol LR (30,50,70) in different colors (blue, light-blue and black respectively) compared to the AOD measured by the Sky Radiometer (red squares)

The two datasets showed good agreement. For this period, using a LIDAR

derived AOD with LR equal to 70 sr yielded on average values 7 % higher than those from the sun photometer. Changing the value of LR to 50 and 30 sr resulted in differences of -5% and -25 %, respectively. Thus, in this range of LR values, LIDAR agrees with the sun-photometer in a column-integrated sense, with better agreement in correspondence of 50 LR for the continental aerosol. During days of dust advection (19-22 June 2012 and 29 June - 2nd July, as discussed in the next sessions) better agreement is found for a LR value of 70 sr. (negative deviation of 33%, 20% and 13% for 30,50 and 70sr respectively). It is necessary to consider that the AOD derived from the LIDAR is underestimated respect to the sky radiometer as the first integrates just on the first 7 km while the latter considers the entire atmospheric column. Both the two studies indicate that LR=50 seems to be the better choice for the local aerosol condition during the campaign. Though this can be taken in consideration for further studies on the LIDAR data, this result does not affect significantly the outcomes of the presented thesis.

Appendix B

Error Calculation

B.1 LIDAR errors

As stated in equation 2.7 the scattering ratio is derived from the following equation:

$$R(r) = \frac{N(r) \cdot r^2}{E \cdot C \cdot \beta_m(r) \cdot T(r)}$$

The parameters E and C, that are dependent on the system characteristics, are eliminated in the process of calibration: $R(r)$ is put to $R(r)_{min}$ in correspondence of a height of calibration r* where R(r) is supposed to attains its minimum. Therefore the equation becomes:

$$R(r) = \frac{N(r) \cdot r^2 \cdot \beta_m(r^*) \cdot T(r^*)}{N(r^*) \cdot (r^*)^2 \cdot \beta_m(r) \cdot T(r)} \cdot R_{min}$$

Putting $s = \frac{N(r)}{N(r^*)}$, $\beta_m^* = \beta_m(r^*)$ and $q = \frac{T(r^*)}{T(r)}$ it is rewritten as:

$$R(r) = \frac{r^2 \cdot \beta_m^*}{(r^*)^2 \cdot \beta_m(r)} \cdot s(r) \cdot q(r) \cdot R_{min} \tag{B.1}$$

For a function χ derived from several measured variables u,v,.., the uncertainty in χ can be approximated as:

$$(\delta\chi)^2 = (\delta u)^2 \left(\frac{\delta\chi}{\delta u}\right)^2 + (\delta v)^2 \left(\frac{\delta\chi}{\delta v}\right)^2 + 2C_{uv}^2 \left(\frac{\delta\chi}{\delta u}\right)\left(\frac{\delta\chi}{\delta v}\right) + ... \tag{B.2}$$

where δu and δv are the uncertainties in measured variables u and v and C_{uv}^2 is the covariance between measured variables u and v. Applying this error propagation formula to the scattering ratio expression and neglecting the uncertainty on the altitude r and the covariances between the measured quantities:

$$\left(\frac{\delta R}{R}\right)^2 = \left(\frac{\delta s}{s}\right)^2 + \left(\frac{\delta q}{q}\right)^2 + \left(\frac{\delta\beta_m^*}{\beta_m^*}\right)^2 + \left(\frac{\delta\beta_m}{\beta_m}\right)^2 + \left(\frac{\delta R_{min}}{R_{min}}\right)^2 \tag{B.3}$$

- $\frac{\delta s}{s}$ is the uncertainty on the measured signal s: it has a contribution due to the statistics of photons counting/digital signal δp, estimated as the square root of the numbers of samples $\sqrt{N}$, and a contribution coming from the background noise δbkg, estimated as the standard deviation of the background signal: $\frac{\delta s}{s} = \frac{\delta p}{s} + \frac{\delta bkg}{s}$
- $\frac{\delta q}{q}$ is the error on the transmission T(r) due to both molecular and aerosol extinction and therefore it is dependent on the a priori assumptions made on the relation between aerosol extinction and backscatter coefficients (the lidar ratio, as explained in section 2.2.2). An estimation of the uncertainty induced by such assumption, following the literature, [155] can be evaluated as: $\left(\frac{\delta q}{q}\right)^2 \cong 4 \cdot ((0.5 \cdot \tau_a)^2 + (0.1 \cdot \tau_m)^2)$ where τ_a and τ_m indicate the optical depths due to particulates and molecules, respectively.
- $\frac{\delta \beta_m^*}{\beta_m^*}$ and $\frac{\delta \beta_m}{\beta_m}$ both reflect uncertainties on the molecular density derived from atmospheric model (ERA40[1])). Both of them are put equal to 0.01 [21]
- $\frac{\delta R_{min}}{R_{min}}$ is the uncertainty on the calibration value used in the retrieval. Such uncertainty on R_{min} is put equal to 0.02 [21]

Similarly the uncertainties on the aerosol depolarization δ_a is found applying equation (B.2) to equation (2.11):

$$(\delta\delta_a)^2 = \left(\frac{\delta\delta_a}{\delta\delta}\right)^2 (\delta\delta)^2 + \left(\frac{\delta\delta_a}{\delta R}\right)^2 (\delta R)^2 \tag{B.4}$$

where the uncertainties on volumetric depolarization $\delta\delta$ is computed as

$$\left(\frac{\delta\delta}{\delta}\right)^2 = \left(\frac{\delta s^{\shortparallel}}{s^{\shortparallel}}\right)^2 + \left(\frac{\delta s^{\perp}}{s^{\perp}}\right)^2 \tag{B.5}$$

where $s^{\shortparallel}$ and $s^{\perp}$ are the parallel and perpendicular component of the signal. Examples of scattering ratio and aerosol depolarization profiles with their error bar are reported in figure B.1 for a case with "clean" condition and in figure B.2 for a dust event.

Is possible to notice how the error increases in presence of a larger amount of aerosol along the vertical (because of the increase in the transmission error δq). Nevertheless such uncertainties are not really affecting the results of classifications since in relatively clean atmosphere conditions the error bars are small while, in presence of larger values of both R and δ_a, the possible uncertainties still lies, most

[1]https://climatedataguide.ucar.edu/climate-data/era40

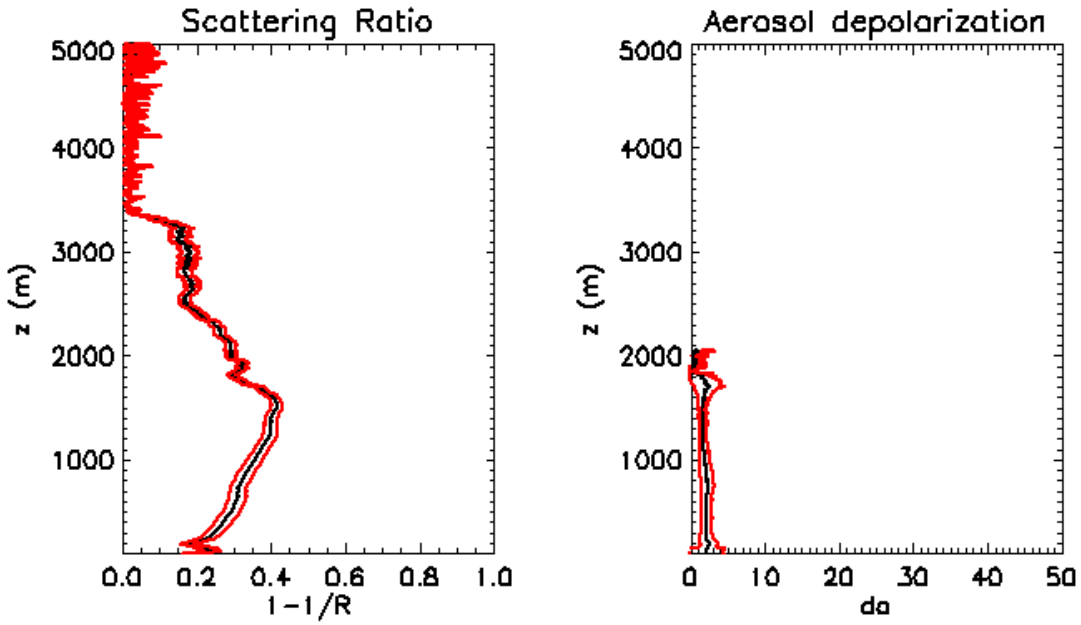

Figure B.1: Left panel: scattering ratio (R(r)) (black) with error bars (red lines). Right panel, aerosol depolarization δ_a (black) and error bars (red lines) for a clean day (17th June at 14:00 UTC)

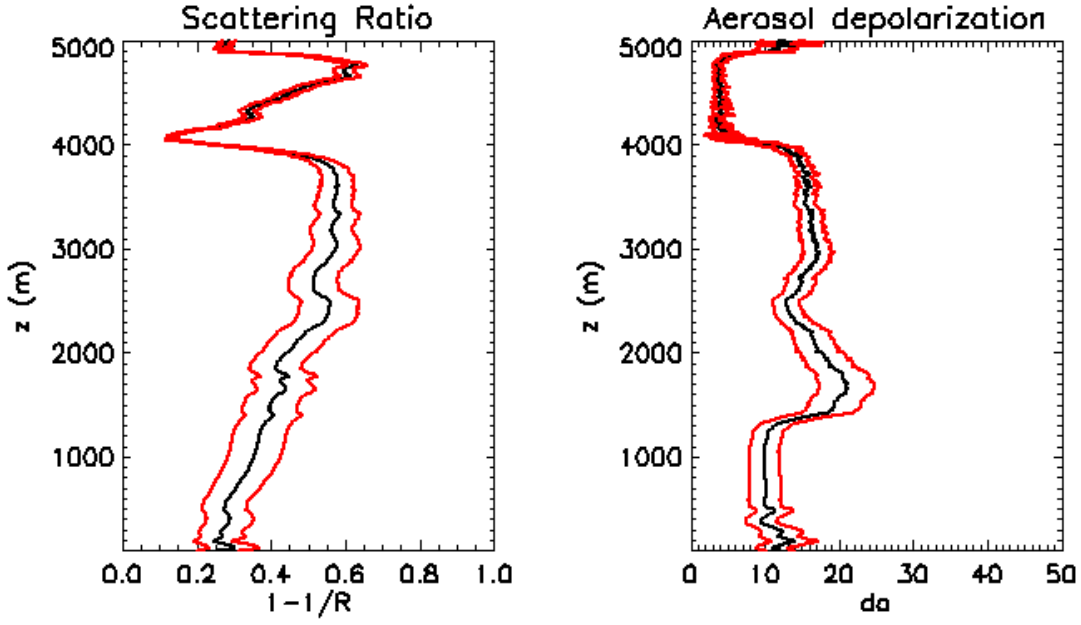

Figure B.2: As in figure B.1 but for a dusty day (30th June at 21:00 UTC)

of the time, in the ranges of classification of figure 2.7. In the other cases the classification is still supported by the presence of coherent patterns of aerosol properties (like shown in figure 2.8) and the jointed studies of trajectories analysis and in-situ measurements. Finally, uncertainties on the aerosol extinction ($\alpha_a = LR \cdot \beta_a$) can be evaluated as:

$$\left(\frac{\delta\alpha}{\alpha}\right)^2 = \left(\frac{\delta\beta_a}{\beta_a}\right)^2 + \left(\frac{\delta q}{q}\right)^2 \tag{B.6}$$

where

$$\left(\frac{\delta\beta_a}{\beta_a}\right)^2 = \left(\frac{R}{1-R}\right)^2 \cdot \left[\left(\frac{\delta s}{s}\right)^2 + \left(\frac{\delta q}{q}\right)^2 + \left(\frac{\delta\beta_m^*}{\beta_m^*}\right)^2 + \frac{1}{R^2} \cdot \left(\frac{\delta\beta_m}{\beta_m}\right)^2 + \left(\frac{\delta R_{min}}{R_{min}}\right)^2\right] \tag{B.7}$$

Uncertainties on the aerosol extinction near the ground, presented in figure 3.8, are reported in figure B.3

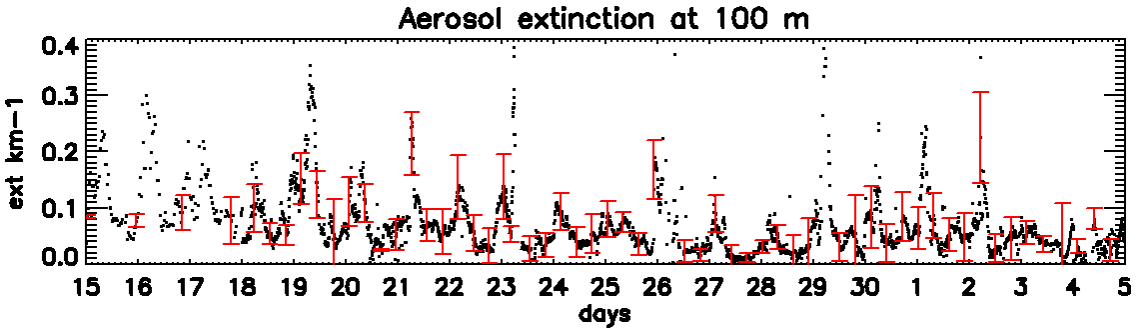

Figure B.3: Lidar extinction (in Km-1) near ground (∼100) with error bars (red)

B.2 OPC errors

Regarding particle number size distributions, three kinds of uncertainties should be considered: the statistical counting uncertainty ϵ_N, the instrumental uncertainty with respect to particle number concentration (sample volume, flow rates, other instrument parameters) ϵ_R and the particle sampling losses (like turbulence diffusion or gravitational settling). The inlets of the instrument are designed to minimize such aerosol losses [2].

As particle counting follows the Poisson statistics, the statistical uncertainty of the particle number concentration can be estimated as:

$$\epsilon_N = \frac{\sqrt{N}}{N} \tag{B.8}$$

[2]Inside the main line, a 2.5m vertical tube made in steel to limitate electrostatic losses, air flows in laminar flux conditions. The isokinetic splitter is a 60cm long and 1/4 inches diameter tube free of bends and made of silicon. A quantitative estimation of the inlets efficiency in such configuration is still not available

The flow rate of the instrument is of 1.2 l/min, therefore each minute the OPC samples a volume V of $1200cm^3$. N therefore can be computed as

$$N = \frac{PNC}{cm^3} \cdot V \tag{B.9}$$

According to the manufacturer, the reproducibility of the Grimm 1.108 OPC in particle counting is $\epsilon_R = \pm 2\%$ [146]. The total relative uncertainties can be therefore estimated as:

$$\epsilon_{tot} = \sqrt{\epsilon_N^2 + \epsilon_R^2} \tag{B.10}$$

The OPC data with the error bars derived from the uncertaintis analysis are reported in figure B.4. Even if the error bars are large and in some points reaches the 50% the two dust events (20th June - 22th June and 30th June - 2nd July) can still be distinguished from the dust free days.

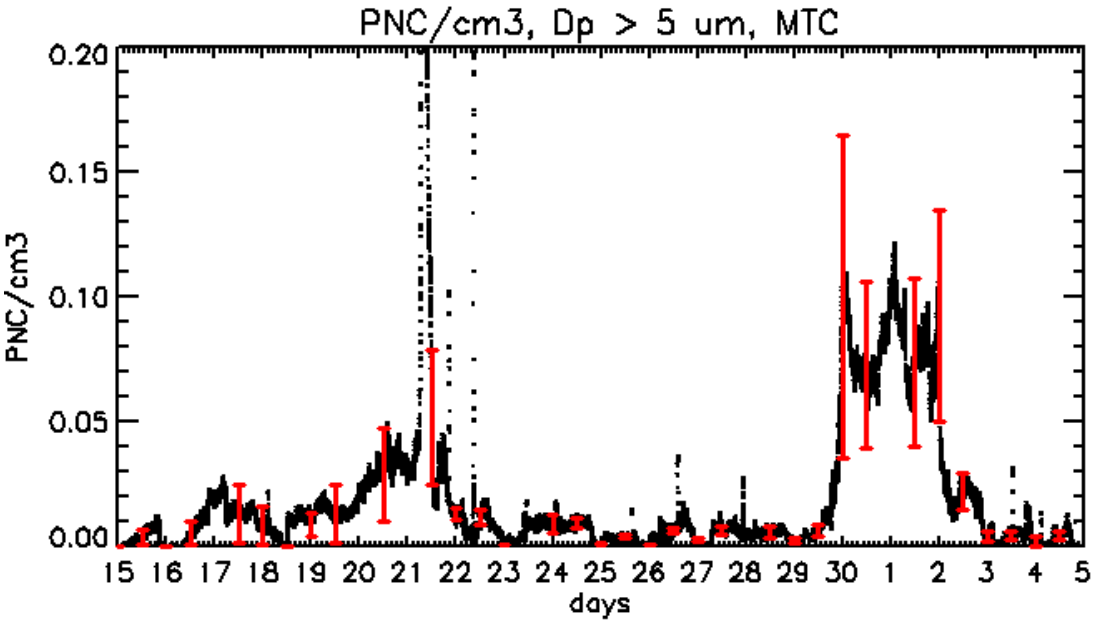

Figure B.4: OPC coarse particles concentration (black) with error bars (red)

B.3 APS errors

To provide accurate size distributions, the APS must determine both particle size and number concentration correctly. Uncertainties on the diameter is found to be of 10% [139]. Manifacturers suggests instead that uncertainties on the concentration of particles has to be estimated as ±10% of reading plus variation from counting statistics (evaluated in a similar way as for the OPC). The uncertainties on the particles counting N is therefore taking in account such contributions, similarly to what presented in equation B.10 for the OPC measures. According to Volckens and Peters (2005) [191], model 3321 APS spectrometer shows near 100% efficiency in

solid particles countings (that is our case, as the measures analyzed here refer to dry particles) As in our analysis we make use of the particle volume, computed as

$$Vn = N \cdot \left(\frac{Dp}{2}\right)^3 \cdot \frac{3}{4} \cdot \pi \tag{B.11}$$

the associated uncertainty is:

$$(\delta Vn)^2 = \left(\frac{\delta Vn}{\delta N}\right)^2 (\delta N)^2 + \left(\frac{\delta Vn}{\delta Dp}\right)^2 (\delta Dp)^2 \tag{B.12}$$

Figure B.5 reports the Volume contribution for the diameters Dp=523nm and Dp=5048. The image shows that for the smaller particles the uncertainty is small compared to the variability on the values. For the coarser aerosol the uncertainties are larger but still not affecting the data interpretation.

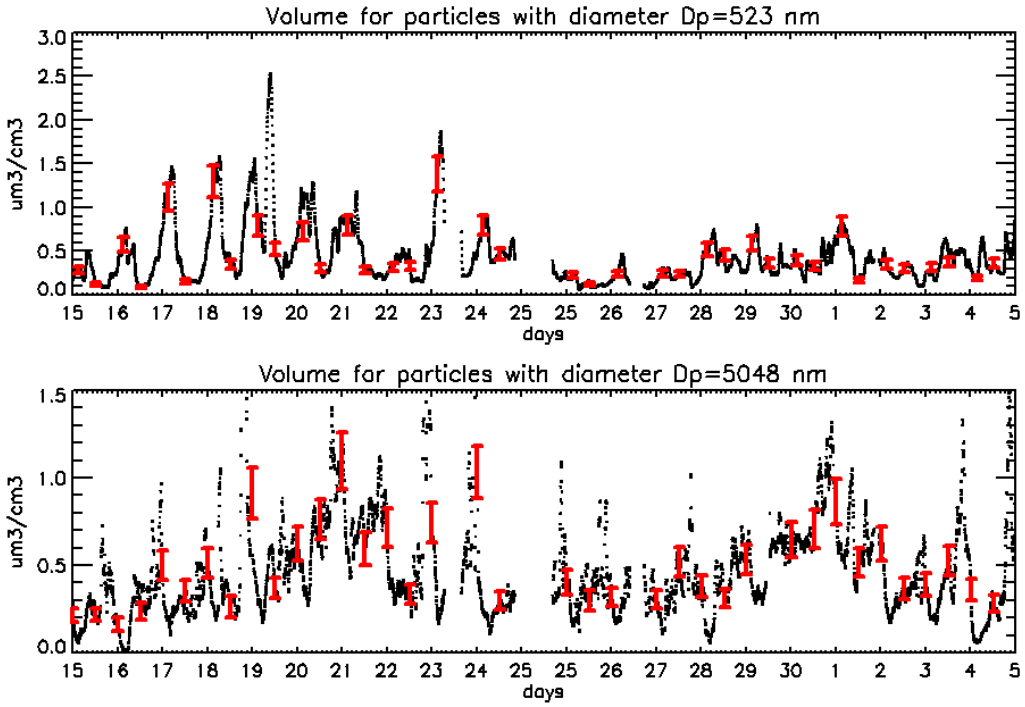

Figure B.5: APS volume contribution (black) with error bars (red) for particles with Dp =523 nm (upper panel) and Dp=5048 nm (lower panel)

B.4 MARGA instrument

The quality of the MARGA instruments retrievals appears to depend mostly on the inaccuracy of the instrument itself (estimated to be ϵ_R <10% for each specie) and the effect of the inlet system ϵ_L[160]. The wall losses were calculated to be varying from 1 to 2 % for SO_2^{-4}, HNO_3^+, NO^{-3}, HCl^+,Cl^-, and to be less than 0.1 % Na^+

for NH^{3+} and NH^{+4} [160]. Following an approach similar to the one adopted for the previous sections we obtain:

$$\epsilon = \sqrt{\epsilon_R^2 + \epsilon_L^2} \tag{B.13}$$

Figure B.6 reports the error bars relative to nitrates measures. In figure 3.15 we

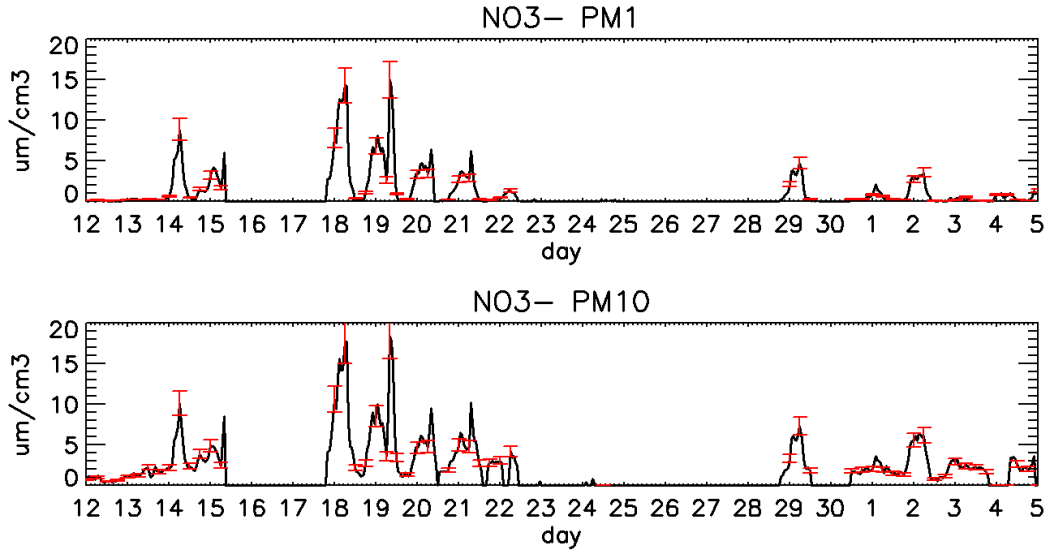

Figure B.6: Nitrates concentration (black) for the PM1 (upper panel) and PM10 (lower panel) channels with error bars (red)

make use of the Ca^{2+} PM10 and total PM10 concentration ratio to have an intensive parameter to compare with aerosol depolarization. In that case the uncertainties should be computed as:

$$\epsilon = \sqrt{\epsilon_{Ca}^2 + \epsilon_{Tot}^2} \tag{B.14}$$

where ϵ_{Ca} and ϵ_{Tot} represent the relative error on Ca^{2+} PM10 and total PM10 concentrations respectively. The same approach should be followed for the volume ratio (Volume from large particles/Volume from fine particles) from the APS. Results of figure 3.15 are therefore reported here with their correspondent error bars (figure B.7):

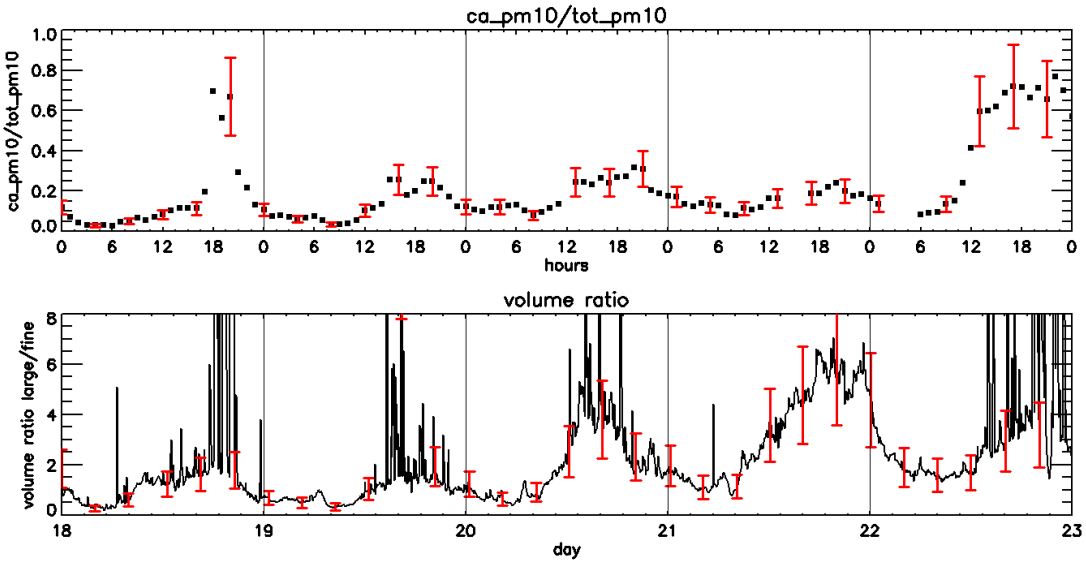

Figure B.7: Increase in the Ca^{2+} PM10 ion concentration respect to the total PM10 ion concentration from MARGA are reported in the upper panel. Lower panel reportes the increase in large particles (2.5 μm <Dp <5.5 μm) fraction respect to the fine ones (0.5 μm <Dp <1 μm) from the APS. Error bars for both parameters are reported in red

Bibliography

[1] Ackermann, I. J., et al., Modal Aerosol Dynamics Model for Europe: Development and first applications, Atmos. Env., 32, 17, 2981-2999, 1998

[2] Amiridis, V., Balis, D. S., Kazadzis, S., Bais, A., Giannakaki, E., Papayannis, A., and Zerefos, C.: Four-year aerosol observations with a Raman lidar at Thessaloniki, Greece, in the framework of European Aerosol Research Lidar Network (EARLINET), J. Geophys. Res., 110, D21203, doi:10.1029/2005JD006190, 2005.

[3] Ancellet, G., and F. Ravetta, Analysis and validation of ozone variability observed by lidar during the ESCOMPTE-2001 campaign, Atmos. Res., 74, 435 – 460,2005

[4] P. Alpert, Y.J. Kaufman, Y. Shay-El, D. Tanre, A. da Silva, S. Schubert, J.H. Joseph; Quantification of dust-forced heating of the lower troposphere; Nature 395(24); 1998

[5] Archer-Nicholls, S., Lowe, D., Darbyshire, E., Morgan, W. T., Bela, M. M., Pereira, G., Trembath, J., Kaiser, J. W., Longo, K. M., Freitas, S. R., Coe, H., and McFiggans, G.: Characterising Brazilian biomass burning emissions using WRF-Chem with MOSAIC sectional aerosol, Geosci. Model Dev., 8, 549-577, doi:10.5194/gmd-8-549-2015, 2015.

[6] Artale, V., Calmanti, S., Carillo, A., Dell'Aquila, A., Herrmann, M., Pisacane, G., Ruti, P. M., Sannino, G., Struglia1, M. V., Giorgi, F., Bi, X., Pal, J. S., Rauscher, S. and The PROTHEUS Group: An atmosphere–ocean regional climate model for the Mediterranean area: assessment of a present climate simulation, Clim. Dynam., 35, 721–740, 2010.

[7] Astitha, M., Kallos, G. and Katsafados, P.: Air pollution modeling in the Mediterranean Region: Analysis and forecasting of episodes, Atmospheric Research, 89, 358–364, 2008

[8] Basart, S., Pérez, C., Nickovic, S., Cuevas, E., and Baldasano, J. (2012). Development and evaluation of the BSC-DREAM8b dust regional model

over Northern Africa, the Mediterranean and the Middle East. Tellus B, 64. doi:http://dx.doi.org/10.3402/tellusb.v64i0.18539

[9] Behrendt, A. and Nakamura, T. : Calculation of the calibration constant of polarization lidar and its dependency on atmospheric temperature, Optics Exp., 10, 805–817, 2002.

[10] Beljaars, A.C.M., 1994: The parameterization of surface fluxes in large-scale models under free convection. Quart. J. Roy. Meteor. Soc., 121, 255–270.

[11] Bergamo, A., Tafuro, A. M., Kinne, S., De Tomasi, F., and Perrone, M. R.: Monthly-averaged anthropogenic aerosol direct radiative forcing over the Mediterranean based on AERONET aerosol properties, Atmos. Chem. Phys., 8, 6995-7014, doi:10.5194/acp-8-6995-2008, 2008

[12] Bohren, C. F. and Huffman, D. R.: Absorption and Scattering of Light by Small Particles, WileyVCH Verlag GmbH, doi:10.1002/9783527618156, (2007), 18617

[13] Bonasoni, P., F. Evangelisti, U. Bonafè, F. Ravegnani, F. Calzolari, A. Stohl, L. Tositti, O. Tubertini, and T. Colombo (2000a), Stratospheric ozone intrusion episodes recorded at Mt. Cimone during the VOTALP project: Case studies, Atmos. Environ., 34, 1355–1365.

[14] Bonasoni, P., P. Cristofanelli, F. Calzolari, U. Bonafe´, F. Evangelisti, A. Stohl, R. van Dingenen, T. Colombo, and Y. Balkanski (2004), Aerosol-ozone correlations during dust transport episodes, Atmos. Chem. Phys., 4, 1201 – 1215.

[15] Boucher, O., Randall, D., Artaxo, P., Bretherton, C., Feingold, G. and co-authors. 2013. Clouds and aerosols. In: Climate Change 2013: The Physical Science Basis. Contribution of Working Group I to the Fifth Assessment Report of the Intergovernmental Panel on Climate Change (eds. T. F. Stocker, D. Qin, G.-K. Plattner, M. Tignor, S. K. Allen and co-authors), Cambridge University Press, Cambridge, UK, 573–574

[16] Bougiatioti, A., Stavroulas, I., Kostenidou, E., Zarmpas, P., Theodosi, C., Kouvarakis, G., Canonaco, F., Prévôt, A. S. H., Nenes, A., Pandis, S. N., and Mihalopoulos, N.: Processing of biomass-burning aerosol in the eastern Mediterranean during summertime, Atmos. Chem. Phys., 14, 4793–4807, doi:10.5194/acp-14-4793-2014, 2014

[17] Brioude, J., et al., 2013b: The lagrangian particle dispersion model Flexpart-Wrf version 3.1, Geoscientific Model Develop., 6, 1889–1904

[18] Browell, E. V., C. F. Butler, S. Ismail, P. A. Robinette, A. F. Carter, N. S. Higdon, O. B. Toon, M. R. Schoeberl, and A. F. Tuck (1990), Airborne lidar observation in the wintertime arctic stratosphere: Polar stratospheric clouds, Geophys. Res. Lett., 17, 385–388.

[19] Burton, S. P., Ferrare, R. A., Hostetler, C. A., Hair, J. W., Rogers, R. R., Obland, M. D., Butler, C. F., Cook, A. L., Harper, D. B., and Froyd, K. D.: Aerosol classification using airborne High Spectral Resolution Lidar measurements methodology and examples, Atmos. Meas. Tech., 5, 73–98, doi:10.5194/amt-5-73-2012, 2012

[20] Bukowiecki, N., Zieger, P., Weingartner, E., Jurányi, Z., Gysel, M., Neininger, B., Schneider, B., Hueglin, C., Ulrich, A., Wichser, A., Henne, S., Brunner, D., Kaegi, R., Schwikowski, M., Tobler, L., Wienhold, F.G., Engel, I., Buchmann, B., Peter, T. and Baltensperger, U. (2011). Ground-based and Airborne in-situ Measurements of the Eyjafjallajokull Volcanic Aerosol Plume in Switzerland in Spring 2010. Atmos. Chem. Phys. 11: 10011–10030, doi: 10.5194/acp-11-10011-2011

[21] Cairo, F., G.. Di Donfrancesco, L.. Di Liberto, and M.. Viterbini, "The RAMNI airborne lidar for cloud and aerosol research", Atmospheric Measurement Techniques, vol. 5, no. 7, pp. 1779-1792, 2012.

[22] M. Campanelli, V. Estellés, C. Tomasi, T. Nakajima, V. Malvestuto and J. A. Martínez-Lozano. "Application of the SKYRAD improved Langley plot method for the in situ calibration of CIMEL sun-skphotometers" Vol. 46, No. 14 May, 2007, Applied Optics.

[23] C. Carnevale, G. Finzi, G. Mannarini, E. Pisoni, M. Volta (2011).Com-paring mesoscale chemistry-transport model and remote-sensed AerosolOptical Depth, Atmospheric Environment, 45, 289-295

[24] Carnevale, C., Finzi, G., Pisoni, E., Volta, M., Kishcha, P., and Alpert, P.: Integrating Saharan dust forecasts into a regional chemical transport model: a case study over Northern Italy, Sci. Total Environ., 417–418, 224–231, 2012

[25] Carnevale, C., Finzi, G., Pisoni, E., Pederzoli, A., Turrini, E. and Volta, L. (2014). Implementation of the on line coupled model WRF/CHEM over the PO Valley. Karlsruhe Intsitute of Technology and University of Hertfordshire

[26] Caricchia A.M, Merluzzi L., Scaramella A., Vaccaro L. (2003), "La banca dati nazionale di qualità dell'aria" Atti della 7a conferenza nazionale delle Agenzie Ambientali L'innovazione al servizio della conoscenza e della prevenzione - Dai sistemi di monitoraggio alla diffusione della cultura ambientale 24 – 16 Novembre 2003 Milano, Italia.

[27] T.N. Carlson, S.G. Benjamin; Radiative Heating Rates for Saharan Dust; Journal of Atmospheric Sciences 37, Issue 1, p. 193-213; 1980

[28] Cattani G, Di Menno di Bucchianico A, Dina D, Inglessis M,Notaro C, Settimo G, et al. 2010. Evaluation of the temporal variation of air quality in Rome, Italy, from 1999 to 2008. Ann Ist Super Sanita 46:242–253.

[29] Chan, P. W. (2010). Determination of Backscatter-Extinction Coefficient Ratio for LIDAR-Retrieved Aerosol Optical Depth Based on Sunphotometer Data. Remote Sensing, 2(9), 2127-2135.

[30] Chen, W. N., Chiang, C. W., and Nee, J. B.: The lidar ratio and depolarization ratio for cirrus clouds, Appl. Optics, 41, 6470–6497, 2002

[31] Chou, M. D., and M. J. Suarez, 1999: A solar radiation parameterization for atmospheric studies. NASA Tech. Memo. 104606, 15, 40 pp.

[32] Chou, M. D., M. J. Suarez, X. Z. Liang, and M. M. H. Yan, 2001: A thermal infrared radiation parameterization for atmospheric studies. NASA Tech. Memo., 104606, 19, 68 pp.

[33] Clarisse, L., Clerbaux, C., Dentener, F., Hurtmans, D., and Coheur, P.-F.: Global ammonia distribution derived from infrared satellite observations, Nat. Geosci., 2, 479–483, doi:10.1038/ngeo551, 2009

[34] Clerbaux, C., D. P. Edwards, M. Deeter, L. Emmons, J.-F. Lamarque, X. X. Tie, S. T. Massie, and J. Gille (2008), Carbon monoxide pollution from cities and urban areas observed by the Terra/MOPITT mission, Geophys. Res. Lett., 35, L03817, doi:10.1029/2007GL032300.

[35] M. J. Costa, E. Catan, A.M. Silva, V. Levizzani; Satellite derived cloud properties relevant for cloud radiative forcing: a case study of interaction between clouds and dust aerosol particles; International Conference on clouds and Precipitation (ICCP) 2004

[36] Cristofanelli, P., Bonasoni, P., Carboni, G., Calzolari, F., Casarola, L., Sajani, S. Z., Santaguida, R.: Anomalous high ozone concentrations recorded at a high mountain station in Italy in summer 2003, Atmos. Environ., 41, 1383–1394, doi:10.1016/j.atmosenv.2006.10.017, 2007

[37] Cristofanelli, P., Marinoni, A., Arduini, J., Bonafè, U., Calzolari, F., Colombo, T., Decesari, S., Duchi, R., Facchini, M. C., Fierli, F., Finessi, E., Maione, M., Chiari, M., Calzolai, G., Messina, P., Orlandi, E., Roccato, F., and Bonasoni, P.: Significant variations of trace gas composition and aerosol properties at Mt. Cimone during air mass transport from North Africa – contributions

from wildfire emissions and mineral dust, Atmos. Chem. Phys., 9, 4603-4619, doi:10.5194/acp-9-4603-2009, 2009

[38] Cristofanelli, P., Fierli, F., Marinoni, A., Calzolari, F., Duchi, R., Burkhart, J., Stohl, A., Maione, M., Arduini, J., Bonasoni, P., 2013. Influence of biomass burning and anthropogenic emissions on ozone, carbon monoxide and black carbon at the Mt. Cimone GAW-WMO global station (Italy, 2165 m a.s.l.). Atmos. Chem. Phys. 13, 15e30.

[39] Crosier, J., Allan, J. D., Coe, H., Bower, K. N., Formenti, P., and Williams, P. I.: Chemical composition of summertime aerosol in the Po Valley (Italy), northern Adriatic and Black Sea, Q. J. R. Meteorol. Soc., 133, 61-75, 10.1002/qj.88, 2007.

[40] Decesari, S., Allan, J., Plass-Duelmer, C., Williams, B. J., Paglione, M., Facchini, M. C., O'Dowd, C., Harrison, R. M., Gietl, J. K., Coe, H., Giulianelli, L., Gobbi, G. P., Lanconelli, C., Carbone, C., Worsnop, D., Lambe, A. T., Ahern, A. T., Moretti, F., Tagliavini, E., Elste, T., Gilge, S., Zhang, Y., and Dall'Osto, M.: Measurements of the aerosol chemical composition and mixing state in the Po Valley using multiple spectroscopic techniques, Atmos. Chem. Phys., 14, 12109-12132, doi:10.5194/acp-14-12109-2014, 2014.

[41] Di Biagio, C., Doppler, L., Gaimoz, C., Grand, N., Ancellet, G., Raut, J.-C., Beekmann, M., Borbon, A., Sartelet, K., Attié, J.-L., Ravetta, F., and Formenti, P.: Continental pollution in the western Mediterranean basin: vertical profiles of aerosol and trace gases measured over the sea during TRAQA 2012 and SAFMED 2013, Atmos. Chem. Phys., 15, 9611-9630, doi:10.5194/acp-15-9611-2015, 2015.

[42] di Sarra, A., Di Iorio, T., Cacciani, M., Fiocco, G., and Fua, D.: Saharan dust profiles measured by lidar from Lampedusa, J. Geophys. Res., 106, 10335–10347, 2001

[43] Diémoz, H., M. Campanelli, and V. Estellés, 2014: One year of measurements with a POM-02 sky radiometer at an Alpine EuroSkyRad station. J. Meteor. Soc. Japan, 92A, 1-16. http://dx.doi.org/10.2151/jmsj.2014-A01

[44] Dyer, A. J., and B. B. Hicks, 1970: Flux–gradient relationships in the constant flux layer. Quart. J. Roy. Meteor. Soc., 96, 715–721.

[45] J. Dufresne, C. Gautier, P. Ricchiazzi, Y. Fouquart; Longwave Scattering Effects of Mineral Aerosols; Journal of Atmospheric Science 59, p. 1959-1966; 2002

[46] Dulac, F., and P. Chazette (2003), Airborne study of a multi-layer aerosol structure in the eastern Mediterranean observed with the airborne polarized lidar ALEX during a STAAARTE campaign (7 June 1997), Atmos. Chem. Phys., 3, 1817 – 1831.

[47] Escudero et al. 2005

[48] Fast, J. D., Gustafson, W. I., Easter, R. C., Zaveri, R. A., Barnard, J. C., Chapman, E. G., Grell, G. A., and Peckham, S. E.: Evolution of ozone, particulates, and aerosol direct radiative forcing in the vicinity of Houston using a fully coupled meteorology-chemistry-aerosol model, J. Geophys. Res., 111, 1–29, doi:10.1029/2005JD006721, 2006

[49] Ferrare, R. A., D. D. Turner, L. Heilman-Brasseur, W. F. Feltz, O. Dubovik, and T. P. Tooman (2001), Raman lidar measurements of the aerosol extinction-to-backscatter ratio over the Southern Great Plains, J. Geophys. Res., 106, 20,333–20,347

[50] Fiebig, M., A. Petzold, U. Wandinger, M. Wendisch, C. Kiemle, A. Stifter, M. Ebert, T. Rother, and U. Leiterer (2002), Optical closure for an aerosol column: Method, accuracy, and inferable properties, applied to a biomass-burning aerosol and its radiative forcing, J. Geophys. Res., 107(D21), 8130, doi:10.1029/2000JD000192.

[51] S. Finardi, C. Silibello, A. D'Allura, P. Radice, Analysis of pollutants exchange between the Po Valley and the surrounding European region, Urban Climate, Volume 10, Part 4, December 2014, Pages 682-702, ISSN 2212-0955, http://dx.doi.org/10.1016/j.uclim.2014.02.002. (http://www.sciencedirect.com/science/article/pii/S2212095514000121)

[52] Flamant, C., and J. Pelon, Atmospheric boundary-layer structure over the Mediterranean during a Tramontane event, Quart. J. Roy. Meteorol. Soc., 122, 1741–1778, 1996.

[53] Flentje H. et al., Aerosol profiling using the ceilometer network of the German Meteorological Service, Atmos. Meas. Tech. Discuss., 3, 3643-3673, 2010b

[54] Forster, C., A. Stohl, and P. Seibert (2007): Parameterization of convective transport in a Lagrangian particle dispersion model and its evaluation. J. Appl. Met. Clim. 46, 403-422

[55] Freudenthaler, V., Esselborn, M., Wiegner, M., Heese, B., Tesche, M., Ansmann, A., Muller, D., Althausen, D., Wirth, M., Fix, A., Ehret, G., Knippertz,

P., Toledano, C., Gasteiger, J., Garhammer, M., and Seefeldner, M.: Depolarization ratio profiling at several wavelengths in pure Saharan dust during SAMUM 2006., Tellus, B61, 165–179, doi:10.1111/j.1600-0889.2008.00396.x, 2009

[56] Gangoiti, G., Millán, M. M., Salvador, R., and Mantilla, E.: Long Range transport and recirculation of pollutants in the Western Mediterranean during the RECAPMA Project. Atmos. Environ., 35, 6267-6276, 2001

[57] Gibert, F. , J. Cuesta, J.-I. Yano, N. Arnault, and P. H. Flamant, 2007a: On the correlation between convective plume updrafts and downdrafts, lidar reflectivity and depolarization ratio. Bound.- Layer Meteor., 125, 553–573

[58] Gimeno, L., Drumond, A., Nieto, R., Trigo, R. M., and Stohl, A.: On the origin of continental precipitation, Geophys. Res. Lett., 37, L13804, doi:10.1029/2010GL043712, 2010.

[59] Giorgi, F.: Climate change hot-spots, J. Geophys. Res., 33, L08707, doi:10.1029/2006GL025734, 2006

[60] Giorgi, F., and P. Lionello, 2008: Climate change projections for the Mediterranean region. Global and Planetary Change, 63, 90-104.

[61] Gkikas, A., Hatzianastassiou, N., Mihalopoulos, N., Katsoulis, V., Kazadzis, S., Pey, J., Querol, X., and Torres, O.: The regime of intense desert dust episodes in the Mediterranean based on contemporary satellite observations and ground measurements, Atmos. Chem. Phys., 13, 12135-12154, doi:10.5194/acp-13-12135-2013, 2013.

[62] Gobbi, G. P., Kaufman, Y. J., Koren, I., and Eck, T. F.: Classification of aerosol properties derived from AERONET direct sun data, Atmos. Chem. Phys., 7, 453-458, doi:10.5194/acp-7-453-2007, 2007.

[63] Granier, C., Müller, J. F., Pétron, G., and Brasseur, G.: A threedimensional study of the global CO budget, Chemosphere, 1, 255–261, doi:10.1016/S1465-9972(99)00007-0, 1999

[64] Grell, G. A., Peckham, S. E., McKeen, S., Schmitz, R., Frost, G., Skamarock, W. C., and Eder, B.: Fully coupled "online" chemistry within the WRF model, Atmosph. Env., 39, 6957–6975, 2005

[65] *Groβ*, S., Esselborn, M., Weinzierl, B., Wirth, M., Fix, A., and Petzold, A.: Aerosol classification by airborne high spectral resolution lidar observations, Atmos. Chem. Phys., 2013, 2487–2505, doi:10.5194/acp-13-2487-2013, 2013. 5204

[66] Guenther, A., T. Karl, P. Harley, C. Wiedinmyer, P. I. Palmer, C. Geron (2006) Estimates of global terrestrial isoprene emissions using MEGAN (Model of Emissions of Gases and Aerosols from Nature), Atmos. Chem. Phys., 6, 3181-3210.

[67] Hanke, M., Umann, B., Uecker, J., Arnold, F., Bunz, H., 2003. Atmospheric measurements of gas-phase HNO3 and SO2 using chemical ionization mass spectrometry during the MINATROC field campaign 2000 on Monte Cimone. Atmos. Chem. Phys. 3, 417–436. http://dx.doi.org/10.5194/acp-3-417-2003

[68] J.E. Hansen, M. Sato, R. Ruedy; Radiative forcing and climate response; Journal of Geophysical Research 102, p. 6831–6864; 1997

[69] Hatzianastassiou, N., et al., 2009. Natural versus anthropogenic aerosols in the eastern Mediterranean basin derived from multiyear TOMS and MODIS satellite data. J. Geophys. Res., 114, D24202.

[70] Henry CR, Satran D, Lindgren B, Adkinson C, Nicholson CI, Henry TD. Myocardial injury and long-term mortality following moderate to severe carbon monoxide poisoning. JAMA 2006;295:398–402.

[71] Herrmann, M., Somot, S., Calmanti, S., Dubois, C., and Sevault, F.: Representation of spatial and temporal variability of daily wind speed and of intense wind events over the Mediterranean Sea using dynamical downscaling: impact of the regional climate model configuration, Nat. Hazards Earth Syst. Sci., 11, 1983-2001, doi:10.5194/nhess-11-1983-2011, 2011.

[72] Ernest Hilsenrath, NASA Goddard Space Flight Center, Greenbelt, MD 20771, USA, Christopher J. Readings, ESA, European Space Research and Technology Center, Noordwijk, NL, Jack A. Kaye, NASA, Headquarters, Washington, D.C. 20546, USA, Volker A. Mohnen, IFU-FhG, D-82467 Garmisch, Germany, Integrated Global Observing Strategy (IGOS) for Ozone and Relevant Atmospheric Parameters, Stratospheric Processes And their Role in Climate (SPARC), $http : //www.atmosp.physics.utoronto.ca/SPARC/News16/16_Hilsenrath.html$

[73] Hodas, N., Meng, Q.Y., Lunden, M.M., Turpin, B.J., 2014. Toward refined estimates of ambient PM2.5 exposure: Evaluation of a physical outdoor to indoor transport model. Atmospheric Environment 83, 229-236.

[74] J. Huang, B. Lin, P. Minnis, T. Wang, X. Wang, Y. Hu, Y. Yi, J.K. Ayers; Satellite-based Assessment of Possible Dust Aerosols Semi-Direct Effect on Cloud Water Path over East Asia; Geophysical Research Letters 33; 2006

[75] Inaba, H. Detection of Atoms and Molecules by Raman Scattering and Resonance Fluorescence. In Laser Monitoring of the Atmosphere; Hinkley, E.D., Ed.; SpringerVerlag: New York, 1976; 153–236. Chap. 5.

[76] IPCC, 2007: Climate Change 2007: Synthesis Report. Contribution of Working Groups I, II and III to the Fourth Assessment Report of the Intergovernmental Panel on Climate Change [Core Writing Team, Pachauri, R.K and Reisinger, A. (eds.)]. IPCC, Geneva, Switzerland, 104 pp.

[77] IPCC, 2013: Climate Change 2013: The Physical Science Basis. Contribution of Working Group I to the Fifth Assessment Report of the Intergovernmental Panel on Climate Change [Stocker, T.F., D. Qin, G.-K. Plattner, M. Tignor, S.K. Allen, J. Boschung, A. Nauels, Y. Xia, V. Bex and P.M. Midgley (eds.)]. Cambridge University Press, Cambridge, United Kingdom and New York, NY, USA, 1535 pp, doi:10.1017/CBO9781107415324

[78] Iwasaka, Y., Shibata, T., Nagatani, T., Shi, G.-Y., Kim, Y. S., Matsuki, A., Trochkine, D., Zhang, D., Yamada, M., Nagatani, M., Nakata, H., Shen, Z., Li, G., Chen, B., and Kawahiraand, K.: Large depolarization ratio of free tropospheric aerosols over the Taklamakan desert revealed by lidar measurements: possible diffusion and transport of dust particles, J. Geophys. Res., 108, 8652, doi:10.1029/2002JD003267, 2003

[79] Kalivitis, N., Gerasopoulos, E., Vrekoussis, M., Kouvarakis, G., Kubilay, N., Hatzianastassiou, N., Vardavas, I., and Mihalopoulos, N.: Dust transport over the eastern Mediterranean derived from Total Ozone Mapping Spectrometer, Aerosol Robotic Network, and surface measurements, J. Geophys. Res.-Atmos., 112, D03202, doi:10.1029/2006JD007510, 2007.

[80] Kampa, M., Castanas, E.: Human health effects of air pollution, Environ. Pollut. (2007), doi:10.1016/j.envpol.2007.06.012

[81] Kanakidou M, Mihalopoulos N, Kindap T, Im U, Vrekoussis M, Gerasopoulos E, Dermitzaki E, Unal A, Koçak M, Markakis K, Melas D, Kouvarakis G, Youssef AF, Richter A. 2011. Megacities as hot spots of air pollution in the east Mediterranean. Atmos. Environ. 45: 1223–1235

[82] Killinger, D.K.; Menyuk, N. Laser remote sensing of the atmosphere. Science 1987, 235, 37 – 45

[83] Kim, D. Y., and V. Ramanathan (2008), Solar radiation budget and radiative forcing due to aerosols and clouds, J Geophys Res-Atmos, 113(D2)

[84] Klett, J. D.: Stable analytical inversion solution for processing lidar returns, Appl. Optics, 20, 211–220, 1981

[85] S. Lafon, I.N. Sokolik, J.L. Rajot, S. Caquineau, A. Gaudichet; Characterization of iron oxides in mineral dust aerosols: Implications for light absorption; Journal of Geophysical Research 111; 2006

[86] Lawrence, M. G., Butler, T. M., Steinkamp, J., Gurjar, B. R., and Lelieveld, J.: Regional pollution potentials of megacities and other major population centers, Atmos. Chem. Phys., 7, 3969–3987, doi:10.5194/acp-7-3969-2007, 2007.

[87] Legg, B. J. and Raupach, M. R.: Markov-chain simulation of particle dispersion in inhomogeneous flows: the mean drift velocity induced by a gradient in Eulerian velocity variance, Bound. Layer Met., 24, 3–13, 1982

[88] Lelieveld, J., Berresheim, H., Borrmann, S., et al.: Global air pollution crossroads over the Mediterranean, Science, 298, 794–799, 2002.

[89] Lelieveld, J., Evans, J. S., Fnais, M., Giannadaki, D. and Pozze, A.: The Contribution of Outdoor Air Pollution Sources to Premature Mortality on a Global Scale, Nature International Weekly Journal of Science, 525, 367–371, 2015.

[90] Li, Q. B., Jacob, D. J., Bey, I., Palmer, P. I., Duncan, B. N., Field, B. D., Martin, R. V., Fiore, A. M., Yantosca, R. M., Parrish, D. D., Simmonds, P. G., and Oltmans, S. J.: Transatlantic transport of pollution and its effects on surface ozone in Europe and North America, J. Geophys. Res., 107(D13), 4166, doi:10.1029/2001JD001422, 2002

[91] Lionello, P., P. Malanotte-Rizzoli, R. Boscolo. and co-authors.: The Mediterranean Climate: An overview of the main characteristics and issues, 'Mediterranean Climate Variability', Elsevier B.V., 1-26, 2006a.

[92] Liu, Z., Omar, A., Vaughan, M., Hair, J., Kittaka, C., Hu, Y., Powell, K., Trepte, C., Winker, D., Hostetler, C., Ferrare, R., and Pierce, R.: Calipso lidar observations of the optical properties of Saharan dust: A case study of long-range transport, J. Geophys. Res., 113, D07207, doi:10.1029/2007JD008878, 2008.

[93] Liu, Z., Guan, D., Crawford-Brown, D., Zhang, Q., He, K., and Liu, J.: A low-carbon road map for China, Nature, 500, 143–145, 2013.

[94] U. Lohmann, J. Feichter; Global indirect aerosol effects: a review; Atmospheric Chemistry and Physics 5, p. 715-737; 2005

[95] Mallet, M., Van Dingenen, R., Roger, J. C., Despiau, S., and Cachier, H.: In situ airborne measurements of aerosol optical properties during photochemical pollution events, J. Geophys. Res., 110, D03205, doi:10.1029/2004JD005139, 2005.

[96] M. Mallet, P. Tulet, D. Serc, F. Solmon, O. Dubovik, J. Pelon, V. Pont, O. Thouron; Impact of dust aerosols on the radiative budget, surface heat fluxes, heating rate profiles and convective activity over West Africa during March 2006; Atmospheric Chemistry and Physics Discussion 9, p. 2967-3006; 2009

[97] Mao, H. and Talbot, R.: O3 and CO in New England: Temporal variations and relationships, J. Geophys. Res., 109, D21304, doi:10.1029/2004JD004913, 2004

[98] Matthias, V., et al., Lidar intercomparison on algorithm and system level in the frame of EARLINET, MPI Rep. 337, Max-Planck-Inst. fur Meteorol., Hamburg, Germany, 2002.

[99] Marchuk, G. I., G. A. Mikhailiv, M. A. Nazaraliev, R. A. Darbinjan, B. A. Kargina, and B. S. Elepov, The Monte Carlo Methods in Atmospheric Optics, Springer Ser. Opt. Sci., vol. 12 , Springer-Verlag, New York, 1980.

[100] Marinoni, A.., P. Cristofanelli, F.. Calzolari, F.. Roccato, U.. Bonafé, and P.. Bonasoni, "Continuous measurements of aerosol physical parameters at the Mt. Cimone GAW Station (2165 m asl, Italy)", Science of the Total Environment, vol. 391, no. 2-3, pp. 241-251, 2008.

[101] Maryon, R. H.: Determining cross-wind variance for low frequency wind meander, Atmos. Environ., 32, 115–121, 1998

[102] Matassoni L, Pratesi G, Centioli D, Cadoni F, Malesani P, Caricchia AM, et al. 2009. Saharan dust episodes in Italy: influence on PM10 daily limit value (DLV) exceedances and the related synoptic. J Environ Monit 11:1586–1594.

[103] Middleton, P., W. R. Stockwell, and W. P. L. Carter (1990): "Aggregation and Analysis of Volatile Organic Compound Emissions for Regional Modeling," Atmos. Environ., 24A, 1107-1133.

[104] Menut, L., Flamant, C., Pelon, J., and Flamant, P. H.: "Urban boundary-layer height determination from lidar measurements over the Paris area," Appl. Opt. 38, 945-954 (1999)

[105] Mie, G.: Beiträge zur Optik trüber Medien, speziell kolloidaler Metallösungen, Ann. Phys., 330, 377–445, doi:10.1002/andp.19083300302, (1908),18617

[106] Millán, M. M., Salvador, R., Mantilla, E., and Kallos, G.: Photooxidant dynamics in the Mediterranean basin in summer: results from European research projects, J. Geophys. Res., 102, 8811–8823, doi:10.1029/96JD03610, 1997

[107] Millán, M., Mantilla, E., Salvador, R., Carratala, A., Sanz, M. J., Alonso, L., Gangoiti, G., and Navazo, M.: Ozone cycles in the western Mediterranean

basin: interpretation of monitoring data in complex coastal terrain, J. Appl. Meteorol., 39, 487–508, 73–83, 2000.

[108] Millán , M., Sanz, M.J., Salvador, R., Mantilla, E., 2002. Atmospheric dynamics and ozone cycles related to nitrogen deposition in the western Mediterranean. Environ. Pollut. 118, 167-186. doi:10.1016/S0269-7491(01)00311-6

[109] Mlawer, Eli. J., Steven. J. Taubman, Patrick. D. Brown, M. J. Iacono, and S. A. Clough (1997), Radiative transfer for inhomogeneous atmospheres: RRTM, a validated correlated–k model for the longwave. J. Geophys. Res., 102, 16663–16682.

[110] Monks , P.S., Gas-phase radical chemistry in the troposphere, Chem. Soc. Rev., 34 (2005), pp. 376–395

[111] Monks, P., Granier, C., Fuzzi, S., Stohl, A., Williams, M., Akimoto, H., Amann, M., Baklanov, A., Baltensperger, U., Bey, I., Blake, N., Blake, R., Carslaw, K., Cooper, O., Dentener, F., Fowler, D., Fragkou, E., Frost, G., Generoso, S., Ginoux, P., Grewe, V., Guen- 25 ther, A., Hansson, H., Henne, S., Hjorth, J., Hofzumahaus, A., Huntrieser, H., Isaksen, I., Jenkin, M., Kaiser, J., Kanakidou, M., Klimont, Z., Kulmala, M., Laj, P., Lawrence, M., Lee, J., Liousse, C., Maione, M., McFiggans, G., Metzger, A., Mieville, A., Moussiopoulos, N., Orlando, J., O'Dowd, C., Palmer, P., Parrish, D., Petzold, A., Platt, U., Pschl, U., Prvt, A., Reeves, C., Reimann, S., Rudich, Y., Sellegri, K., Steinbrecher, R., Simpson, D., 30 ten Brink, H., Theloke, J., van der Werf, G., Vautard, R., Vestreng, V., Vlachokostas, C., and von Glasow, R.: Atmospheric composition change – global and regional air quality, Atmos. Environ., 43, 5268–5350, doi:10.1016/j.atmosenv.2009.08.021, 2009. 8193, 8194

[112] Morrison, H., G. Thompson, V. Tatarskii, 2009: Impact of Cloud Microphysics on the Development of Trailing Stratiform Precipitation in a Simulated Squall Line: Comparison of One– and Two–Moment Schemes. Mon. Wea. Rev., 137, 991–1007.

[113] Müller, D., A. Ansmann, I. Mattis, M. Tesche, U. Wandinger, D. Althausen, and G. Pisani (2007), Aerosol-type-dependent lidar ratios observed with Raman lidar, J. Geophys. Res., 112, D16202, doi:10.1029/2006JD008292

[114] Murayama, T., H. O. N. Kaneyasu, H. Kamataki, and K. Miura (1999), Application of lidar depolarization measurement in the atmospheric boundary layer: Effects of dust and sea-salt particles, J. Geophys. Res., 104, 31781–31792

[115] Murayama, T., Masonis, S. J., Redemann, J., Anderson, T. L., Schmid, B., Livingston, J. M., Russell, P. B., Huebert, B., Howell, S. G., McNaughton,

C. S., Clarke, A., Abo, M., Shimizu, A., Sugimoto, N., Yabuki, M., Kuze, H., Fukagawa, S., Maxwell-Meier, K., Weber, R. J., Orsini, D. A., Blomquist, B., Bandy, A., and Thornton, D.: An intercomparison of lidarderived aerosol optical properties with airborne measurements near Tokyo during ACE-Asia, J. Geophys. Res.-Atmos., 108, 8651, doi:10.1029/2002jd003259, 2003

[116] G. Myhre, F. Stordal; Global sensitivity experiments of the radiative forcing due to mineral aerosols; Journal of Geophysical Research 106(16), p. 18,193-18,204; 2001

[117] Nabat, P., Somot, S., Mallet, M., Chiapello, I., Morcrette, J. J., Solmon, F., Szopa, S., Dulac, F., Collins, W., Ghan, S., Horowitz, L. W., Lamarque, J. F., Lee, Y. H., Naik, V., Nagashima, T., Shindell, D., and Skeie, R.: A 4-D climatology (1979–2009) of the monthly tropospheric aerosol optical depth distribution over the Mediterranean region from a comparative evaluation and blending of remote sensing and model products, Atmos. Meas. Tech., 6, 1287–1314, doi:10.5194/amt-6-1287-2013, 2013.

[118] Nakajima, T., G. Tonna, R. Rao, P. Boi, Y. Kaufman, and B. Holben, 1996: Use of sky brightness measurements from ground for remote sensing of particulate polydispersions. Appl. Optics, 35(15), 2672-2686

[119] http://tes.jpl.nasa.gov/mission/biomassburning/

[120] Nedelec, P., Cammas, J.-P., Thouret, V., Athier, G., Cousin, J.-M., Legrand, C., Abonnel, C., Lecoeur, F., Cayez, G., and Marizy, C.: An improved infrared carbon monoxide analyser for routine measurements aboard commercial Airbus aircraft: technical validation and first scientific results of the MOZAIC III programme, Atmos. Chem. Phys., 3, 1551–1564, 2003, http://www.atmos-chem-phys.net/3/1551/2003/.

[121] Nee, J. B., Chiang, C.-W., Hu, H.-l., Hu, S.-X., and Yu, J.-Y.: Lidar measurements of Asian dust storms and dust cloud interactions, J. Geophys. Res., 112, D15202, doi:10.1029/2007JD008476, 2007

[122] Nisantzi, A., Mamouri, R. E., Ansmann, A., and Hadjimitsis, D.: Injection of mineral dust into the free troposphere during fire events observed with polarization lidar at Limassol, Cyprus, Atmos. Chem. Phys., 14, 12155–12165, doi:10.5194/acp-14-12155-2014, 2014. 5211

[123] O'Connor, E. J., Illingworth, A. J., and Hogan, R. J.: A technique for autocalibration of cloud lidar, J. Atmos. Ocean. Tech., 21, 777–786, 2004

[124] Omar, A. H., Winker, D. M., Kittaka, C., Vaughan, M. A., Liu, Z. Y., Hu, Y. X., Trepte, C. R., Rogers, R. R., Ferrare, R. A., Lee, K. P., Kuehn, R.

E., and Hostetler, C. A.: The CALIPSO Automated Aerosol Classification and Lidar Ratio Selection Algorithm, J. Atmos. Ocean. Tech., 26, 1994–2014, doi:10.1175/2009jtecha1231.1, 2009

[125] Papayannis, A., Balis, D., Amiridis, V., Chourdakis, G., Tsaknakis, G., Zerefos, C., Castanho, A. D. A., Nickovic, S., Kazadzis, S., and Grabowski, J.: Measurements of Saharan dust aerosols over the Eastern Mediterranean using elastic backscatter-Raman lidar, spectrophotometric and satellite observations in the frame of the EARLINET project, Atmos. Chem. Phys., 5, 2065–2079,doi:10.5194/acp-5-2065-2005, 2005.

[126] Pappalardo, G. et al., 2004: Aerosol lidar intercomparison in the framework of the EARLINET project. 3 -Raman lidar algorithm for aerosol extinction, backscatter and lidar ratio, Appl. Opt., Vol. 43, N. 28, 5370-5385. (http://www.ncbi.nlm.nih.gov/pubmed/15495429)

[127] M. Pasqui, B. Gozzini, F. Pasi ; Sahara dust impact on precipitation severe storm events over West-Central Mediterranean Area; International Conference on clouds and Precipitation (ICCP) 2004

[128] Pavese, G., Calvello, M., Esposito, F., Leone, L., and Restieri, R.: Effects of Saharan dust advection on atmospheric aerosol properties in the West-Mediterranean area, Adv. Meteorol., 2012, 730579, doi:10.1155/2012/730579, 2012.

[129] Paulson, C. A., 1970: The mathematical representation of wind speed and temperature profiles in the unstable atmospheric surface layer. J. Appl. Meteor., 9, 857–861.

[130] Pederzoli, A., Mircea M, Finardi S, Di Sarra A, Zanini G. Quantification of Saharan dust contribution to PM10 concentrations over Italy during 2003–2005. Atmos Environ, 2010; 44:4181–90

[131] Pérez, C., Sicard, M., Jorba, O., Comerón, A., and Baldasano, J. M. (2004). Summertime re-circulations of air pollutants over the north-eastern Iberian coast observed from systematic EARLINET lidar measurements in Barcelona. Atmospheric Environment, 38(24), 3983-4000.

[132] Pérez, C., Nickovic, S., Pejanovic, G., Baldasano, J. M. and Ozsoy, E. 2006a. Interactive dust-radiation modeling: a step to improve weather forecasts. J. Geophys. Res. 11, D16206.

[133] Pérez, C., Nickovic, S., Baldasano, J. M., Sicard, M., Rocadenbosch, F. and co-authors. 2006b. A long Saharan dust event over the western Mediterranean:

Lidar, Sun photometer observations, and regional dust modeling. J. Geophys. Res. 111, D15214.

[134] Pérez, N., Pey, J., Castillo, S., Alastuey, A., Querol, X. and Viana, M., 2008, Interpretation of the variability of regional background aerosols in the western Mediterranean, Science of the Total Environment, 407, 527–540.

[135] J. Perlwitz, R.L. Miller; Cloud cover increase with increasing aerosol absorptivity: A counterexample to the conventional semidirect aerosol effect; Journal of Geophysical Research 115; 2010

[136] Perrino, C., Catrambrone, M., Pietrodangelo, A.,(2008). Influence of atmospheric stability on the mass concentration and chemical composition of atmospheric particles: a case study in Rome, Italy. Environment International 34, 621–628

[137] Pey, J., Pérez, N., Querol, X., Alastuey, A., Cusack, M., Reche, C., 2010. Intense winter atmospheric pollution episodes affecting the Western Mediterranean. Sci. Total Environ. 408, 1951-1959

[138] Pey, J., Querol, X., Alastuey, A., Forastiere, F., and Stafoggia, M.: African dust outbreaks over the Mediterranean Basin during 2001–2011: PM10 concentrations, phenomenology and 10 trends, and its relation with synoptic and mesoscale meteorology, Atmos. Chem. Phys., 13, 1395–1410, doi:10.5194/acp-13-1395-2013, 2013

[139] Pfeifer, S., Müller, T., Weinhold, K., Zikova, N., Santos, S., Marinoni, A., Bischof, O. F., Kykal, C., Ries, L., Meinhardt, F., Aalto, P., Mihalopoulos, N., and Wiedensohler, A.: Intercomparison of 15 aerodynamic particle size spectrometers (APS 3321): uncertainties in particle sizing and number size distribution, Atmos. Meas. Tech. Discuss. , 8, 11513-11532, doi:10.5194/amtd-8-11513-2015 , 2015

[140] Pope CA III, Burnett RT, Thun MJ, Calle EE, Krewski D, Ito K, Thurston GD. Lung cancer, cardiopulmonary mortality, and longterm exposure to fine particulate air pollution. JAMA 2002;287:1132–1141

[141] Pöschl, U. (2005), Atmospheric Aerosols: Composition, Transformation, Climate and Health Effects. Angewandte Chemie International Edition, 44: 7520–7540. doi:10.1002/anie.200501122

[142] Eric O. Potma and Shaul Mukamel, "Theory of Coherent Raman Scattering", in Coherent Raman Scattering Microscopy, J. X. Cheng and X. S. Xie (Eds.), CRC Press (2013).

[143] Prospero, J. M., Charlson, R. J., Mohnen, V., Jaenicke, R., Delany, A. C., Moyers, J., Zoller, W. and Rahn, K. 1983. The atmospheric aerosol system: an overview. Rev. Geophys. Space Phys. 21, 1607–1629.

[144] Prospero, J.M., Ginoux, P., Torres, O., Nicholson, S.E., Gill, T.E., 2002. Environmental characterization of global sources of atmospheric soil dust identified with the nimbus 7 total ozone mapping spectrometer (TOMS) absorbing aerosol product. Rev. Geophys. 40, 1002. doi:10.1029/2000RF000095.

[145] H. R. Pruppacher and J. D. Klett: Microphysics of Clouds and Precipitation, second edition, Kluwer Academic Publishers, Dordrecht, The Netherlands, 1997, 954 pp.,hardback ISBN 0-79-234211-1

[146] Putaud, J.P., Van Dingenen, R., Dell'Acqua, A., Raes, F., Matta, E., Decesari, S., Facchini, M.C., Fuzzi, S., 2004. Sizesegregated aerosol mass closure and chemical composition in Monte Cimone (I) during MINATROC. Atmospheric Chemistry and Physics 4, 889 - 902

[147] Querol, X, Pey, J., Pandolfi, M., Alastuey, A., Cusack, M., Pérez, N., Moreno, T., Viana, M., Mihalopoulos, N., Kallos, G., Kleanthous, S., 2009a. African dust contributions to mean ambient PM10 mass-levels across the Mediterranean Basin. Atmos. Environ. 43, 4266-4277

[148] K. Rajeshwar, R. McConnell, S. Licht, Solar Hydrogen Generation: Toward a Renewable Energy Future(2008) ,DOI 10.1007/978-0-387-72810-0, Technology and Engineering, https://books.google.it/books?isbn=0387728104

[149] Rea, G., Turquety, S., Menut, L., Briant, R., Mailler, S., and Siour, G. (2015). Source contributions to 2012 summertime aerosols in the euro-mediterranean region. Atmospheric Chemistry and Physics Discussions, 15(6):8191–8242

[150] Rosati, B., Gysel, M., Rubach, F., Mentel, T. F., Goger, B., Poulain, L., Schlag, P., Miettinen, P., Pajunoja, A., Virtanen, A., Bialek, J., Klein Baltink, H., Henzing, J. S., Größ, J., Gobbi, G. P., Wiedensohler, A., Kiendler-Scharr, A., O'Dowd, C., Decesari, S., Facchini, M. C., Weingartner, E., and Baltensperger, U.: Vertical profiling of aerosol hygroscopic properties in the planetary boundary layer during the PEGASOS campaigns, Atmos. Chem. Phys. Discuss., 15, 9445–9505, doi:10.5194/acpd-15-9445-2015, 2015b. 18613, 18615, 18616, 18618, 18624, 18626, 18629

[151] Rosati, B. et al, Comparison of vertical aerosol extinction coefficients from in-situ and LIDAR measurements, Atmos. Chem. Phys., 15(13-13):18609-18651. DOI:10.5194/acpd-15-18609-2015

[152] D. Rosenfeld, Y. Rudich, R. Lahav; Desert dust suppressing precipitation: A possible desertification feedback loop; Proceedings of the National Academy of Sciences 98(11), p. 5975-5980; 2001

[153] Rossa A, Ferrario ME, Sansone M, Monai M. 2012. Climatology of the static stability of the night-time Po Valley pbl from radio sondes and passive microwave radiometers. In Proceedings of the 9th International Symposium on Tropospheric Profiling, Cimini D, Di Girolamo P, Marzano FS, Rizi V (eds), L'Aquila, Italy, September 2012. ESAConference Bureau: Noordwijk, The Netherlands.

[154] Royer, P., Raut, J.-C., Ajello, G., Berthier, S., and Chazette, P.: Synergy between CALIOP and MODIS instruments for aerosol monitoring: application to the Po Valley, Atmos. Meas. Tech.,3, 893–907, doi:10.5194/amt-3-893-2010, 2010.

[155] Russell, P. B., Swissler, T. J., and McCormick, M. P.: Methodology for error analysis and simulation of lidar aerosol measurements, Appl. Optics, 18, 3783–3797, 1979

[156] Saarikoski, S., Carbone, S., Decesari, S., Giulianelli, L., Angelini, F., Canagaratna, M., Ng, N. L., Trimborn, A., Facchini, M. C., Fuzzi, S., Hillamo, R., and Worsnop, D.: Chemical characterization of springtime submicrometer aerosol in Po Valley, Italy, Atmos. Chem. Phys., 12, 8401–8421, doi:10.5194/acp-12-8401-2012, 2012.

[157] Samoli E, Touloumi G, Schwartz J, Anderson HR, Schindler C, Forsberg B, Vigotti MA, Vonk J, Kosnik M, Skorkovsky J, et al. Short-term effects of carbon monoxide on mortality: an analysis within the APHEA project. Environ Health Perspect 2007;115:1578–1583.

[158] Sakulyanontvittaya, T., T. Duhl, C. Wiedinmyer, D. Helmig, S. Matsunaga, M. Potosnak, J. Milford, A. Guenther (2008) Monoterpene and Sesquiterpene Emission Estimates for the United States. Environmental Science & Technology, 42 (5), 1623-1629

[159] S.K. Satheesh, K. Krishna Moorthy; Radiative effects of natural aerosols: A review; Atmospheric Environment Volume 39, Issue 11, p. 2089-2110; 2005

[160] Schaap, M., Otjes, R. P., and Weijers, E. P.: Illustrating the benefit of using hourly monitoring data on secondary inorganic aerosol and its precursors for model evaluation, Atmos. Chem. Phys., 11, 11041–11053, doi:10.5194/acp-11-11041-2011, 2011

[161] Schell, B., I.J. Ackermann, H. Hass, F. S. Binkowski, A. Ebel, 2001: Modeling the formation of secondary organic aerosol within a comprehensive air quality model system. J. Geophys. Res., 106, 28275–28293.

[162] Schicker, I., Radanovics, S., and Seibert, P.: Origin and transport of Mediterranean moisture and air, Atmos. Chem. Phys., 10, 5089–5105, doi:10.5194/acp-10-5089-2010, 2010.

[163] Schultz, M. G., A. Heil, J. J. Hoelzemann, A. Spessa, K. Thonicke, J. G. Goldammer, A. C. Held, J. M. C. Pereira, and M. van het Bolscher (2008), Global wildland fire emissions from 1960 to 2000, Global Biogeochem. Cycles, 22, GB2002, doi:10.1029/2007GB003031

[164] Seaton, A.; MacNee, W.; Donaldson, K.; Godden, D. Particulate Air Pollution and Acute Health Effects; Lancet 1995, 345, 176-178

[165] J. H. Seinfeld, and S. N. Pandis, Atmospheric Chemistry and Physics: From Air Pollution to Climate Change, Wiley and Sons, 1998

[166]

[167] Shimizu, A., Sugimoto, N., Matsui, I., Arao, K., Uno, I., Murayama, T., Kagawa, N., Aoki, K., Uchiyama, A., and Yamazaki, A.: Continuous observations of Asian dust and other aerosols by polarization lidars in China and Japan during ACE-Asia, J. Geophys. Res., 109, D19S17, doi:10.1029/2002jd003253, 2004

[168] Sicard, M., Pérez, C., Rocadenbosch, F., Baldasano, J. M., and García-Vizcaino, D.: Mixedlayer depth determination in the Barcelona coastal area from regular lidar measurements: methods, results and limitations, Bound.-Lay. Meteorol., 119, 135–157, doi:10.1007/s10546-30 005-9005-9, 2006

[169] Slanina, J., ten Brink, H. M., Otjes, R. P., Even, A., Jongejan, P., Khlystov, A., Waijers-Ijpelaan, A., Hu, M., and Lu, Y.: Continuous analysis of nitrate and ammonium in aerosols by the Steam Jet Aerosol Collector (SJAC), Atmos. Environ., 35, 2319–2330, 2001

[170] Somot S. , Sevault F., Déqué M., Crépon M. (2008) 21st century climate change scenario for the Mediterranean using a coupled Atmosphere-Ocean Regional Climate Model. Global and Planetary Change, 63(2-3), pp. 112-126, doi:10.1016/j.gloplacha.2007.10.003

[171] Soriano, C., Baldasano, J. M., Buttler, W. T., and Moore, K.: Circulatory patterns of air pollutants within the Barcelona air basin in a summertime situation: lidar and numerical approaches, Bound.Lay. Meteorol., 98, 33–55, 2001

[172] Stockwell, W. R., P. Middleton, J. S. Chang, and X. Tang (1990): "The Second Generation Regional Acid Deposition Model Chemical Mechanism for Regional Air Quality Modeling," J. Geophys. Res. 95, 16343- 16376

[173] Stohl, A., M. Hittenberger, and G. Wotawa (1998): Validation of the Lagrangian particle dispersion model FLEXPART against large scale tracer experiments. Atmos. Environ. 32

[174] Stohl, A., Forster, C., Frank, A., Seibert, P., and Wotawa, G.: Technical note: The Lagrangian particle dispersion model FLEXPART version 6.2, Atmos. Chem. Phys., 5, 2461-2474, doi:10.5194/acp-5-2461-2005, 2005.

[175] Stull, R. B.: An Introduction to Boundary Layer Meteorology, vol. 13, Kluwer Academic Publishers, the Netherlands, Dordrecht/Boston/London, 1988

[176] Sugimoto, N. and Lee, C. H.: Characteristics of dust aerosols inferred from lidar depolarization measurements at two wavelengths, Appl. Optics, 45, 7468–7474, 2006.

[177] Sullivan, R. C., M. Moore, M. D. Petters, S. M. Kreidenweis, G. Roberts, and K. A. Prather (2009a), Timescale for hygroscopic conversion of mineral dust particles after heterogeneous reaction with nitric acid, Phys. Chem. Chem. Phys., 11, 7826–7837, doi:10.1039/b904217b

[178] Sun, W., et al. (2012), For the depolarization of linearly polarized light by smoke particles, J. Quant. Spectrosc. Radiat. Transfer, doi:10.1016/j.jqsrt.2012.03.031.

[179] I. Tegen, A.A. Lacis, I. Fung; The influence on climate forcing of mineral aerosols from disturbed soils; Nature 380, p. 419-422; 1996

[180] Tesche, M., Ansmann, A., Muller, D., Althausen, D., Engelmann, R., Freudenthaler, V., and Groβ, S.: Vertically resolved separation of dust and smoke over Cape Verde using multiwavelength Raman and polarization lidars during Saharan Mineral Dust Experiment 2008, J. Geophys. Res., 114, D13202, doi:10.1029/2009jd011862, 2009a

[181] Tewari, M., F. Chen, W. Wang, J. Dudhia, M. A. LeMone, K. Mitchell, M. Ek, G. Gayno, J. Wegiel, and R. H. Cuenca, 2004: Implementation and verification of the unified NOAH land surface model in the WRF model. 20th conference on weather analysis and forecasting/16th conference on numerical weather prediction, pp. 11–15.

[182] Task Force on Hemispheric Transport of Air Pollution (TF HTAP), Hemispheric Transport of Air Pollution, 2010, http://www.htap.org/

[183] Thomson D. J.: Criteria for the selection of stochastic models of particle trajectories in turbulent flows, J. Fluid Mech., 180, 529–556, 1987

[184] Thron, R.W., 1996. Direct and indirect exposure to air pollution. Otolaryngol. Head Neck Surg. 114, 281

[185] Tuccella, P., Curci, G., Visconti, G., Bessagnet, B., Menut, L., and Park, R. J.: Modeling of gas and aerosol with WRF/Chem over Europe: Evaluation and sensitivity study, J. Geophys. Res., 117, D03303, doi:10.1029/2011JD016302, 2012

[186] S. Twomey; Pollution and the planetary albedo; Atmospheric Environment 8, Issue 12, p. 1251-1256; 1974

[187] Rita Van Dingenen, Frank Raes, Jean-P Putaud, Urs Baltensperger, Aurélie Charron, M.-Cristina Facchini, Stefano Decesari, Sandro Fuzzi, Robert Gehrig, Hans-C Hansson, Roy M Harrison, Cristoph Hüglin, Alan M Jones, Paolo Laj, Gundi Lorbeer, Willy Maenhaut, Finn Palmgren, Xavier Querol, Sergio Rodriguez, Jürgen Schneider, Harry ten Brink, Peter Tunved, Kjetil Tørseth, Birgit Wehner, Ernest Weingartner, Alfred Wiedensohler, Peter Wåhlin, A European aerosol phenomenology—1: physical characteristics of particulate matter at kerbside, urban, rural and background sites in Europe, Atmospheric Environment, Volume 38, Issue 16, May 2004, Pages 2561-2577, ISSN 1352-2310, http://dx.doi.org/10.1016/j.atmosenv.2004.01.040.

[188] Velchev, K., Cavalli, F., Hjorth, J., Marmer, E., Vignati, E., Dentener, F., and Raes, F.: Ozone over the Western Mediterranean Sea – results from two years of shipborne measurements, Atmos. Chem. Phys., 11, 675–688, doi:10.5194/acp-11-675-2011, 2011.

[189] Varinou, M., Kallos, G., Tsiligiridis, G., and Sisla, G. (2001) The role of anthropogenic and biogenic emissions on tropospheric ozone formation over Greece. Physics and Chemistry of the Earth, 24(5), pp. 507-513.

[190] 24. D. H. P. Vogelezang and A. A. M. Holtslag, Evaluation and model impacts of alternative boundary-layer height formulations, Boundary-Layer Meteorol. 81, 245–269, 1996.

[191] Volckens, J. A. E. and T. M. Peters. (2005) "Counting and particle transmission efficiency of the aerodynamic particle sizer." Journal of Aerosol Science 36: 1400-1408.

[192] von der Weiden, S.-L., Drewnick, F., and Borrmann, S.: Particle Loss Calculator – a new software tool for the assessment of the performance of aerosol inlet systems, Atmos. Meas. Tech., 2, 479–494, doi:10.5194/amt-2-479-2009, 2009

[193] Washington, R., M. C. Todd, N. J. Middleton, and A. S. Goudie (2003), Dust-storm source areas determined by the total ozone monitoring spectrometer and surface observations, Ann. Assoc. Am. Geogr., 93(2), 297–313, doi:10.1111/1467-8306.9302003

[194] Webb, E. K., 1970: Profile relationships: The log-linear range, and extension to strong stability. Quart. J. Roy. Meteor. Soc., 96, 67–90.

[195] Whitby, K. T., and B. Cantrell, Atmospheric aerosols-Characteristics and measurements, Int. Conf Environ. Sens. Assess.Proc., 1975, 1976.

[196] Wiegner, M., Gasteiger, J., Kandler, K., Weinzierl, B., Rasp, K., Esselborn, M., Freudenthaler, V., Heese, B., Toledano, C., Tesche, M., and Althausen, D.: Numerical simulations of optical properties of Saharian dust aerosols with emphasis on lidar applications, Tellus B, 61, 180–194, 2009

[197] Wild, O., Zhu, X., and Prather, M.J., 2000: Fast-J: Accurate simulation of in- and below-cloud photolysis in tropospheric chemical models, J. Atmos. Chem., 37, 245-282

[198] http://www.who.int/mediacentre/news/releases/2014/air-pollution/en/

[199] Y. Yin, S. Wurzler, Z. Levin, T.G. Reisin; Interactions of mineral dust particles and clouds: Effects on precipitation and cloud optical properties; Journal of Geophysical Research 107(23); 2002

[200] Yurganov, L., Grechko, E., and Dzola, A.: Zvenigorod carbon monoxide total column time series: 27 yr of measurements, Chemosphere: Global Changing Science, 1, 127–136, 1999.

[201] Zanis, P., C. Ntogras, A. Zakey, et al., 2012: Regional climate feedback of anthropogenic aerosols over Europe using RegCM3, Climate Res., 52, 267–278, doi:10.3354/cr01070.

[202] Zaveri, R.A., and L.K. Peters, 1999: A new lumped structure photochemical mechanism for large-scale applications, J. Geophys. Res., 104, 30,387 - 30,415

[203] Zaveri, RC Easter, JD Fast, and LK Peters. 2008. "Model for simulating aerosol interactions and chemistry (MOSAIC). J. Geophys. Res., 113, D13204, doi:10.1029/2007JD008792.

[204] Zuev, V.E. Laser Beams in the Atmosphere, Translated by J.S. Wood; Consultants Bureau: New York, 1982.

[205] Zhang, D.–L., and R.A. Anthes, 1982: A high–resolution model of the planetary boundary layer– sensitivity tests and comparisons with SESAME–79 data. J. Appl. Meteor., 21, 1594–1609.

Acknowledgement

I would like to express my special appreciation and thanks to my advisor Professor Dr. Federico Fierli for having supported my work with his precious goal-oriented advices and for helping me to grow as a research scientist with his high analytical supervision and smart advices.

I am also thankful to Dr. Paola Formenti, Prof. Dr. Gabriele Curci and Prof. Dr. Stephan Borrmann for being my reviewers, taking the time to review my thesis and giving me precious feedbacks.

I would like to express my special appreciation to all the members of the research group of the ISAC-CNR institute with which I had the pleasure to spend my PhD years. In particular:

Dr Francesco Cairo, for being like a second supervisor, supporting me patiently and competently in the most experimental part of my work and helping me overcome many of the difficulties I met during my PhD work.

Dr Marcel Snels, for giving me help under many different aspects, from science related advices to practical problems.

Maurizio Viterbini, for his passionate life tips.

Davide Dionisi, Luca Di Liberto and Chiara Cagnazzo for being always available to help me with my scientific doubts.

During these years I also had the possibility to interact and work with a large community of scientists from different European research centers: it allowed me not only to enrich my work with various experiences and contributions but also to learn from different approaches and grow as a scientist. Among them I would like in particular to thank:

François Ravetta, who gave me the opportunity to work with him in the LATMOS laboratoire in Paris for my three months abroad. It was a very precious experience, under several points of view.

Jean Christophe Raut, who gave me access to the WRF-Chem simulations and that was always available to answer my questions.

Stefano De Cesari and Paolo Cristofanelli, for helping me to actively participate to the PEGASOS project, for giving me access to data and their very useful advices and indications on my PhD work.

Christian Tony Landi, who gave me access to the one year WRF simulations and

technical support for my own simulations.

The research groups of Johannes Größ(Universität Leipzig), of Robert Wolf (Paul Scherrer Institut) and, in particular, of Bernadette Rosati (Paul Scherrer Institut) that gave me access to their data and collaborated with us in the framework of the PEGASOS project. Our jointed work helped me to better approach my analysis.

A special thanks is due to all the other PhD students that were my fellow adventurers during these years. I would especially like to thank Alessio, Daniele, Federico, Gloria and Mauro (in alphabetical order) for the scientific help, for the wonderful sharing of experiences, for the chats, the laughs and friendship. Your company was a really treasurable component of my PhD life.

Finally, my deepest gratitude goes to my family and my friends, and especially to Virgilio, for making my life easier and always believing in me. You gave me the courage and the strenght to go on even in the darkest times!